

Banner appropriate to article type will appear here in typeset article

Stability and dynamics of the laminar flow past rectangular prisms

Alessandro Chiarini^{1†} and Edouard Boujo^{2‡}

¹Complex Fluids and Flows Unit, Okinawa Institute of Science and Technology Graduate University, 1919-1 Tancha, Onna-son, Okinawa 904-0495, Japan

²Laboratory of Fluid Mechanics and Instabilities, École Polytechnique Fédérale de Lausanne, CH-1015 Lausanne, Switzerland

(Received xx; revised xx; accepted xx)

The laminar flow past rectangular prisms is studied in the space of length-to-height ratio ($1 \leq L/H \leq 5$), width-to-height ratio ($1.2 \leq W/H \leq 5$) and Reynolds number ($Re \approx 700$). The primary bifurcation is investigated with linear stability analysis. For large W/L it consists of an oscillating mode breaking the top/bottom planar symmetry. For smaller W/L the flow becomes first unstable to stationary perturbations, and the wake experiences a static deflection, vertical for intermediate W/L and horizontal for small W/L . Weakly nonlinear analysis and nonlinear direct numerical simulations are used for $L/H = 5$ and larger Re . For $W/H = 1.2$ and 2.25 , after the primary bifurcation the flow recovers the top/bottom planar symmetry but loses the left/right one, via supercritical and subcritical pitchfork bifurcations, respectively. Further increasing Re , the flow becomes unsteady and oscillates around either the deflected (small W/H) or the non-deflected (intermediate W/H) wake. For intermediate W/H and Re , a periodic and fully symmetric regime is detected, with hairpin vortices shed from the top and bottom leading-edge (LE) shear layers; its triggering mechanism is discussed. At large Re and for all W/H , the flow approaches a chaotic state characterised by the superposition of different modes: shedding of hairpin vortices from the LE shear layers, and wake flapping in the horizontal and vertical directions. In some portions of the parameter space the different modes synchronise, giving rise to periodic regimes also at relatively large Re .

Key words:

1. Introduction

Flows past bluff bodies and their transitions with increasing Reynolds numbers from steady two-dimensional (2D) wake flows, through unsteady and three-

† Email address for correspondence: alessandro.chiarini@oist.jp

‡ Email address for correspondence: edouard.boujo@epfl.ch

dimensional (3D) flows, to fully turbulent wakes have attracted much attention over the years (Oertel 1990; Williamson 1996b; Choi et al. 2008; Thompson et al. 2021), as their relevance goes beyond the fundamental interest and encompasses several industrial applications, for example in the field of vortex-induced vibrations (Williamson & Govardhan 2008).

1.1. 2D cylinders

Most studies on 2D bluff bodies have focused on circular and square cylinders as prototypes to characterise the flow bifurcations. At the critical Reynolds number (based on the free stream velocity U_∞ and cylinder diameter D) $Re_c \approx 45 - 47$ the flow undergoes a Hopf bifurcation from a symmetric steady state towards a time-periodic asymmetric state (Noack & Eckelmann 1994) that gives origin to the von Kármán vortex shedding. The triggering mechanism is known to result from a global instability (Jackson 1987), which arises when the region of local absolute instability is large enough (Chomaz 2005), and whose onset therefore depends on the size of the wake recirculation region and on the maximum reverse flow velocity (Chiarini et al. 2022c). At larger Reynolds numbers the flow undergoes a secondary instability and becomes three-dimensional. For the circular cylinder, mode A with spanwise wavelength $\lambda \approx 3.9D$ becomes unstable at $Re \approx 190$, while mode B with $\lambda \approx 1.2D$ becomes unstable at slightly larger Re (Barkley & Henderson 1996; Williamson 1996b,a). A further quasi-periodic mode with $\lambda \approx 2.5D$ has been found to become unstable at larger Reynolds numbers (Blackburn & Lopez 2003; Blackburn et al. 2005; Blackburn & Sheard 2010).

For 2D rectangular cylinders, the critical Reynolds number and physical mechanism of the bifurcations vary with the length-to-height ratio L/H (Okajima 1982; Mills et al. 1995; Hourigan et al. 2001). For $Re \geq 300$, in fact, the Strouhal number of the flow increases in an almost stepwise manner with L/H , due to a pressure feedback-loop that locks the shedding of vortices from the shear layers separating from the leading and trailing edges (Nakamura et al. 1991). This stepwise increase is closely related to the number of large-scale vortices that fit along the sides of the rectangular cylinders. Two different regimes are possible depending on the relative phase of the leading- and trailing-edge vortices (Chiarini et al. 2022c). Using dynamic mode decomposition, Zhang et al. (2023) observed that the instability mechanism at $Re = 1000$ changes with the length-to-height ratio: for small L/H , the pressure feedback loop encompasses the whole separation region and the instability is controlled by the impinging shear-layer instability; for larger L/H , the feedback loop covers the entire chord of the cylinder and the instability is controlled by the leading-edge vortex shedding instability. The first onset of three-dimensionality also depends on L/H : unlike short cylinders, where the flow becomes 3D via the modes A, B and C of the wake (Robichaux et al. 1999; Blackburn & Lopez 2003), for long enough rectangular cylinders Chiarini et al. (2022b) found that the first 3D unstable mode is of quasi-subharmonic nature and is due to an inviscid mechanism triggered by the interaction of the vortices placed over the cylinder sides.

1.2. Axisymmetric 3D bluff bodies

Less studies have considered flows past 3D bluff bodies, although they are ubiquitous in human life and engineering applications, e.g. tall buildings, chimneys, pylons, cars, trains and other ground vehicles. These flows exhibit a richer physics

and, already at low Reynolds numbers, the first bifurcations and their sequence depend on the body geometry.

Unlike 2D cylinder wakes, the flow past a sphere becomes asymmetric prior to a transition to unsteady flow (Magarvey & Bishop 1961a,b; Magarvey & MacLatchy 1965). The wake remains steady and axisymmetric up to $Re \approx 211$ (Johnson & Patel 1999), and then transitions to a steady asymmetric state through the regular bifurcation of an eigenmode of azimuthal wavenumber $m = 1$ (Tomboulides & Orszag 2000). The resulting wake is characterised by a pair of steady streamwise vortices and exhibits a reflectional symmetry about a longitudinal plane of arbitrary azimuthal orientation. At higher Reynolds numbers the wake undergoes a further bifurcation and the flow becomes unsteady. By means of stability analysis Natarajan & Acrivos (1993) found that the $m = 1$ mode becomes unstable to unsteady perturbations at $Re \approx 277$, as later confirmed by the experiments and simulations of Tomboulides *et al.* (1993); Johnson & Patel (1999); Tomboulides & Orszag (2000). This unsteady regime consists of hairpin vortices shed downstream of the sphere in the same plane as that of the steady asymmetric regime. Citro *et al.* (2017) performed a 3D global stability analysis of the steady asymmetric flow to characterise the eigenmode responsible for this second bifurcation. They found a critical Reynolds number of $Re = 272$, and deduced from a structural sensitivity analysis (Giannetti *et al.* 2010) that the instability is driven by the region outside the asymmetric wake. At larger Reynolds numbers, $Re > 600$, the wake loses its periodicity and the flow becomes more chaotic (Magarvey & Bishop 1961b).

A similar bifurcation scenario has been observed for the flow past a disk perpendicular to the incoming flow. At $Re \approx 115$ (based on the disk diameter D) a regular steady bifurcation leads to a 3D steady asymmetric state, with a reflectional symmetry Natarajan & Acrivos (1993); Fabre *et al.* (2008); Meliga *et al.* (2009). At slightly larger Re , i.e. $Re \approx 121$, a Hopf bifurcation breaks the remaining reflectional symmetry and the time invariance. Then, a third bifurcation occurs at $Re \approx 140$ that preserves the flow unsteadiness, but restores a reflectional symmetry normal to that preserved by the first bifurcation.

Similarly, Bohorquez *et al.* (2011) investigated the stability of the laminar flow past bullet-shaped bodies (slender cylindrical bodies with an elliptical leading edge and a blunt trailing edge) of different aspect ratios. They found the same sequence of bifurcations, and observed that the critical Reynolds number increases with the aspect ratio. Compared to the sphere and disk wakes, they found that the symmetry plane selected by the first regular bifurcation is preserved for a larger range of Reynolds numbers, i.e. up to $Re \approx 500$.

1.3. Non-axisymmetric 3D bluff bodies

Many studies on non-axisymmetric 3D bluff bodies have focused on two simple types of geometry: finite circular cylinders and rectangular prisms. Inoue & Sakuragi (2008) investigated the vortex shedding past finite circular cylinders of span-to-diameter ratio in the range $0.5 \leq W/D \leq 100$ with direct numerical simulations (DNS) at low Reynolds numbers $Re \leq 300$. They found that the flow changes drastically depending on W/D and Re , and identified five basic wake patterns: (i) periodic oblique vortex shedding at large W/D and large Re , (ii) quasi-periodic oblique vortex shedding at large W/D and intermediate Re , (iii) periodic hairpin vortex fall off at moderate W/D , (iv) two stable counter-rotating vortex pairs at small W/D and small Re , and (v) alternating shedding

of counter-rotating vortex pairs from the free ends at small W/D and large Re . Yang et al. (2022) considered the same geometry and investigated the effect of W/D in the range $[0.5, 2]$ by means of both DNS and linear stability analysis, for $Re \leq 1000$. At low Re the flow consists of a steady wake with two perpendicular symmetry planes. For small W/D a regular bifurcation leads to a steady state with only one symmetry plane (similar to axisymmetric bodies), here perpendicular to the cylinder axis. At larger Re the flow becomes unsteady via a Hopf bifurcation for all W/D . Two patterns occur with different frequencies and shape, that consist of vortex shedding from the side surface or the free ends of the body, respectively. The critical Reynolds numbers of the bifurcations largely change with W/D .

Rectangular prisms with sharp corners differ from finite circular cylinders, as the corners set the flow separation points. The Reynolds number and sequence of the bifurcations are expected to change with the length-to-height ratio L/H (as already observed for 2D rectangular cylinders) and the width-to-height ratio W/H . Marquet & Larsson (2015) set the length-to-height ratio to $L/H = 1/6$ and investigated the linear stability of the steady flow past thin rectangular plates varying the width-to-height ratio. For $1 \leq W/H \leq 2$ the flow undergoes a pitchfork bifurcation that breaks the top/bottom planar symmetry, similar to the flow past axisymmetric bodies, like spheres and disks. For $W/H > 2.5$ the flow becomes unstable via a Hopf bifurcation that breaks the top/bottom symmetry and leads to a time-periodic regime, similar to 2D cylinders. For intermediate width-to-height ratios, $2 \leq W/H \leq 2.5$, the flow undergoes a Hopf bifurcation that, instead, breaks the left/right planar symmetry. Zampogna & Boujo (2023) set the width-to-height ratio to $W/H = 1.2$ and investigated the flow bifurcations varying the length-to-height ratio between $1/6 \leq L/H \leq 3$. Their analysis yields a series of pitchfork and Hopf bifurcations. Two stationary modes that break respectively the top/bottom and left/right planar symmetries become first unstable. At larger Re , two oscillatory modes become unstable, and again break either the top/bottom or left/right symmetry. The critical Reynolds number of the first bifurcation increases monotonically with L/H , similar to the first instability of the flow past 2D rectangular cylinders (Chiarini et al. 2021) and axisymmetric bodies (disk, sphere and bullet-shaped bodies). For the flow past a cube, this bifurcation scenario is confirmed by the low- Re DNS of Saha (2004) and the experiments of Klotz et al. (2014): at $Re \approx 216$ the steady symmetric flow bifurcates towards a steady asymmetric regime with only one planar symmetry; at $Re = 265$ the flow undergoes a Hopf bifurcation and oscillates about the bifurcated asymmetric regime.

1.4. Present study

In this work we take a step forward from the works of Marquet & Larsson (2015) and Zampogna & Boujo (2023), and characterise the sequence of bifurcations for the flow past rectangular prisms in a three-dimensional space of parameters, varying simultaneously the length-to-height and width-to-height ratios and the Reynolds number. The present study is based on linear and weakly nonlinear stability analysis for the description of the first bifurcations, and on DNS for the complete characterisation of the nonlinear effects and the description of the flow regimes at larger Re . Rectangular prisms with length-to-height and width-to-height ratios between $1 \leq L/H \leq 5$ and $1.2 \leq W/H \leq 5$ and Reynolds numbers up to $Re \approx 700$ are considered. The DNS focus on $L/H = 5$, similar to the BARC benchmark (“Benchmark on the Aerodynamics of a Rectangular 5:1 Cylinder”,

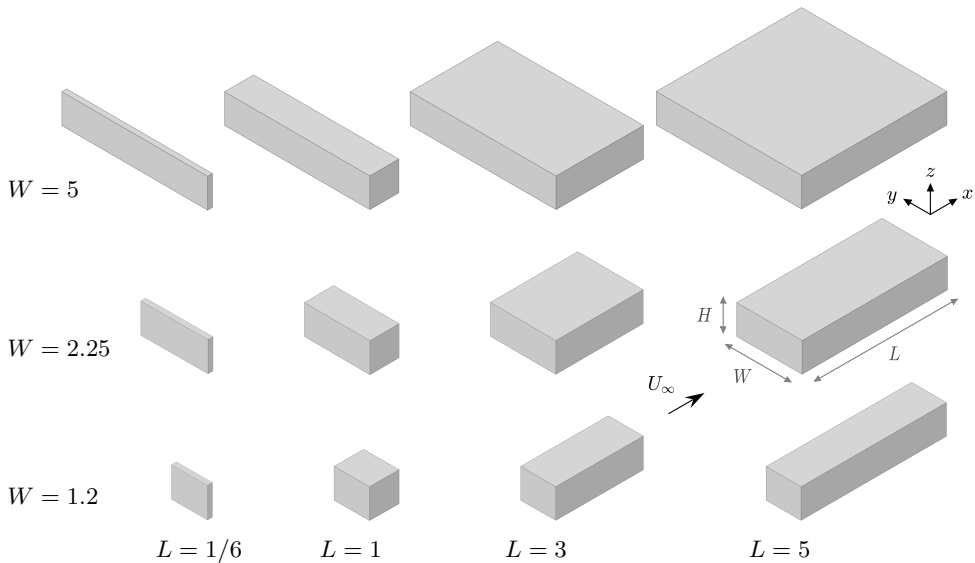


Figure 1: Overview of the bluff body geometry for different lengths L and widths W .

see <https://www.aniv-iawe.org/barc-docs>), which aims to characterise the flow past elongated bluff bodies and set standards for simulations and experiments in the turbulent regime.

The structure of the paper is as follows. Section 2 provides a brief description of the mathematical formulation and numerical methods. The low- Re steady flow is characterised in §3.1, while sections 3.2-3.3 deal with the linear stability analysis. The results of the weakly nonlinear stability analysis are presented in §3.4. Section 4 presents the results from the DNS and details the flow regimes after the first bifurcations for the rectangular prisms with $L/H = 5$. Eventually, a concluding discussion is provided in §5.

2. Methods

2.1. Flow configuration

The incompressible flow past rectangular prisms with aspect ratio $1 \leq L/H \leq 5$ and $1.2 \leq W/H \leq 5$ is considered; here L , W and H are the length, width and height of the prism, i.e. the sizes in the streamwise, spanwise and vertical directions. Figure 1 sketches the geometry and the notation. A Cartesian reference system is placed at the leading edge of the prisms, with the x axis aligned with the flow direction, and the y and z axes denoting the spanwise and vertical directions. The Reynolds number is based on H and on the free stream velocity U_∞ . Unless otherwise stated, hereafter all quantities are made dimensionless with H and U_∞ . The flow is governed by the incompressible Navier-Stokes (NS) equations for the velocity $\mathbf{u} = (u, v, w)$ and pressure p ,

$$\frac{\partial \mathbf{u}}{\partial t} + \mathbf{u} \cdot \nabla \mathbf{u} = -\nabla p + \frac{1}{Re} \nabla^2 \mathbf{u}, \quad \nabla \cdot \mathbf{u} = 0. \quad (2.1)$$

2.2. Mathematical formulation

The onset of the instability is studied by using linear theory that is based on a normal-mode analysis Theofilis (2003, 2011). The field $\{\mathbf{u}, p\}$ of velocity and pressure is divided into a time-independent base flow $\{\mathbf{u}_0, p_0\}$ and an unsteady contribution $\{\mathbf{u}_1, p_1\}$ with small amplitude ϵ , i.e.

$$\mathbf{u}(\mathbf{x}, t) = \mathbf{u}_0(\mathbf{x}) + \epsilon \mathbf{u}_1(\mathbf{x}, t), \text{ and } p(\mathbf{x}, t) = p_0(\mathbf{x}, t) + \epsilon p_1(\mathbf{x}, t). \quad (2.2)$$

Using this decomposition in the NS equations (2.1), the steady base flow equations for $\{\mathbf{u}_0, p_0\}$ are obtained at order ϵ^0 , while the equations governing the small perturbations $\{\mathbf{u}_1, p_1\}$, i.e. the linearised Navier–Stokes (LNS) equations, are obtained at order ϵ^1 . Using the normal-mode ansatz $\{\mathbf{u}_1, p_1\} = \{\hat{\mathbf{u}}_1, \hat{p}_1\}e^{\lambda t} + c.c.$ (where *c.c.* stands for complex conjugate) the equations yield an eigenvalue problem for the complex eigenvalue $\lambda = \sigma + i\omega$ and the complex eigenvector $\{\hat{\mathbf{u}}_1, \hat{p}_1\}$:

$$\lambda \hat{\mathbf{u}}_1 + \mathbf{u}_0 \cdot \nabla \hat{\mathbf{u}}_1 + \hat{\mathbf{u}}_1 \cdot \nabla \mathbf{u}_0 = -\nabla \hat{p}_1 + \frac{1}{Re} \nabla^2 \hat{\mathbf{u}}_1, \quad \nabla \cdot \hat{\mathbf{u}}_1 = 0. \quad (2.3)$$

The linear stability of the system is determined by the sign of the real part of λ , i.e. σ . If all $\sigma < 0$ the perturbations decay and the flow is stable. If otherwise at least one exponent exists with $\sigma > 0$, the perturbations grow exponentially. If $\omega \neq 0$ the mode is time dependent.

2.3. The numerical method

Two different numerical methods are used. The stability analysis is based on finite elements and the simulations have been implemented in the non-commercial software FreeFem++ (Hecht 2012), while the direct numerical simulations are performed using an in-house code based on second-order finite differences.

For the finite element calculations (§3.2), the steady base flow solution of (2.1) and the eigenvalue and eigenmodes solution of (2.3) are calculated with the same method as in Zampogna & Boujo (2023), to which the reader is referred for details. Given the two symmetry planes $y = 0$ and $z = 0$ of the prism, we consider only the quarter-space $y, z \geq 0$ and build in the numerical domain $\{x, y, z \mid -10 \leq x \leq 20; 0 \leq y, z \leq 10\}$ an unstructured tetrahedral mesh with nodes strongly clustered near the prism. See Appendix B for convergence studies with respect to mesh and domain sizes. The weak form of the equations is discretised with Arnold–Brezzi–Fortin MINI-elements (P1 for pressure and P1b for each velocity component). For $W/H \geq 2.5$, dimensions in the y direction are normalised by W and y derivatives are scaled by a factor $1/W$. The nonlinear base flow equations are solved with a Newton method, and the eigenvalue problem with a Krylov–Schur method. Calculations are run in parallel with a domain-decomposition method, typically on 48 processes. Boundary conditions are as follows: at the inlet, free-stream velocity $\mathbf{u}_0 = (1, 0, 0)^T$ and zero perturbation $\mathbf{u}_1 = \mathbf{0}$; on the body surface, no-slip condition $\mathbf{u}_i = \mathbf{0}$ ($i = 0, 1$); at the outlet, stress-free condition $-p_i \mathbf{n} + Re^{-1} \nabla \mathbf{u}_i \cdot \mathbf{n} = \mathbf{0}$ ($i = 0, 1$); finally, on the symmetry planes $y = 0$ and $z = 0$, symmetric (*S*) conditions $u_{i,n} = 0, \partial_n \mathbf{u}_{i,t} = \mathbf{0}$ or antisymmetric (*A*) conditions $\mathbf{u}_{i,t} = \mathbf{0}, \partial_n u_{i,n} = 0$ ($i = 0, 1$; subscripts n and t denoting normal and tangential directions, respectively) are used, the specific choice depending on the considered field, i.e. doubly symmetric base flow $S_y S_z$ or eigenmode belonging to one of the four possible families $S_y S_z, S_y A_z, A_y S_z$ and

$A_y A_z$. Adjoint modes, used to compute structural sensitivities, are obtained in a similar way (see Zampogna & Boujo 2023, for more details).

For the three-dimensional nonlinear simulations (§4), the NS equations are solved using a DNS code introduced by Luchini (2016) and written in CPL Luchini (2021), which employs second-order finite differences on a staggered grid in the three directions. This DNS code has been previously validated and used to compute the flow past rectangular cylinders in both the laminar (Chiarini et al. 2022b) and turbulent (Chiarini & Quadrio 2021, 2022; Chiarini et al. 2022a) regimes. The momentum equation is advanced in time by a fractional step method using a third-order Runge-Kutta scheme. The Poisson equation for the pressure is solved using an iterative SOR algorithm. The presence of the cylinder is dealt with a second-order implicit immersed boundary method, implemented in staggered variables (Luchini 2013). The nonlinear simulations investigate the flow past rectangular prisms with $L/H = 5$ and $W/H = 1.2, 2.25$ and 5 with Reynolds number up to $Re \approx 700$. The computational domain extends for $-25H \leq x \leq 75H$, $-40H \leq y \leq 40H$ and $-25H \leq z \leq 25H$ in the streamwise, spanwise and vertical directions, corresponding to $L_x = 100H$, $L_y = 80H$ and $L_z = 50H$. The prisms extend for $0 \leq x \leq L$, $-W/2 \leq y \leq W/2$ and $-0.5H \leq z \leq 0.5H$, with $y = 0$ and $z = 0$ being the two symmetry planes. The computational domain is discretised with $N_x = 1072$ and $N_z = 590$ points in the streamwise and vertical directions for all cases. The number of points in the spanwise direction increases with W/H being $N_y = 666, 720$ and 804 for $W/H = 1.2, 2.25$ and 5 , respectively. The points are distributed accordingly with a geometrical progression in the three directions, to obtain a higher resolution close to the prisms, especially close to the corners and in the wake. Close to the corners the grid spacing is $\Delta x = \Delta y = \Delta z \approx 0.008H$. The time step is adaptive and computed at every time step to enforce that the Courant-Friedrichs-Lewy number is below unity.

3. Global linear stability analysis

3.1. Base flow

The low- Re steady symmetric base flow is shown in figure 2 by means of iso-surfaces of zero streamwise velocity ($u_0 = 0$) coloured by streamwise vorticity ω_x . The wake has a different shape depending on the prism geometry. Long and narrow bodies (e.g. $L = 5$, $W = 1.2$) tend to exhibit a convex backflow region centred about the vertical and horizontal symmetry planes $y = 0$ and $z = 0$, somewhat reminiscent of axisymmetric wakes. For these bodies the top/bottom and left/right recirculation regions originating from the leading edges reattach on the body upstream of the trailing edges. By contrast, short and wide bodies (e.g. $L = 1$, $W = 5$) tend to exhibit a non-convex backflow region, with two lobes above and below the horizontal symmetry plane $z = 0$. Interestingly, moving downstream the backflow region enlarges in the vertical direction y and shrinks in the spanwise one z , resulting in “peanut”-shaped $y-z$ cross-sections. In addition, the upper/lower recirculation regions originating from the leading edges extend all the way down to the trailing edges without reattaching on the body, and are therefore connected with the main wake recirculation.

Some quantitative properties of the base flow are shown in figure 3. For all the body widths considered, the recirculation length l_r (length of the downstream

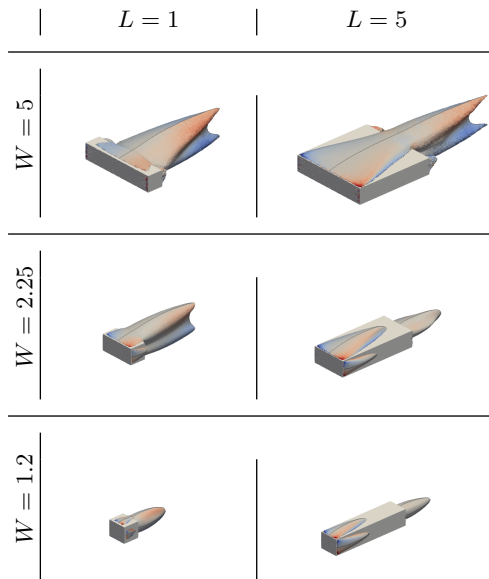


Figure 2: Base flow near the first bifurcation, visualised with isosurfaces of zero streamwise velocity ($u_0 = 0$) coloured by streamwise vorticity ω_x .

recirculation region along the symmetry axis $y = z = 0$ measured from the trailing edge, figure 3a) generally increases with Re , like most 2D and 3D bluff body wakes (Giannetti & Luchini 2007; Marquet & Larsson 2015). Also, l_r decreases with L due to decreasing leading-edge separation angle, in agreement with the observations of Zampogna & Boujo (2023) for prisms $W = 1.2$ and of Chiarini et al. (2022c) for 2D bluff bodies of different shapes. The recirculation length is also seen to increase with W . Anticipating on the linear stability results (§3.2), it appears that at the first bifurcation (dashed line) l_r increases as W increases, while it remains fairly independent on L with an overall slightly decreasing trend.

The base flow drag coefficient $C_x = 2F_x/(\rho U_\infty HW)$, where F_x is the drag force, decreases or stays constant with the Reynolds number in almost the complete space of parameters; see figure 3(b). For narrower bodies, $W = 1.2$ and 2.25, the drag coefficient has a non-monotonic trend with L , first decreasing and then increasing. For longer bodies, $W = 5$, it monotonically increases with L for all Re . At the first bifurcation, C_x varies with L following different trends depending on the body width: it decreases and then increases for $W = 1.2$, monotonically decreases for $W = 2.25$, and remains essentially constant for $W = 5$.

3.2. Linear stability

We now turn to the results of the linear stability analysis. For each geometry, we consider the steady symmetric base flow and look at the eigenmodes that become linearly unstable as Re increases. In particular, we are interested in the symmetries of the modes and whether they are stationary (pitchfork bifurcation) or oscillatory (Hopf bifurcation).

3.2.1. First bifurcation: stability diagram

We start considering the first bifurcation. Figure 4 summarises the effect of the geometry. Three main regions appear in the L - W plane. The flow past wide bodies

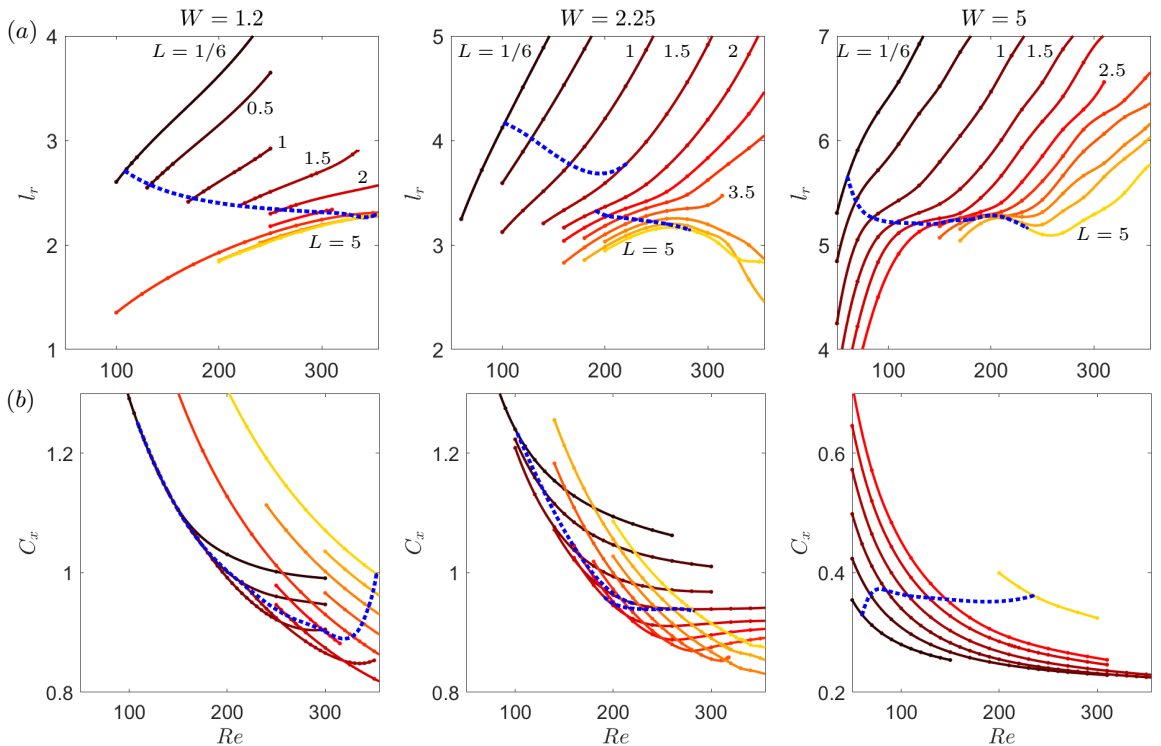


Figure 3: Base flow properties: (a) recirculation length, (b) drag coefficient.

Solid lines: $l_r(Re)$ and $C_x(Re)$ for different body lengths

$L = 1/6, 0.5, 1, \dots, 4.5, 5$. Dotted line: l_r and C_x at the onset of the first bifurcation. Body width from left to right: $W = 1.2, 2.25, 5$.

($W > 2.25$) first become unstable to oscillatory $S_y A_z$ perturbations that break the temporal and the top/bottom planar symmetry and preserve the left/right planar symmetry, leading to a periodic vortex shedding across the shorter body dimension. This is consistent with the 2D limit $W \rightarrow \infty$, and resembles the results for the flow past finite-length circular cylinders (Yang et al. 2022). Increasing the length-to-width ratio L/W , the flow first becomes unstable to stationary $S_y A_z$ perturbations that break the top/bottom spatial symmetry and maintain the left/right one. This bifurcation leads to a static vertical deflection of the wake. Finally, further increasing L/W , the flow first becomes unstable to stationary $A_y S_z$ perturbations that break the left/right symmetry while preserving the top/bottom one. This corresponds to a static horizontal deflection of the wake. By symmetry the $S_y A_z$ and $A_y S_z$ modes become unstable simultaneously in the special case of bodies of square cross section $W/H = 1$, as observed by Marquet & Larsson (2015); Meng et al. (2021); Zampogna & Boujo (2023). Interestingly, the oscillatory $A_y S_z$ mode observed by Marquet & Larsson (2015) for thin plates $L = 1/6$ of intermediate width $2 \leq W \leq 2.5$, seems restricted to a narrow region of the L - W plane.

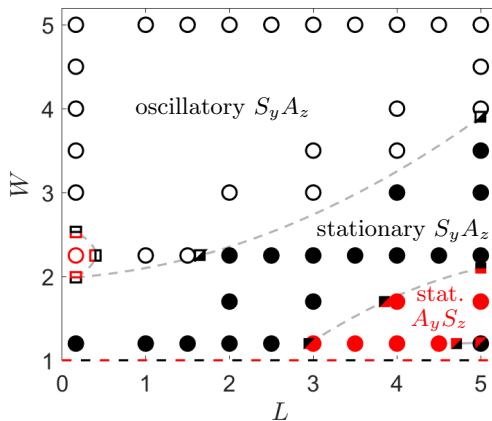


Figure 4: Stability diagram for the first bifurcation. Filled symbols: pitchfork (stationary) bifurcation; open symbols: Hopf (oscillatory) bifurcation. Red: symmetry breaking in the horizontal y direction ($A_y S_z$); black: symmetry breaking in the vertical z direction ($S_y A_z$). Circles: actual calculations; squares: interpolations along L or W . By symmetry, for $W = 1$ the $S_y A_z$ and $A_y S_z$ eigenmodes bifurcate simultaneously.

3.2.2. Eigenmodes and neutral curves

We now proceed to characterise in more detail the linear stability of the steady symmetric low- Re base flow for increasing values of the Reynolds number. Only a few selected geometries are considered. Figure 5 shows the critical Reynolds number and the frequency of the first bifurcations as a function of the body length L for $W = 1.2$, $W = 2.25$ and $W = 5$. The eigenmodes of the first two bifurcations for these widths and the two body lengths $L = 1$ and 5 are shown in figures 6; see also figures 33 and 34 in appendix A.

For narrow bodies, $W = 1.2$, the first two bifurcations of the steady symmetric base flow occur in short succession (as W is close to 1), and correspond to stationary $S_y A_z$ and $A_y S_z$ modes that break either of the two planar symmetries (Zampogna & Boujo 2023). A pair of streamwise streaks of positive and negative streamwise perturbation velocity arise in the wake (figure 6), leading to a vertical or horizontal displacement of the wake. Other bifurcations occur at larger Re and correspond to oscillatory $S_y A_z$ and $A_y S_z$ modes. For small L these modes are almost as unstable as their stationary counterparts, but they quickly become much more stable as L increases, i.e. the corresponding Re_c increases faster. The associated angular frequency is of the order $\omega \simeq 0.4 - 0.6$ ($St = fH/U_\infty \simeq 0.06 - 0.09$, where $f = \omega/(2\pi)$) for $L \leq 2$. The increase of Re_c with L is consistent with the stationary bifurcation of the flow past axisymmetric bodies of different lengths: disk much thinner than its diameter $L/D \ll 1$, sphere $L/D = 1$, bullet-shaped bodies $1 \leq L/D \leq 3.5$ (Natarajan & Acrivos 1993; Fabre et al. 2008; Meliga et al. 2009; Bohorquez et al. 2011) and with the primary oscillatory bifurcation of the flow past 2D bodies of different shape (Jackson 1987; Chiarini et al. 2022c).

For wide bodies, $W = 5$, the first bifurcation corresponds to an oscillatory $S_y A_z$ mode for all L (as already observed in figure 4). The critical Reynolds number increases with L , and is rather well separated from the following bifurcations.

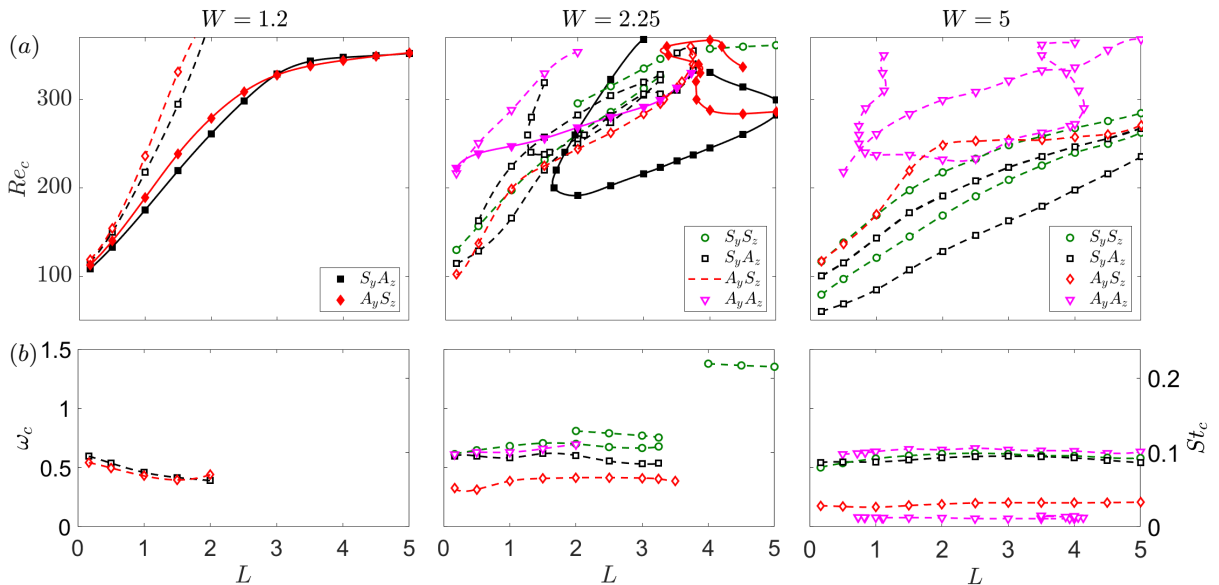


Figure 5: (a) Neutral curves: critical Reynolds number Re_c as a function of body length L , for different body widths, $W = 1.2, 2.25$ and 5 from left to right. Filled symbols and solid lines indicate stationary (pitchfork) bifurcations; open symbols and dashed lines indicate oscillatory (Hopf) bifurcations. Body width from left to right: $W = 1.2, 2.25, 5$. (b) Critical frequency as a function of body length L for a few of the first oscillatory bifurcations. Left-hand axis: angular frequency $\omega_c = \omega(Re_c)$; right-hand axis: Strouhal number $St_c = \omega_c/(2\pi)$.

The angular frequency is $\omega \simeq 0.5 - 0.6$ ($St \simeq 0.08 - 0.10$). The unstable eigenmode is stronger in the central region (small $|y|$); see figure 6. The second bifurcation corresponds to an oscillatory $S_y S_z$ modes for all L . Like the leading $S_y A_z$ mode, it is associated with vortex shedding in the upper and lower shear layers, with a similar frequency but different inter-layer phasing. Unlike the $S_y A_z$ mode that breaks the top/bottom symmetry, the $S_y S_z$ mode preserves both planar symmetries. In other words, in the vertical plane $y = 0$ the two leading modes can be categorised as “sinuous” and “varicose”, respectively. To the best of our knowledge, unsteady doubly symmetric $S_y S_z$ modes have not been reported in 3D bluff body wakes in previous works except for thin plates ($L = 1/6$, $W > 3.1$, Marquet & Larsson (2015)); see also section 4.2. At larger Reynolds numbers further bifurcations are observed, including some involving doubly antisymmetric modes ($A_y A_z$). All these bifurcations are oscillatory and the corresponding frequencies are almost independent on L , and differ by one order of magnitude depending on the bifurcation; see figure 5.

For bodies of intermediate width, $W = 2.25$, the critical Reynolds number of the first bifurcation generally increases with the length of the body, but the leading mode changes with L : stationary for $L > 1.5$ (similar to narrower bodies), and oscillatory with $\omega \simeq 0.3-0.6$ ($St \simeq 0.05 - 0.10$) for $L < 1.5$ (similar to wider bodies). As mentioned previously (figure 4), for this specific width the first bifurcation breaks the left/right symmetry for very short bodies ($L < 0.5$), which leads to the unusual vortex shedding across the larger body dimension observed by Marquet & Larsson (2015), and breaks the top/bottom symmetry

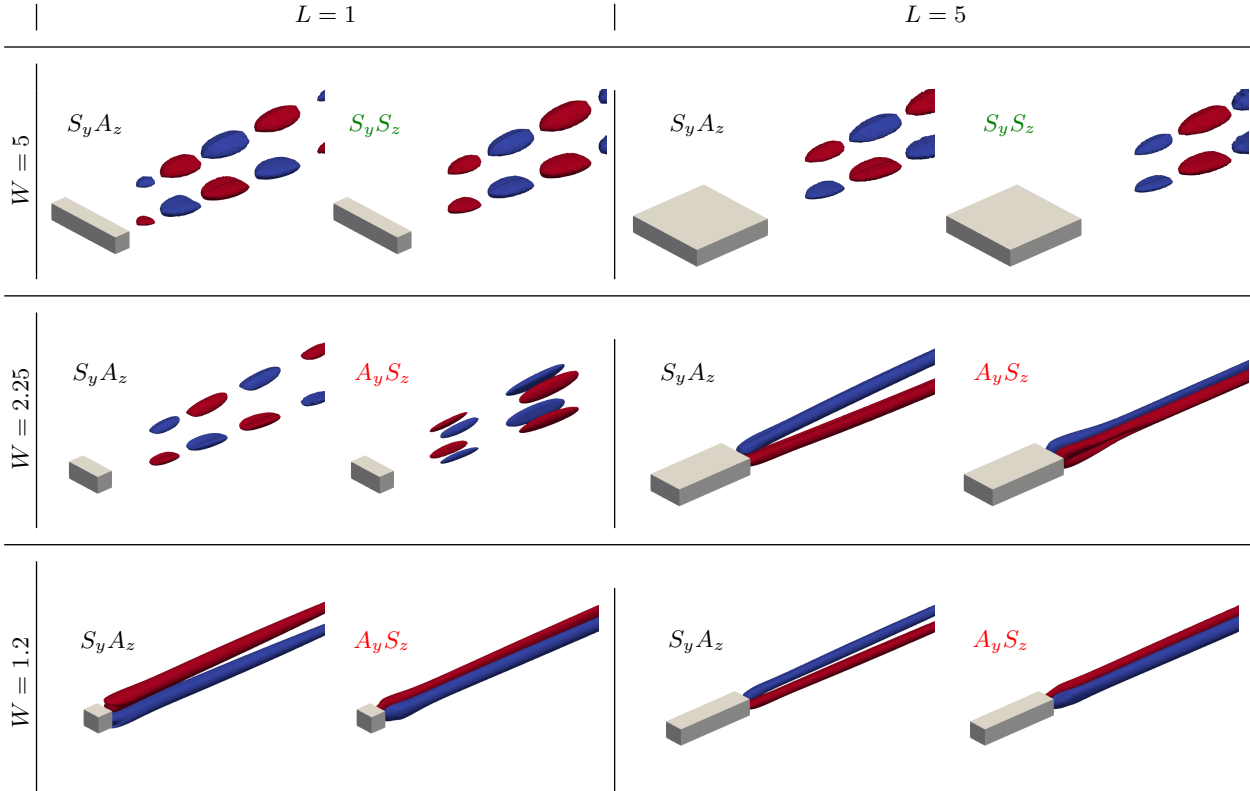


Figure 6: First and second bifurcating eigenmodes (left and right, respectively), visualised with isosurfaces of streamwise velocity.

otherwise, leading to the more usual vortex shedding across the smaller dimension ($0.5 < L < 1.75$) or to a static vertical wake deflection ($L > 1.75$). Interestingly, the stationary $S_y A_z$ mode remains fully stable in the range of Re investigated when $L < 1.5$, while for $L > 1.5$ it is restabilised for large enough Re . Other bifurcations at larger Re draw a more complicated pattern than for $W = 1.2$ and 5. Their order of appearance depends on L , and some modes are unstable only in some interval of L . For almost all values of L , however, doubly symmetric $S_y S_z$ doubly antisymmetric $A_y A_z$ modes only correspond to the third or higher bifurcations.

Figure 7 offers a complementary picture, with neutral curves shown as a function of the body width W for the two body lengths $L = 1/6$ and 5. The first critical Re tends to decrease with W , albeit not monotonously: the first bifurcation lies on the envelope of different neutral curves corresponding to different modes, each mode being more unstable in a preferred interval of W .

3.3. Structural sensitivity

We now look at the structural sensitivity of the two leading modes. Bodies with $L = 1$ and 5 and $W = 1.2, 2.25$ and 5 are considered. Figure 8 shows isosurfaces of $\|\hat{\mathbf{u}}_1\| \|\hat{\mathbf{u}}_1^\dagger\|$, the product of the Euclidean norms of the eigenmode (direct mode) and the associated adjoint mode. This quantity was introduced by Giannetti & Luchini (2007) as an upper bound for the eigenvalue variation $|\delta\lambda|$ induced by

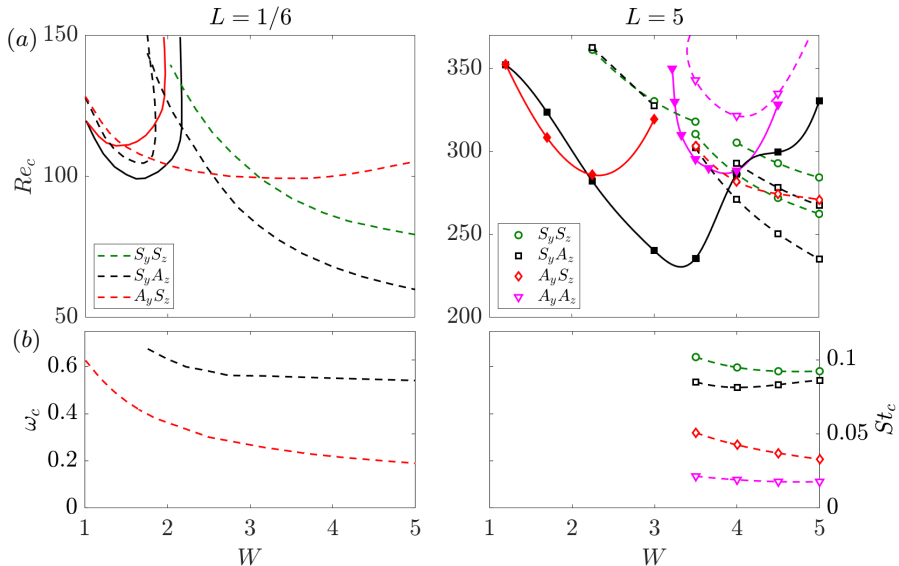


Figure 7: Same as figure 5, as a function of body width W , for the two body lengths $L = 1/6$ (left; data from Marquet & Larsson 2015) and $L = 5$ (right).

a specific perturbation of the LNS operator, namely a “force-velocity coupling” representing feedback from a localised velocity sensor to a localised force actuator at the same location. In this sense, the structural sensitivity is an indicator of the eigenvalue sensitivity and identifies the wavemaker (Monkewitz et al. 1993). The most sensitive regions, where the direct and adjoint modes overlap, are found in the near wake of the body for all modes, which is typical of bluff body wakes. As expected, these regions with large sensitivity are symmetric with respect to both y and z .

All the S_y modes, which preserve the left/right symmetry, are most sensitive in two regions located symmetrically with respect to the horizontal symmetry plane $z = 0$. For oscillatory S_y modes, observed for smaller L/W , the structural sensitivity is maximum exactly on the $u_0 = 0$ isosurface, in two flat and elongated regions separated by more than one body height; see also the cross-sections in figures 35–36 in appendix A. By contrast, for stationary S_y modes observed for larger L/W , the structural sensitivity is maximum inside the backflow region, in more compact regions located closer to the horizontal plane.

Stationary $A_y S_z$ modes are most sensitive in two regions located symmetrically with respect to the vertical symmetry plane $y = 0$, and the structural sensitivity is maximum inside the backflow region.

The peculiar oscillatory $A_y S_z$ mode observed for short lengths and intermediate widths (e.g. $L = 1$, $W = 2.25$) has a more convoluted structural sensitivity, that is maximum outside and near the downstream end of the backflow region.

3.4. Weakly nonlinear analysis

In section 3.2 we have investigated the linear stability of the $S_y S_z$ steady base flow, characterising the different eigenmodes that become unstable. It is worth emphasising that, when Re increases past the first bifurcation, the linear stability of the base flow is not necessarily relevant. Rigorously speaking, to detect

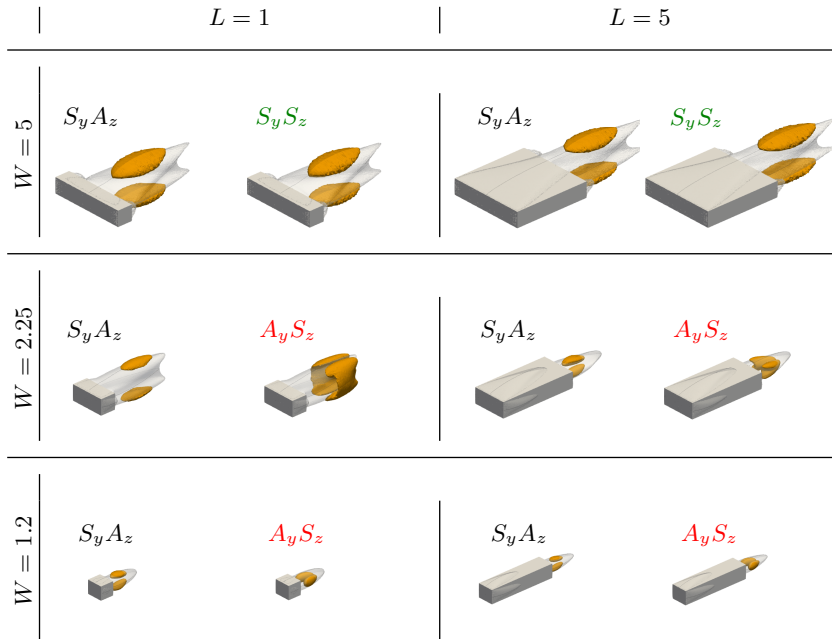


Figure 8: Structural sensitivity of the first (left) and second (right) bifurcating eigenmodes: representative isosurfaces of $\|\hat{\mathbf{u}}_1\| \|\hat{\mathbf{u}}_1^\dagger\|$ (opaque orange). The isosurface $u_0 = 0$ is reproduced from figure 2 (translucent grey).

secondary bifurcations one should study the linear stability of the nonlinearly bifurcated state itself (e.g. static deflected wake or periodic vortex shedding) or use nonlinear simulations. For instance, the onset of the 3D instability in the 2D cylinder wake can be predicted using Floquet analysis of the 2D limit cycle for $Re > 47$ (Barkley & Henderson 1996). When the base flow is unstable to at least two eigenmodes, the nonlinear flow can certainly not be predicted based only on the growth rates or critical Reynolds numbers of these modes. In some cases, weakly nonlinear analysis is able to capture the dominant nonlinear interactions between competing modes, then providing a very useful reduced order model (a set of scalar amplitude equations) able to inform about the types of bifurcations (e.g. subcritical or supercritical), the different bifurcated flows and their linear stability, ranges of multi-stability and hysteresis, etc. For example, Zampogna & Boujo (2023) found that for the flow past an Ahmed body (3D rectangular prism with $L = 3$, $W = 1.2$ and rounded leading edges), where a steady $S_y A_z$ mode becomes linearly unstable before a steady $A_y S_z$ mode, the weakly nonlinear analysis correctly predicts that the vertically and horizontally deflected wakes exchange their stability as Re increases.

In this section, we perform a weakly nonlinear analysis to study the flow behaviour in the vicinity of codimension-two points, where two eigenmodes become unstable simultaneously. Anticipating on the DNS (section 4), we focus on $(L, W) = (5, 1.2)$ and $(5, 2.25)$. For each of these two geometries, the top/bottom ($S_y A_z$) and left/right ($A_y S_z$) symmetry-breaking eigenmodes undergo a stationary bifurcation at close Re values. The method is the same as in Zampogna & Boujo (2023) (see Appendix C for details about the derivation). In short, we use the technique of multiple scales. We introduce a small parameter ϵ^2

quantifying the departure from criticality $Re_c^{-1} - Re^{-1}$, expand the flow field as a power series in ϵ , introduce slow time scales $\epsilon^2 t, \epsilon^4 t \dots$, and use a small-amplitude shift operator meant to bring the two bifurcations at the same critical Reynolds number Re_c . By injecting all this in the Navier-Stokes equations and collecting like-order terms in ϵ , we obtain a series of linear problems to be solved successively. A set of two coupled equations for the slowly-varying amplitudes of the $S_y A_z$ and $A_y S_z$ modes, i.e. A and B respectively, is then obtained by imposing non-resonance conditions (Fredholm alternative). Remarkably, although their coefficients are computed at $Re = Re_c$ only, these ordinary differential equations can be solved very easily and yield stable and unstable solutions (A, B) as a function of Re (assumed sufficient close to Re_c).

For $(L, W) = (5, 1.2)$, we obtain the third-order amplitude equations

$$d_t A = \lambda_A A - \chi_A A^3 - \eta_A A B^2, \quad (3.1)$$

$$d_t B = \lambda_B B - \chi_B B^3 - \eta_B A^2 B. \quad (3.2)$$

See Appendix C for the expressions of the λ, χ and η coefficients. The above system has four possible equilibrium solutions ($d_t A = d_t B = 0$): (i) symmetric base flow $(A, B) = (0, 0)$ described in section §3.1, (ii) pure vertical deflection $(A, 0)$, (iii) pure horizontal deflection $(0, B)$, and (iv) mixed state (A, B) . Note that (3.1)-(3.2) is invariant under reflections $A \rightarrow -A$ and $B \rightarrow -B$, so we discuss only $A \geq 0$ and $B \geq 0$. The linear stability of each state is determined by computing the eigenvalues of the 2×2 Jacobian of (3.1)-(3.2) linearised about the state of interest. Here, we obtain the bifurcation diagram of figure 9(a). The symmetric state $(A, B) = (0, 0)$ is stable up to $Re \approx 352$, when the $S_y A_z$ eigenmode becomes unstable and the flow settles to a vertically deflected state $(A, 0)$. Almost at the same Re , the $A_y S_z$ eigenmode becomes unstable, but the horizontally deflected state $(0, B)$ is initially unstable. Near $Re \approx 353$, there is an exchange of stability between states $(A, 0)$ and $(0, B)$, i.e. the wake leaves the vertically deflected state and enters a horizontally deflected state. In the very narrow range of bistability between these two states, a mixed state (A, B) exists, but is unstable. Qualitatively, the bifurcation scenario is similar to that found by Zampogna & Boujo (2023) for Ahmed bodies of dimensions $(L, W) = (3, 1.2)$ and a range of close-by geometries.

For $(L, W) = (5, 2.25)$ we find a subcritical pitchfork bifurcation of the $A_y S_z$ mode. In this case, leading-order nonlinearities do not lead to saturation but instead make the system more unstable, so (3.1)-(3.2) does not yield a stable solution. This calls for the inclusion of higher-order nonlinearities to capture saturation, so we derive the fifth-order amplitude equations

$$d_t A = \lambda_A A - \chi_A A^3 - \eta_A A B^2 + \kappa_A A B^4 + \beta_A A^3 B^2 + \gamma_A A^5, \quad (3.3)$$

$$d_t B = \lambda_B B - \chi_B B^3 - \eta_B A^2 B + \kappa_B A^4 B + \beta_B A^2 B^3 + \gamma_B B^5. \quad (3.4)$$

The above system has the same type of equilibrium solutions as previously described. However, the pure deflected states may each have one or two different amplitudes $(A_1, 0)$ and $(A_2, 0)$, and $(0, B_1)$ and $(0, B_2)$; similarly, up to four mixed states may exist, (A_i, B_i) , $i = 1, 2$. Here, we obtain the bifurcation diagram of figure 9(b). The symmetric state $(A, B) = (0, 0)$ is stable up to $Re \approx 282$, when the $S_y A_z$ eigenmode becomes unstable and the flow settles to a vertically deflected state $(A, 0)$. This first bifurcation is supercritical, so there exists only one such state. At $Re \approx 286$ the $A_y S_z$ mode becomes unstable, and this second

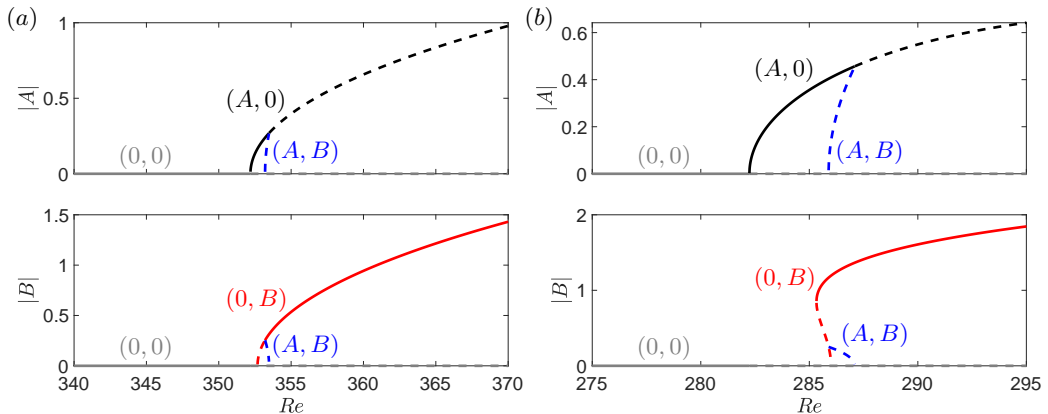


Figure 9: Bifurcation diagrams obtained from weakly nonlinear analysis in the vicinity of codimension-two steady bifurcations. A and B are the amplitudes of the top/bottom ($S_y A_z$) and left/right ($A_y S_z$) symmetry-breaking eigenmodes, respectively. Solid and dashed lines denote stable and unstable branches, respectively. (a) $L = 5, W = 1.2$; (b) $L = 5, W = 2.25$.

bifurcation is subcritical: the branch $(0, B)$ is initially unstable and moves towards lower Reynolds numbers, before becoming stable again and folding back to larger Reynolds number. One mixed state (A, B) exists but is unstable. The state $(A, 0)$ becomes unstable at $Re \approx 287$, leaving $(0, B)$ as the only stable state. Therefore, there is a narrow interval of bistability between the vertically and horizontally deflected states.

4. Three-dimensional nonlinear simulations

In this section, we use 3D, unsteady, fully nonlinear simulations to explore the successive bifurcations observed in the flow past elongated prisms with $L = 5$ and $W = 1.2, 2.25$ and 5 up to $Re = 700$. The specific value $L = 5$ is chosen as it defines the international BARC benchmark (Bruno et al. 2014). To identify the different regimes, hereafter we use the notation $xY_z Z_z$: the lower case x determines whether the regime is steady (s), periodic (p) or aperiodic (a); the upper case Y and Z determine the planar symmetries of the flow, i.e. whether the flow is symmetric (S) or antisymmetric (A) with respect to the y and z axis. When the flow is unsteady the symmetry refers to the time-averaged flow. As an example, the $sS_y S_z$ regime refers to a steady regime that retains the top/bottom and left/right planar symmetries, as the low- Re symmetric state shown in section 3.1. For $W = 2.25$ and $W = 5$, the $pS_y S_z l$ and $pS_y S_z t$ regimes refer to periodic regimes characterised by shedding of vortices from the leading-edge (l) and trailing-edge (t) shear layers respectively. Hereafter, blue, green and red symbols/lines are used for steady, periodic and aperiodic regimes respectively.

4.1. Narrow prism: $W = 1.2$

For $L = 5$ and $W = 1.2$ five different regimes are identified when the Reynolds number is increased up to $Re = 700$. This is conveniently visualised in figure 10, where the aerodynamic forces are shown as a function of Re . For $Re \lesssim 352$ the flow is steady and retains the $S_y S_z$ symmetry, in agreement with the linear stability

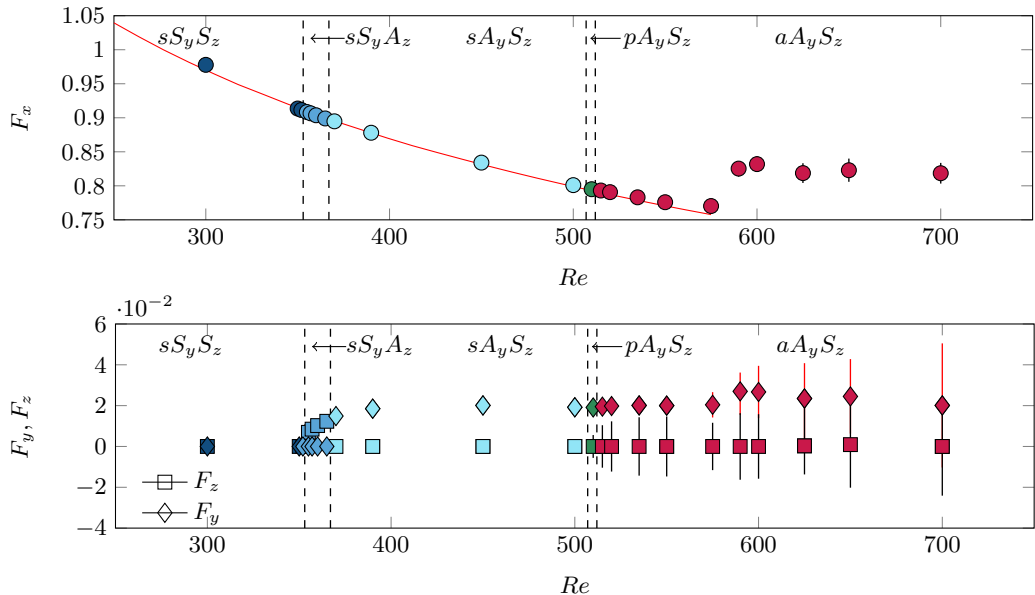


Figure 10: Dependence of the aerodynamic forces on the Reynolds number for $L = 5$ and $W = 1.2$. The circles refer to the average value, while the bars to the root mean square of the fluctuations. Top: Streamwise force F_x . Bottom: Lateral forces F_y and F_z . The red line in the top panel is for $8.47 \times Re^{-0.3799}$.

analysis presented in section 3.2. At $Re \approx 355$ the $sS_y S_z$ regime is unstable, and the flow experiences a pitchfork bifurcation towards the $sS_y A_z$ regime. The flow loses the top/bottom planar symmetry, but retains the left/right one. For $Re \gtrsim 370$ the steady $A_y S_z$ mode becomes unstable, and the flow enters the $sA_y S_z$ regime. The flow recovers the top/bottom planar symmetry, but loses the left/right one. This regime remains stable up to $Re \approx 500$, when the flow becomes unsteady. The flow approaches first the periodic $pA_y S_z$ regime, characterised by an alternating shedding of hairpin vortices from the top and bottom LE shear layers. For $Re \geq 515$ the wake starts flapping and the flow enters the aperiodic $aA_y S_z$ regime.

4.1.1. Low Re : Steady $sS_y A_z$ and $sA_y S_z$ regimes

The nonlinear simulations show that the primary bifurcation breaks the top/bottom planar symmetry leading to the steady $sS_y A_z$ regime, similarly to what was observed for shorter bodies (Marquet & Larsson 2015; Zampogna & Boujo 2023). This bifurcation occurs at $Re \approx 355$, in agreement with the critical Reynolds number $Re_c = 353$ found in section 3.2. The simulations show that for $Re \gtrsim 365$, the steady $A_y S_z$ mode dominates, and the flow recovers the top/bottom planar symmetry but loses the left/right one, as predicted by the WNL analysis. We observe a small discrepancy between the linear and WNL stability analyses ($Re_c \approx 355$) and the fully nonlinear simulations ($Re_c \approx 365$).

To characterise the $sA_y S_z$ and $sS_y A_z$ regimes, figure 11 shows isosurfaces of positive (red) and negative (blue) values of the streamwise vorticity, and illustrates the loss of the planar symmetries. This is similar to what is observed in the wake past disks, spheres and bullet-shaped bodies at Reynolds numbers larger than $Re \approx 115, 210$ and 350 (Johnson & Patel 1999; Tomboulides & Orszag 2000;

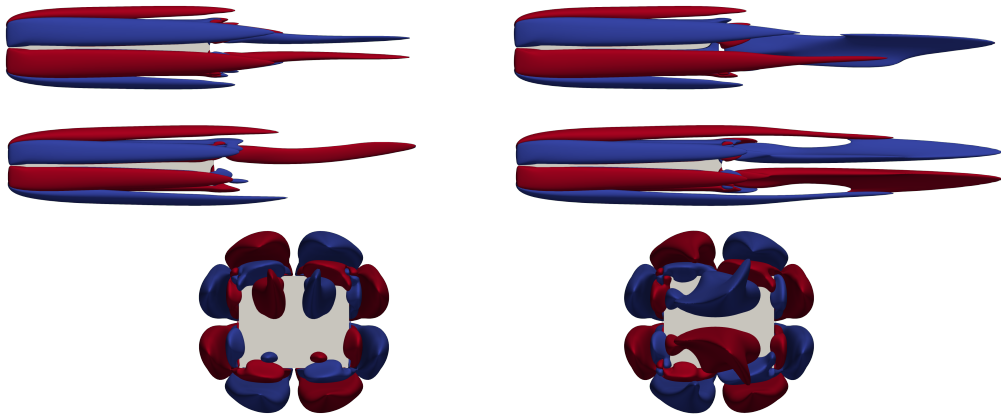


Figure 11: Isocontours of streamwise vorticity with the red/blue surfaces indicating $\omega_x = \pm 0.075$. Left: $sS_y A_z$ regime at $Re = 355$. Right: $sA_y S_z$ regime at $Re = 370$. Top: $x - z$ plane. Centre: $x - y$ plane. Bottom $y - z$ plane.

Fabre et al. 2008; Bohorquez et al. 2011). In these regimes, referred to as steady state in the case of axisymmetric bodies (Fabre et al. 2008; Bohorquez et al. 2011), a pair of counter rotating steady streamwise vortices arise in the wake that are absent at lower Reynolds numbers. These streamwise vortices are not aligned with the flow, but exhibit an eccentricity that increases with the distance from the trailing edge. In the $sS_y A_z$ regime the eccentricity is in the z direction, while in the $sA_y S_z$ regime it is in the y direction. For ellipsoids Magnaudet & Mougin (2007) found that the amount of streamwise vorticity that the body injects in the wake plays a crucial role in destabilising the flow.

The $sS_y A_z$ and $sA_y S_z$ flow regimes are further visualised in figure 12, where the streamwise velocity is plotted in the $z = 0$ and $y = 0$ planes, together with streamlines of the in-plane velocity components. Green circles are used for the elliptical stagnation points corresponding to a local maximum or minimum of the two-dimensional stream function ψ , and identify the centre of the recirculating regions; blue circles refer to hyperbolic stagnation points, corresponding to saddle points of ψ . In both the $sS_y A_z$ and $sA_y S_z$ regimes, the flow asymmetry is confined in the wake, confirming that the $A_y S_z$ and $S_z A_y$ global modes are unstable modes of the wake. Note, indeed, that the recirculating regions along the sides of the prism retain the planar symmetries in both regimes. These regions do not play a relevant role in the triggering mechanism of the primary instability, as confirmed by the results of the structural sensitivity shown in figure 8. A similar conclusion has been drawn for the primary instability of the flow past elongated two-dimensional rectangular cylinders by Chiarini et al. (2021), although in that case it consists of a Hopf bifurcation towards an unsteady regime.

Figure 13 shows that when the flow bifurcates to the $sS_y A_z$ and $sA_y S_z$ regimes, the drag decreases according to a power law, i.e. $F_x \sim Re^\alpha$ with $\alpha = -0.3799$. This is similar to what is observed for the flow around a sphere (Johnson & Patel 1999) or a short circular cylinder (Yang et al. 2022). In this case the decrease of F_x is entirely due to a decrease of the friction contribution $F_{x,f}$ (see the bottom left panel of figure 13), as the pressure contribution $F_{x,p}$ does not change with Re . An increase of Re , indeed, results into a downstream shift of the flow reattachment point x_r over the sides of the prism, leading to a longer recirculating region and

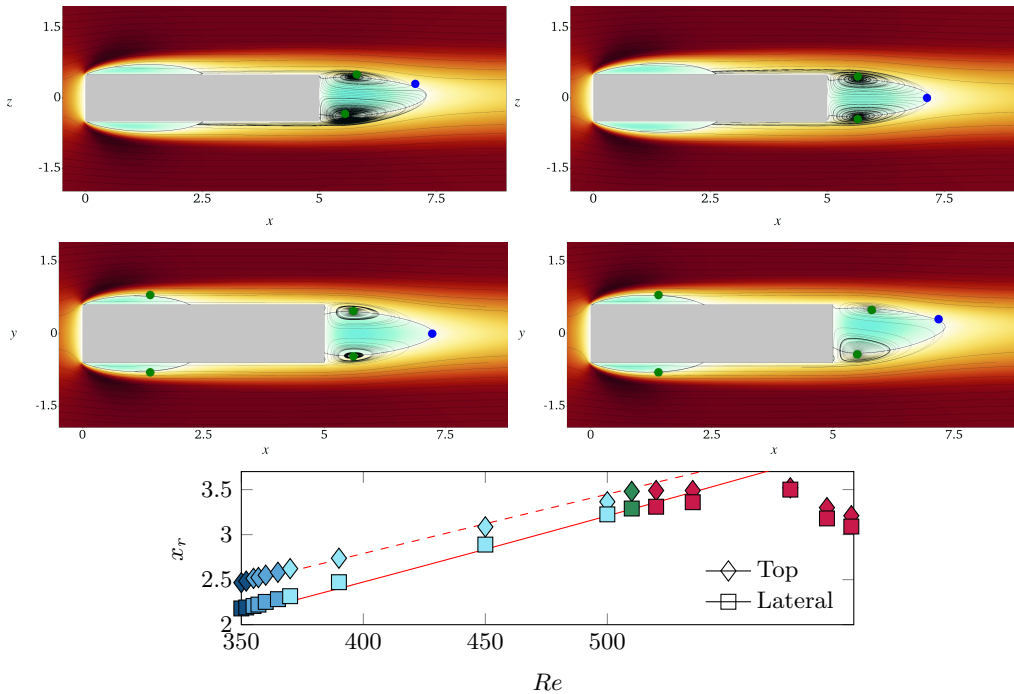


Figure 12: Top panels: contour of the streamwise velocity in the $y = 0$ (top) and $z = 0$ (bottom) planes, together with streamlines of the in-plane velocity components. Left: $Re = 355$, $sS_y A_z$. Right: $Re = 370$, $sA_y S_z$. The symmetric blue-to-red colourmap covers $-1.2 \leq u \leq 1.2$. Green and blue circles identify the elliptical and hyperbolic stagnation points, respectively. Bottom panel: position of the reattachment point x_r over the top and lateral sides as a function of Re ; the red solid line is for $0.0023 \times Re^{1.1651}$, while the red dash line is for $0.0095 \times Re^{0.9485}$. In the unsteady regimes for $Re > 500$, x_r refers to the reattachment point of the time averaged flow.

to a decrease of $F_{x,f}$ (see the bottom panel in figure 12). We note that a power function fits well the relation between x_r and Re , being $x_r \sim Re^{1.1651}$ for the lateral sides and $x_r \sim Re^{0.9485}$ for the top and bottom sides. In contrast, the non-zero cross-stream component of the aerodynamics forces increases as Re increases, being for example $F_y \approx 0.01$ for $Re = 360$ and $F_z \approx 0.02$ for $Re = 450$. Unlike for F_x , this is due to an increase of both the friction and pressure contributions (see the bottom right panel of figure 13), and is associated with the increasing flow asymmetry.

The regular bifurcation towards an asymmetric steady flow is found for prisms with small W only, irrespective of L (section 3.2). This is the case of many other 3D bluff bodies: besides the largely studied axisymmetric sphere and disk, the existence of a regular bifurcation in non-axisymmetric flows has been reported by Marquet & Larsson (2015) for thin plates with $W/D < 2$, by Yang et al. (2022) for short circular cylinders with $W/D < 1.75$, and by Sheard et al. (2008) for short cylinders with hemispherical ends. The main difference is that, after the regular bifurcation, the wake retains a symmetric plane that is randomly oriented (selected by numerical or experimental perturbations; Tomboulides & Orszag 2000) for axisymmetric bodies, but dictated by the planar symmetries of the geometry for non-axisymmetric bodies.

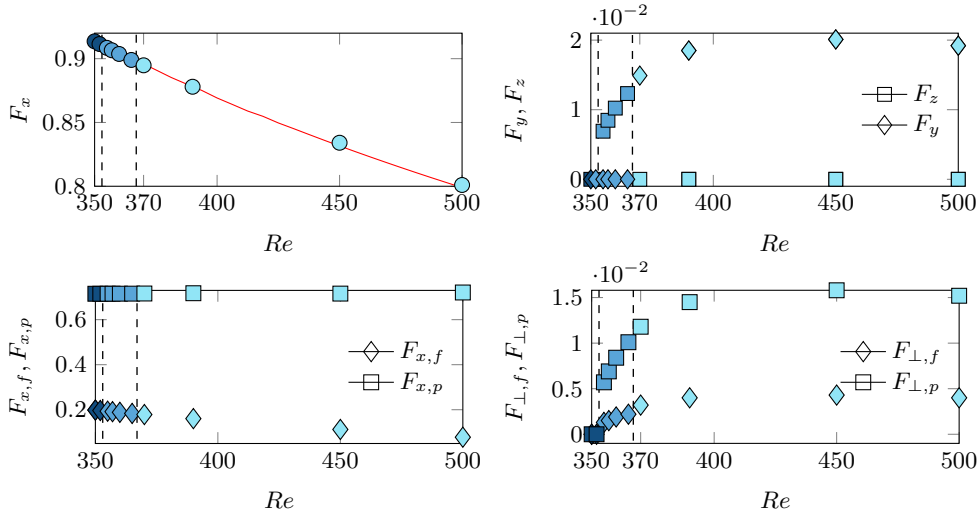


Figure 13: Dependence of the aerodynamics forces on Re for the sS_yS_z , sS_yA_z and sA_yS_z regimes for $W = 1.2$. The top panels are for the total forces. The bottom panels separate the viscous and pressure forces. F_{\perp} in the bottom right panel denotes the single non-zero force component perpendicular to the incoming flow, i.e. F_z for the sS_yA_z regime and F_y for the sA_yS_z regime. The red line in the top left panel is for $8.47 \times Re^{-0.3799}$.

4.1.2. Large Re : pA_yS_z and aA_yS_z regimes

A further bifurcation occurs at $Re \approx 510$. It consists of a Hopf bifurcation: the flow becomes unsteady and starts oscillating about the deflected sA_yS_z regime. A similar regime, with the flow oscillating about an asymmetric steady state has been observed for the flow past a sphere (Johnson & Patel 1999), the flow past a cube (Saha 2004), the flow past a disk (Meliga et al. 2009) and the flow past a short cylinder (Pierson et al. 2019). Interestingly, when considering the time-average forces, the decreasing power law that fits F_x and Re in the sS_yS_z , sS_yA_z and sA_yS_z regimes holds also in the unsteady regime for intermediate Reynolds numbers up to $Re = 575$ (figure 10). For these Re , indeed, the time average flow field — and its dependence on Re — resembles the steady sA_yS_z regime. The average size of the recirculating regions over the lateral sides increases with the Reynolds number, as shown in figure 12 by means of the reattaching point x_r . For larger Re the structure of the time average flow changes, and F_x increases. For $Re \geq 575$, indeed, the average $x_r(Re)$ deviates from the power law found at smaller Re : the lateral recirculating regions shrink as Re increases (figure 12).

The dynamics of the flow progressively changes as Re increases. At $Re = 510$ the flow enters the periodic pA_yS_z regime, which is characterised by an alternating shedding of hairpin vortices from the top and bottom LE shear layers (see the top panels of figure 15). At this Re a single peak is found in the frequency spectrum of F_z , i.e. $St \approx 0.277$, while F_y remains practically constant in time (figure 14). The attractor draws a limit cycle in the phase space.

For $Re \gtrsim 515$ a frequency $St \approx 0.0776$ appears in the spectrum of F_y , and the flow becomes aperiodic. Here the flow is characterised by a superposition of two different modes, (i) the shedding of hairpin vortices from the top and bottom LE shear layers (with $St \approx 0.28$), and (ii) the flapping motion of the wake in the

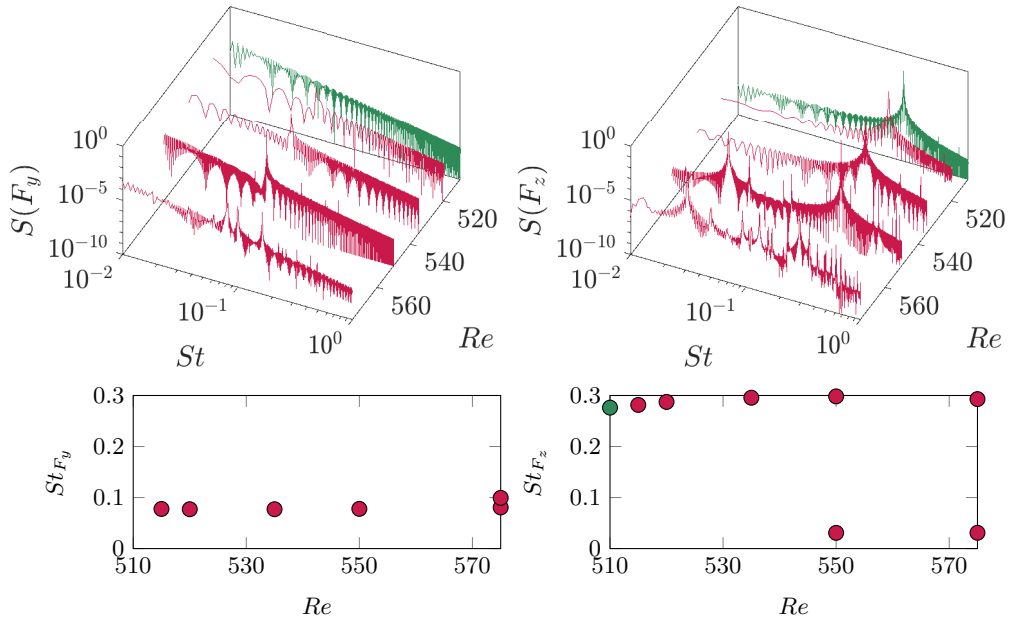


Figure 14: Frequency content for $W = 1.2$ and $510 \leq Re \leq 575$. Top: frequency spectra for F_y (left) and F_z (right). Bottom: dependence of the main frequency on the Reynolds number for F_y (left) and F_z (right). To ease the visualisation in the top panels only five Reynolds numbers are considered.

y direction (with $St \approx 0.08$); see figure 16 and the related discussion. The two frequencies are not commensurate and, as shown in the force diagrams in the right panels of figure 15, a torus replaces the limit cycle in the phase space. Note that as Re increases the $St \approx 0.28$ spectrum peak progressively decreases, while the $St \approx 0.077$ one progressively increases. The flow dynamics is mainly driven by the shedding of the hairpin vortices at low Re , while the wake flapping motion dominates at large Re .

For $Re \geq 550$ the wake flaps also in the z direction, and a further frequency $St \approx 0.03$ appears in the spectrum of F_z (figure 15). The different Re at which the two oscillating modes arise agree with the results of the linear stability analysis, which reveals that (for $L \leq 2$) the unsteady $A_y S_z$ wake mode becomes unstable at smaller Re compared to the unsteady $S_y A_z$ mode as long as $W \geq H$. When Re is further increased the different modes nonlinearly interact and the flow becomes progressively more chaotic (see the bottom panels of figure 15).

To examine the spatial structure of the different modes and relate them with the flow frequencies, we use proper orthogonal decomposition (POD); see appendix D for details. Figure 16 considers $Re = 515$. As shown in the top panels, the dominant POD modes are associated with the same frequencies found in the frequency spectra (figure 14) and with their multiples. The POD modes come in pairs (i.e. with same single values and frequencies), as typical for oscillating structures. Mode 1 is associated with $St \approx 0.28$, and a shedding of vortices from the top and bottom sides is clearly visible in its spatial structure. Mode 3, instead, is associated with $St \approx 0.07$. Its spatial structure is confined in the

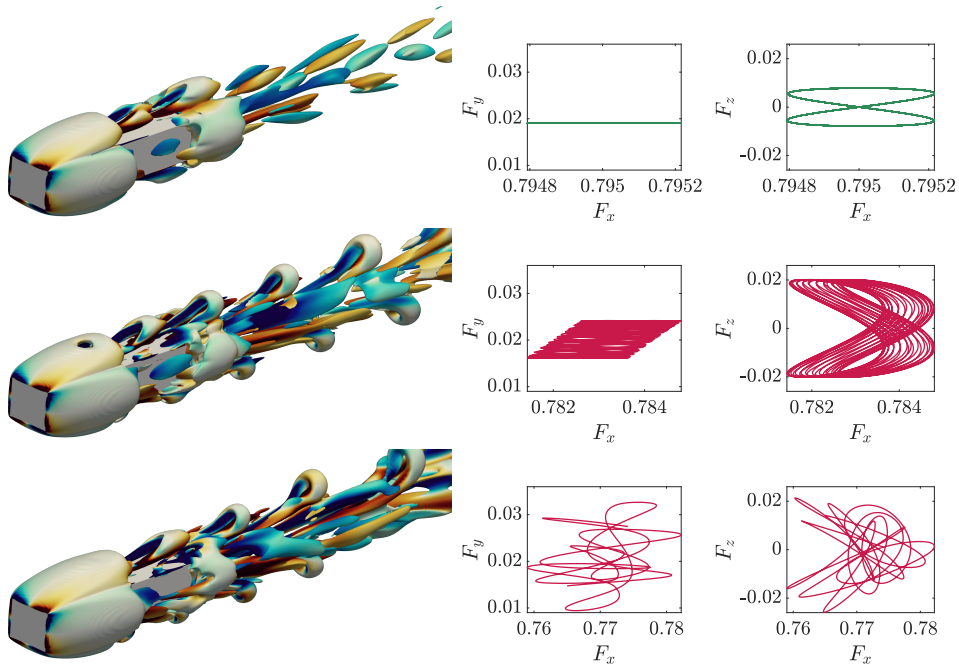


Figure 15: Structure of the flow for $W = 1.2$ and $510 \leq Re \leq 575$. Left: instantaneous snapshot; isosurfaces of $\lambda_2 = -0.05$ coloured with the streamwise vorticity in the $-1 \leq \omega_x \leq 1$ range. Right: force diagrams. From top to bottom: $Re = 510$, $Re = 535$ and $Re = 575$.

wake and breaks the left/right symmetry consistently with a flapping mode of the wake in the y direction about a $A_y S_z$ state.

For elongated prisms with $W = 1.2$ and $L = 5$, the wake flapping frequencies are smaller compared to the characteristic frequencies of the flow past a sphere, e.g. $St \approx 0.129$ at $Re = 270$ (Tomboulides & Orszag 2000), and a short cylinder, e.g. $St \approx 0.125$ at $Re = 283$ (Yang et al. 2022). This is consistent with the linear stability results in figure 5, that point out a decrease of St with L . It is also worth mentioning that a shedding of hairpin vortices has been already observed in the flow past other (short) bluff bodies; see for example Tomboulides & Orszag (2000) for the sphere, Yang et al. (2022) for short cylinders and Saha (2004) for the cube. As detailed in Saha (2004), however, for short bodies the hairpin vortices are generated in the wake, after the large-scale vortices shed from the body are convected downstream. In contrast, for the considered elongated prisms, the hairpin vortices form over the sides of the prism, and are related to the dynamics of the side recirculating regions. A closer look on their generation, growth and downstream advection is provided later in section 4.2.3, when discussing the periodic $pS_y S_z l$ regimes observed for intermediate widths.

4.2. Intermediate width: $W = 2.25$

For $L = 5$ and $W = 2.25$ the scenario becomes more complicated, with many regimes identified for Reynolds numbers up to $Re = 700$; see figure 17. In agreement with the linear stability analysis (section 3.2), the critical Reynolds number corresponding to the onset of the first bifurcation decreases with the width of the prism. For $W = 2.25$ the primary instability consists of a pitchfork

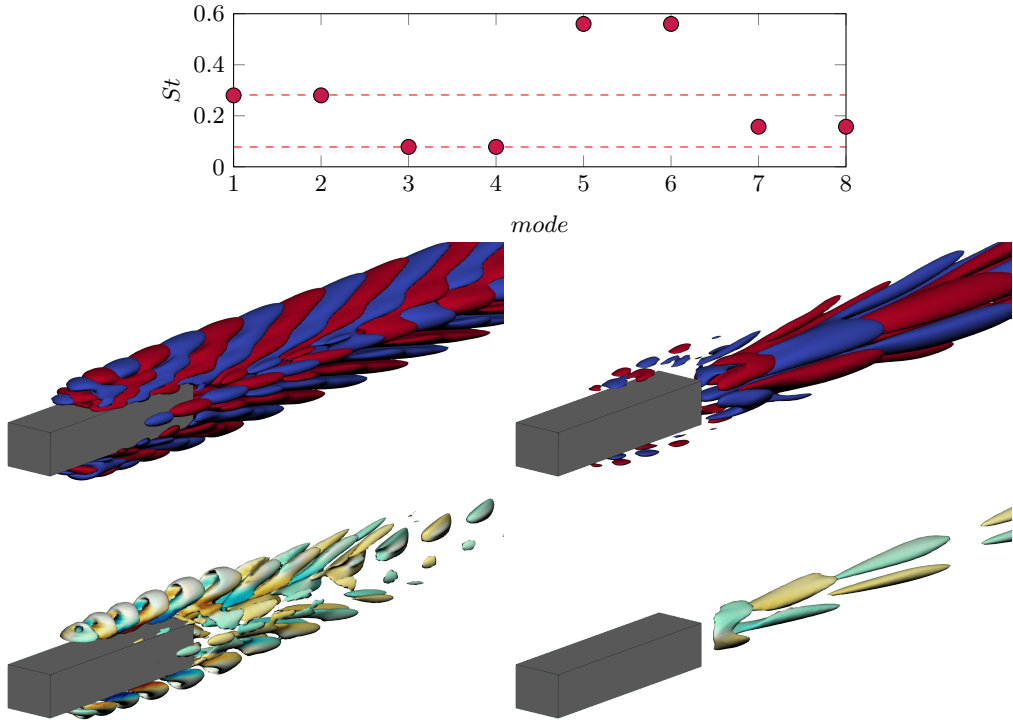


Figure 16: POD analysis for $W = 1.2$ and $Re = 515$. Top: frequency associated with the first 8 POD modes, ordered by decreasing singular value (i.e. decreasing energy fraction). The dashed lines are the main DNS frequencies, also shown in figure 14. Central and bottom panels: visualisation of the POD modes 1 (left) and 3 (right). Centre: Isosurfaces of $\omega_y \pm 0.5$. Bottom: isosurfaces of $\lambda_2 = -0.5$ coloured with the streamwise vorticity.

bifurcation towards the steady sS_yA_z regime, and occurs between $Re = 250$ and $Re = 290$, which is smaller than $Re_c \approx 352$ found for $W = 1.2$. At larger Re , another bifurcation at $Re \approx 300$ restores the top/bottom planar symmetry and breaks the left/right one, thus leading to the sA_yS_z regime, similar to smaller W . The simulations show an hysteresis in the transition from sS_yA_z to sA_yS_z . Bistability is detected for some values of Re , in agreement with the subcritical nature of the bifurcation (see the WNL analysis in section 3.4). Interestingly, at larger Re the flow recovers both planar symmetries and settles again in a sS_yS_z regime, before becoming unsteady at $Re \approx 375$ with a combination of two different modes, i.e. a flapping of the wake and a symmetric shedding of hairpin vortices from the top and bottom LE shear layers. As Re further increases, the wake flapping mode first stabilises, leading to the periodic pS_yS_zla and pS_yS_zlb regimes, and then destabilises again at larger Re , leading eventually to the aperiodic aS_yS_z regime.

4.2.1. Low Re : Steady regimes sS_yA_z and sA_yS_z

The nonlinear simulations show that the flow is steady and retains the S_yS_z symmetry for $Re \lesssim 290$, in agreement with the results of the linear stability analysis. At $Re \approx 290$ the flow undergoes a regular bifurcation towards the steady sS_yA_z regime, similarly to what was found for $W = 1.2$. Further increasing the

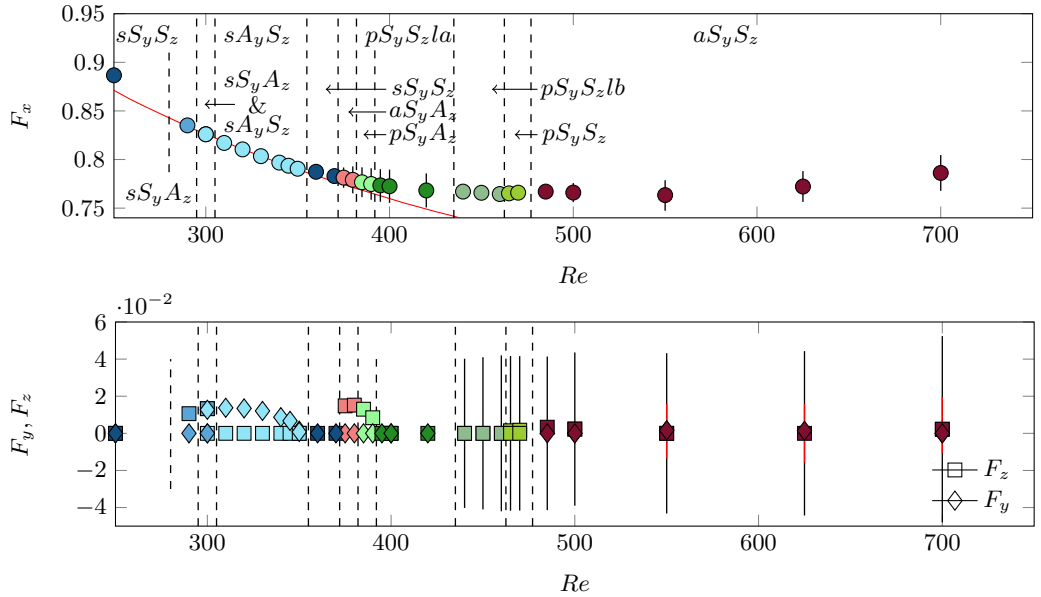


Figure 17: As figure 10, but for $L = 5$ and $W = 2.25$. The red line in the top panel is for $4.33 \times Re^{-0.2905}$.

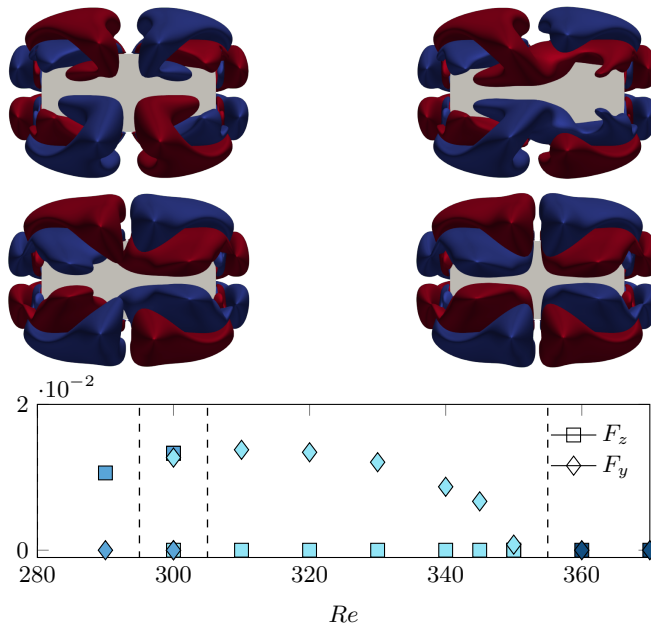


Figure 18: Transition from the sS_yA_z to the sS_yS_z regime for $300 \leq Re \leq 360$. Back view of the $y-z$ plane. The red and blue isosurfaces are for $\omega_x = \pm 0.1$. Top left: $Re = 300$, regime sS_yA_z . Top right: $Re = 300$, regime sA_yS_z . Centre left: $Re = 330$, regime sA_yS_z . Centre right: $Re = 360$, regime sS_yS_z . Bottom: zoom of the bottom panel of figure 17 in the $280 \leq Re \leq 370$ range.

Reynolds number, the flow remains steady but recovers the top/bottom symmetry and loses the left/right one, i.e. enters the sA_yS_z regime. Unlike for smaller W , this bifurcation is hysteretic, and both the sS_yA_z and sA_yS_z regimes are simultaneously stable for a small range of $Re \approx 300$; see the top panels of figure 18 and the WNL analysis in section 3.4.

By increasing the Reynolds number in the $320 \leq Re \leq 350$ range, the flow asymmetry in the y direction decreases, and at $Re = 350$ the flow recovers the left/right planar symmetry; for $Re \approx 360$ the flow is steady and $F_y \approx F_z \approx 0$. This flow symmetrisation is shown in figure 18, by means of isocontours of streamwise vorticity. Like for $W = 1.2$ (figure 11), at $Re = 300$ a pair of counter-rotating streamwise vortices is found in the wake, with eccentricity in the y direction (see the sA_yS_z regime in the top right panel). As Re increases, a new pair of counter rotating vortices arises, becomes stronger and progressively pushes the other pair apart. Indeed, a new pair of isosurfaces with positive and negative ω_x arises at the left side of the TE, and the previous pair is shifted towards the right side of the prism (bottom left panel). Eventually, at $Re \approx 360$ the two pairs of vortices are placed symmetrically with respect to the z axis, and they have the same intensity (bottom right panel). At this Re the flow exhibits again both the top/bottom and left/right planar symmetries, and enters a sS_yS_z regime. This does not happen for $W = 1.2$, as two pairs of streamwise vortices with characteristic size H cannot be simultaneously accommodated at the TE when $W < 2H$.

In passing, we note that in the steady sS_yA_z , sA_yS_z and sS_yS_z regimes a decreasing power law fits well the relation between F_x and Re , being $F_x \sim Re^\alpha$ with $\alpha = -0.2905$. However, the agreement does not extend to the unsteady regime, as instead observed for $W = 1.2$. Also, like for smaller W , the decrease of F_x with Re is mainly due to the enlargement of the side recirculating regions (not shown).

4.2.2. Intermediate Re : aperiodic aS_yA_z and periodic pS_yA_z regimes

At $Re \approx 375$ the flow becomes unsteady. Unlike for smaller W , here the flow enters different regimes in short succession. This is conveniently visualised in figures 19 and 20, where the frequency content and the structure of the flow are shown for $375 \leq Re \leq 470$.

For $375 \leq Re \leq 380$, the flow approaches the aperiodic aS_yA_z state: unlike for smaller W , the flow oscillates about a S_yA_z state that retains the left/right symmetry and breaks the top/bottom one. The flow exhibits two non commensurate frequencies, being $St \approx 0.05$ and $St \approx 0.23$, and the attractor draws a torus in the phase space. As shown in the top left panel of figure 20, at this Re the flow behaviour is the result of the superposition of two different modes (see the following POD analysis), i.e. (i) an asymmetric flapping mode of the wake in the z direction with $St \approx 0.04$ and (ii) a symmetric and in-phase shedding of hairpin vortices from the top and bottom LE shear layers with $St \approx 0.23$. For $Re \approx 385$, instead, the flapping mode of the wake stabilises and the flow approaches the periodic pS_yA_z regime. The wake remains deflected in the z direction and the flow unsteadiness is only due to the in-phase shedding of hairpin vortices, with a frequency $St \approx 0.24$ that slightly increases with Re (see bottom panel of figure 19). A limit cycle replaces the torus in the phase space; see figure 20.

Like for $W = 1.2$, we use POD to examine the structure of the flow at $Re = 380$. In figure 21 we separate the modes responsible for the two non commensurate frequencies $St \approx 0.05$ and $St \approx 0.23$ detected in the frequency spectra. The

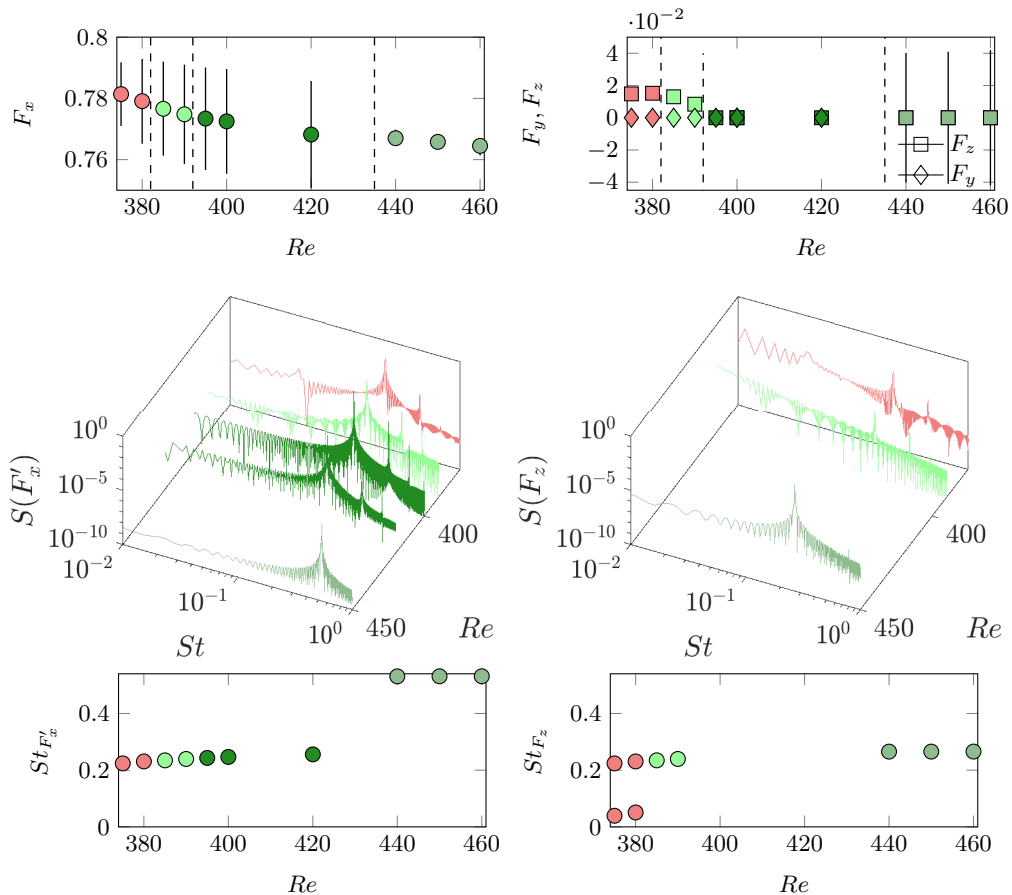


Figure 19: Forces and frequency content for $W = 2.25$ and $375 \leq Re \leq 450$. Top panels: zoom of the figure 17 in the $370 \leq Re \leq 460$ range. Note that in the $440 \leq Re \leq 460$ range the oscillations of F_x are small and the bars are not visible. Central panels: frequency spectra for $F'_x = F_x - \langle F_x \rangle_t$ (left) and F'_z (right); $\langle \cdot \rangle_t$ denote time average. To ease the visualisation, only five Re are considered. In the central right panel the $S(F'_z)$ spectra for $Re = 400$ and $Re = 420$ is not visible as the F_z fluctuations are almost null. Bottom: main frequencies for F'_x (left) and F'_z (right).

POD mode 1 is associated with $St \approx 0.23$, and its spatial structure shows a $S_y S_z$ shedding of hairpin vortices from the top and bottom sides of the prism. Mode 5, instead, matches the $St \approx 0.05$ frequency, with a $S_y A_z$ spatial structure that agrees with an asymmetric flapping mode of the wake in the z direction. Based on this, it seems that the aperiodic $a S_y A_z$ regime found at $Re \approx 380$ is the result of a superposition of an oscillatory $S_y A_z$ mode of the wake, that is unstable for a small range of Re only (at $Re \approx 385$ it is stable), and of an unsteady $S_y S_z$ mode of the LE shear layers. Interestingly, this interpretation is partially confirmed by the linear stability analysis, which indeed predicts an unsteady $S_y S_z$ mode to become unstable for $Re \gtrsim 350$ for this geometry, with a frequency that is compatible with $St \approx 0.2$ (figure 5). Also, the neutral curves (figure 5) show that for $L \leq 4$ an unsteady $S_y A_z$ mode of the wake with $St \approx 0.06 - 0.07$ becomes unstable, but for a small range of Re only. For $L \approx 4$, for example, the unstable range is between

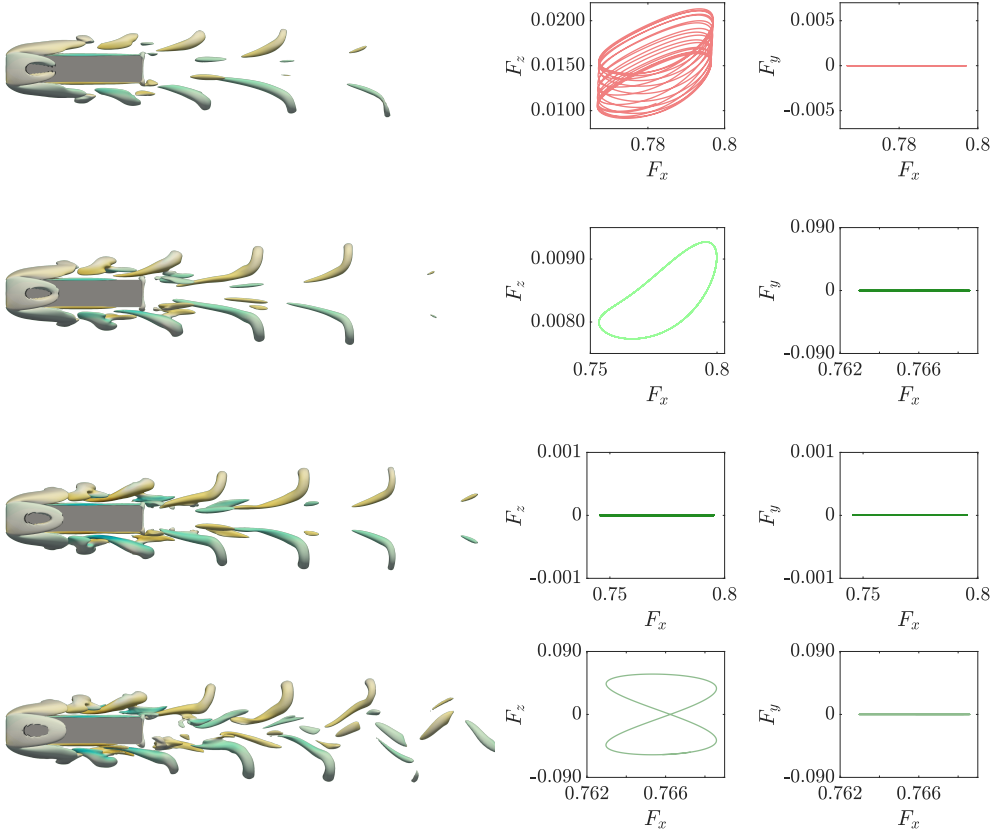


Figure 20: Structure of the flow for $W = 2.25$ and $375 \leq Re \leq 470$. Left: instantaneous visualisation of the flow structure by means of isocontours of $\lambda_2 = -0.25$ coloured with $-1 \leq \omega_x \leq 1$. Right: $F_z - F_x$ and $F_y - F_x$ force diagrams. From top to bottom $Re = 375$, $Re = 390$, $Re = 420$ and $Re = 450$.

$330 \lesssim Re \lesssim 350$. Recalling that these neutral curves refer to the low- Re sS_yS_z steady base flow, it is possible that due to nonlinear effects, an increase of Re extends this curve to $L = 5$, explaining this sudden destabilisation/stabilisation of the wake flapping mode.

4.2.3. Intermediate Re : periodic pS_yS_zl regime

As Re is further increased, the flow recovers once again the top/bottom planar symmetry, and for $390 < Re \leq 470$ it is in the periodic and symmetric pS_yS_zl regime; see figure 20. In this regime, two distinct behaviours can be further distinguished, based on the fluctuations of F_z .

For $390 < Re \leq 420$ the flow shows an in-phase shedding of hairpin vortices from the top and bottom LE shear layers, and the flow *instantaneously* retains the top/bottom and left/right planar symmetries (left panels of figure 20); this is regime pS_yS_zla . Accordingly, the unbalance of the viscous and pressure forces between the top/bottom and left/right sides is null at all times, leading to $F_z \approx F_y \approx 0$ (see the force diagrams in figure 20). To the best of our knowledge, such a

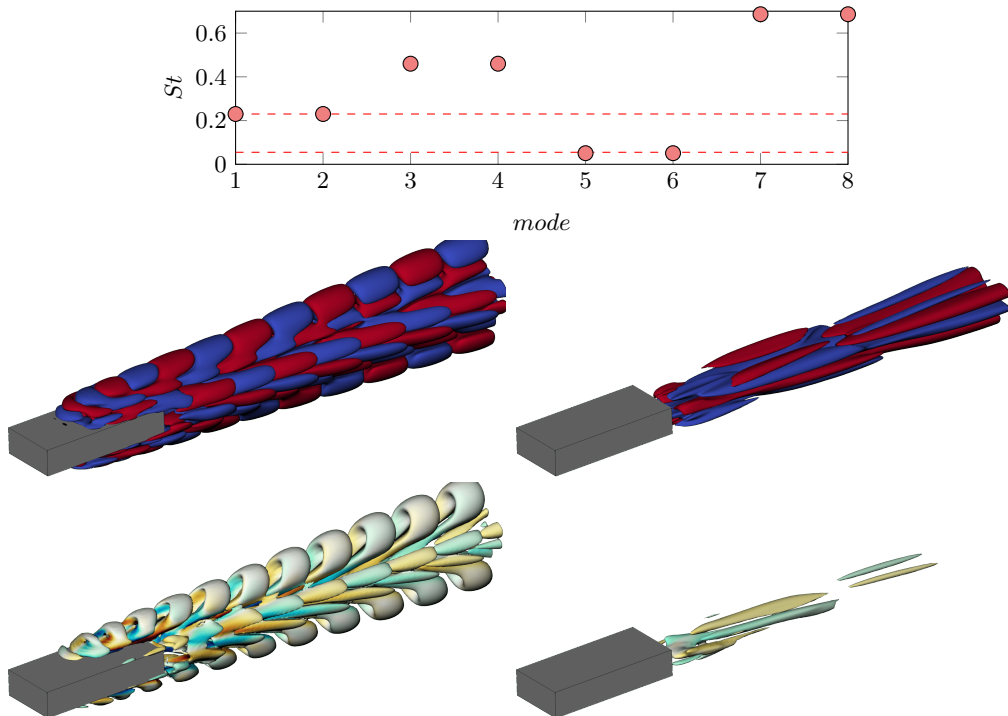


Figure 21: POD analysis for $W = 2.25$ and $Re = 380$. Top: frequency associated with the first 8 POD modes, ordered by decreasing singular value (i.e. decreasing energy fraction). The dashed lines are the frequencies as in figure 20. Central and bottom panels: visualisation of the POD modes 1 (left) and 5 (right). Centre isosurfaces of $\omega_y \pm 0.5$. Bottom: isosurfaces of $\lambda_2 = -0.5$ coloured with the streamwise vorticity.

vortex shedding that preserves all spatial symmetries at all times and generates neither lift force nor side force has not been reported.

For $420 < Re \leq 470$, instead, the flow remains periodic with $St \approx 0.24$, but the shedding of vortices from the top and bottom LE shear layers is in phase opposition (bottom left panel in figure 20); this is regime pS_yS_zlb . As a result, in this regime the flow retains the top/bottom planar symmetry in an average sense only, and the oscillations of F_z intensify.

We now consider regime pS_yS_zla and detail the dynamics of the hairpin vortices shed from the top and bottom LE shear layers. We use $Re \approx 400$. Figure 22 shows the flow structures at four different instants, which are taken equispaced in the $T = 1/St$ period of the shedding. A pair of hairpin vortices with vorticity of opposite sign is shed in phase from the top and bottom LE shear layers, with a spanwise wavelength λ_z dictated by the width of the prism $\lambda_z \approx W$. The top/bottom LE shear layers, indeed, periodically release tubes of negative/positive spanwise vorticity that, due to the vertical and spanwise velocity gradients, are modulated and form hairpin vortices. Due to the no-slip boundary condition on the sides of the prism, the central part of the tubes (head of the hairpin vortices) is convected downstream faster than the lateral parts (legs). Accordingly, the hairpin vortices induce low-speed velocity (negative velocity fluctuations) between their legs, and high-speed velocity (positive velocity fluctuations) in the outer region. Once

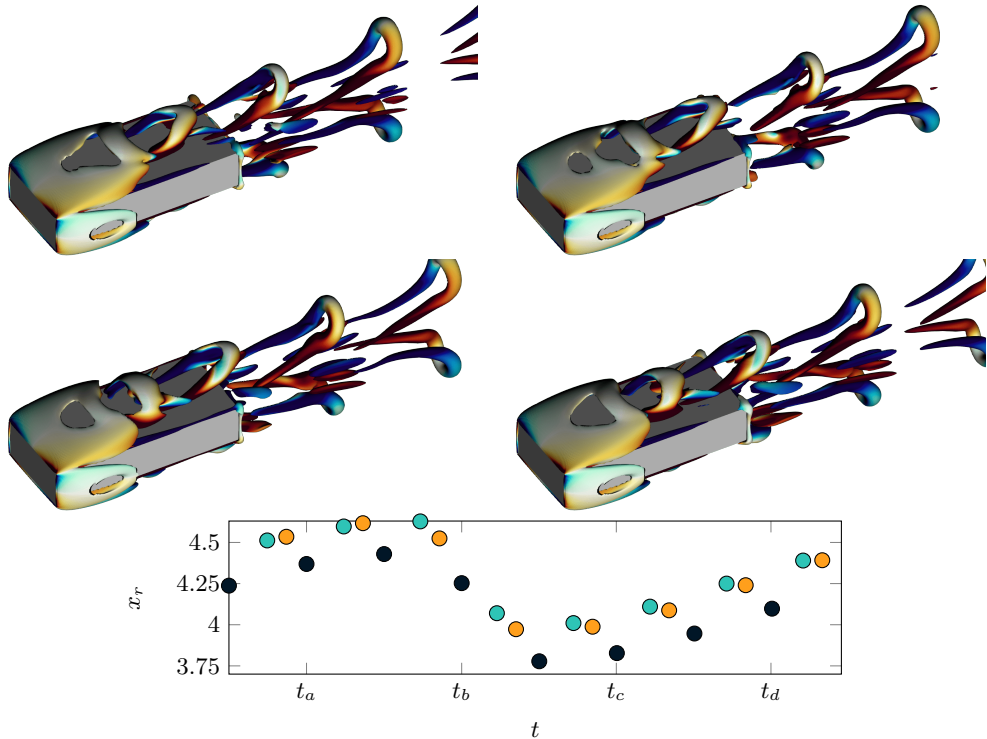


Figure 22: Top panels: Flow structure of the double symmetric pS_yS_zla flow regime for $L/H = 5$, $W/H = 2.25$ and $Re = 400$. Four snapshots are shown, separated in time by $T/4$, where T is the period of the shedding of hairpin vortices. In order the top four panels refer to t_a , t_b , t_c and t_d in the bottom panel. The isosurfaces are for $\lambda_2 = -0.05$ coloured with $-1 \leq \omega_x \leq 1$. Bottom panel: Time evolution of the reattachment point over the top/bottom of prisms with $W/H = 2.25$ at $Re = 400$ in the $z = 0$ plane. Black circles: sharp LE and $L/H = 5$. Green squares: sharp LE and $L/H = \infty$. Orange diamonds: rounded LE with $R = 1/64$ and $L/H = 5$.

generated, the two hairpin vortices are shed downstream and continue moving as a pair in the wake, where they progressively move apart in the z direction due to their mutual induction, until they are dissipated by viscosity. The shedding of hairpin vortices is accompanied by a periodic enlargement and shrinking of the top/bottom recirculation regions (black circles in figure 22). The recirculating regions enlarge while the leading-edge shear layers accumulate vorticity (x_r moves downstream), and suddenly shrink when the hairpin vortices are shed.

The shedding of hairpin vortices from the LE shear layers recalls what is observed in the flow past two-dimensional rectangular cylinders. In that case, two-dimensional spanwise aligned vortices are periodically shed from the leading-edge shear layers due to the so-called impinging-LE-vortex (ILEV) instability (Naudascher & Rockwell 1994). The ILEV instability is a resonant oscillation of the fluid. Vortices are shed periodically from the LE shear layer and, when a LE vortex passes over the TE, a pressure pulse is generated, travels upstream and triggers the shedding of a new LE vortex (Chiarini et al. 2022c). The flow frequency thus changes with the length of the body, and the dynamics of the LE and TE vortex shedding are synchronised. In the two-dimensional case, therefore,

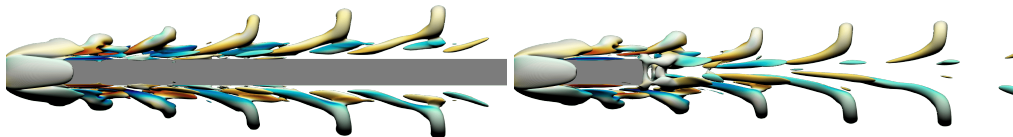


Figure 23: Lateral view of the flow structures for a rectangular prism of infinite length and $W = 2.25$ (left) and for a rectangular prism with $L = 5$ and $W = 2.25$ and rounded LE with $R = 1/64$ (right). For both cases the Reynolds number is set at $Re = 400$. For the rectangular prism of infinite length the flow approaches the pS_yS_zla regime. For the rectangular prism with $R = 1/64$ the flow approaches the pS_yA_z regime.

the shedding of vortices from the LE is not the result of an absolute instability of the LE shear layer, but it is interconnected with the dynamics of the TE vortex shedding (Hourigan et al. 2001; Chiarini et al. 2022c).

To investigate the role of the LE and TE shear layers in the mechanism that sustains the pS_yS_zla regime, two types of additional simulations have been carried out at $Re = 400$ for modified prism geometries. First, to isolate the LE shear layer from the interaction with the TE, we have considered a rectangular prism of infinite length and $W = 2.25$. As shown in the left panel of figure 23, the flow enters the pS_yS_zla regime in this case too, with a pair of hairpin vortices shed in phase from the top and bottom LE shear layers. Interestingly, the shedding frequency closely matches that found for $L = 5$, being $St \approx 0.24$. This indicates that for 3D prisms the triggering mechanism of the LE vortex shedding does not require the presence of a TE, as instead observed for 2D blunt bodies (Chaurasia & Thompson 2011; Thompson 2012). A possible feedback mechanism that triggers the formation of the hairpin vortices may be therefore embedded within the recirculating regions that arise over the top and bottom sides of the prism.

Second, to support this hypothesis we have considered rectangular prisms with $L = 5$ and $W = 2.25$, but with a rounded LE. Five curvature radii R have been considered, ranging from $R = 1/2$ (semicircular LE) to $R = 1/64$. For $R = 1/2$ the flow does not separate from the LE, and recirculating regions do not form over the top and bottom sides of the prism. In this case the flow approaches a steady and asymmetric sS_yA_z regime (not shown) and shedding of hairpin vortices from the LE is not detected. When a smaller R is considered, the flow separates from the LE, and recirculating regions with progressively larger size form over the top and bottom sides of the prism. However, the shedding of hairpin vortices is not detected up to $R = 1/64$. In this case the flow enters a periodic regime around the asymmetric S_yA_z state, which is characterised by the in-phase shedding of hairpin vortices from the top and bottom LE shear layers; see the right panel of figure 23. Again, the shedding frequency matches well that found for the sharp configuration, being $St \approx 0.238$. Overall, these additional simulations support the hypothesis that in the pS_yS_zl regime the shedding of hairpin vortices from the LE shear layers is the result of a feedback mechanism that takes place in the recirculating regions over the top and bottom sides of the prism, and that it does not require the presence of a TE.

4.2.4. Large Re : Aperiodic regime aS_yS_z

Increasing the Reynolds number up to $Re \geq 460$, the lateral and vertical flapping modes of the wake become unstable, and the flow progressively enters the chaotic regime; see figure 24 and 25. Unlike for smaller W , for $500 \leq Re \leq 700$ the flow

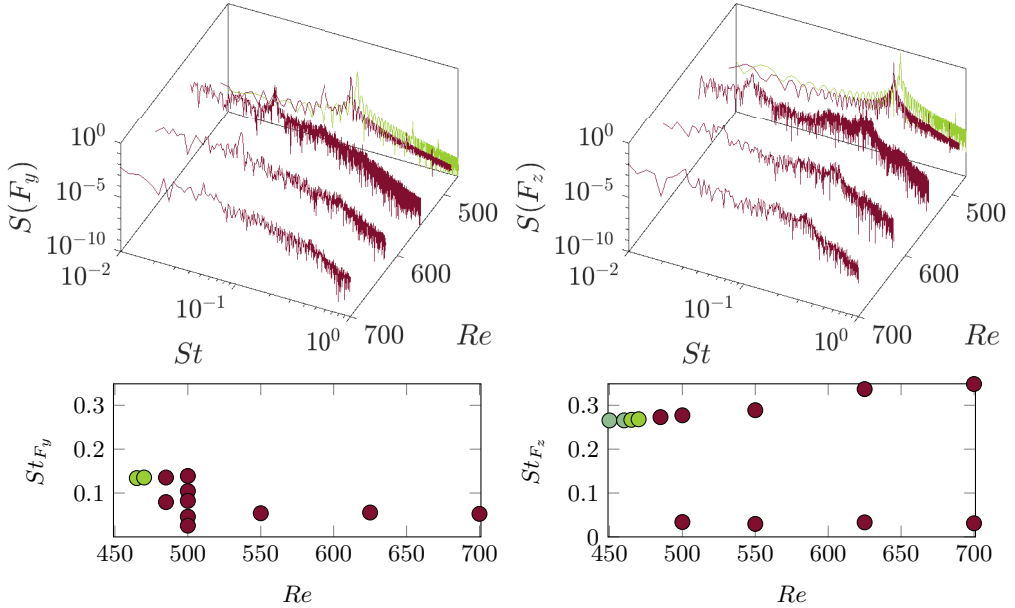


Figure 24: As figure 19, but for $460 \leq Re \leq 700$. In the bottom panel $Re = 450$ is also shown to ease the comparison with the pS_yS_zlb regime described in section 4.2.3.

oscillates around a S_yS_z state, and the time average value of the cross-stream forces is $F_y = F_z = 0$. This recalls the results of Zdravkovich et al. (1989) and Zdravkovich et al. (1998), who investigated the flow past a finite circular cylinder at $Re \approx 10^5$, varying the width-to-height ratio between $0.25 \leq W \leq 10$. In agreement with our results, they found an asymmetric flow pattern for $1 \leq W \leq 2$ only.

According to our simulations, the flow loses the instantaneous left/right symmetry at $Re \approx 465$. For $465 \leq Re \leq 470$ the frequency spectrum of F_y (figure 24) shows a single peak at a frequency of $St \approx 0.134$, which is half the frequency of the LE vortex shedding (see the frequency spectrum of F_z in the same figure). The flow enters a pS_yS_z regime. In this range of Re the flow remains periodic and the attractor is a limit cycle that draws a close line in the phase space; see the $F_y - F_x$ and $F_z - F_x$ diagrams in figure 25. As Re increases, the bifurcated limit cycle becomes unstable, and a new frequency arises; see the spectrum of F_y where at $Re = 485$ a second, non commensurate frequency $St \approx 0.079$ arises. At this Re , the flow is aperiodic and the attractor draws a torus in the phase space.

For $Re \geq 500$, additional frequencies appear and the flow becomes chaotic (see the bottom panels of figure 25). In the aS_yS_z regime the flow dynamics is dominated by the nonlinear interaction of three different modes, i.e. (i) the shedding of hairpin vortices from top and bottom LE shear layers, and the unsteady flapping modes of the wake in the (ii) z and (iii) y directions. The frequency of the first two modes are detected with the peaks in the spectrum of F_z , i.e. $St \approx 0.25-0.30$ and $St \approx 0.02-0.03$. The frequency $St \approx 0.04-0.05$ of the wake flapping mode in the y direction, instead, is visible in the spectrum of F_y . As Re increases, the frequency of the LE vortex shedding increases. However, the

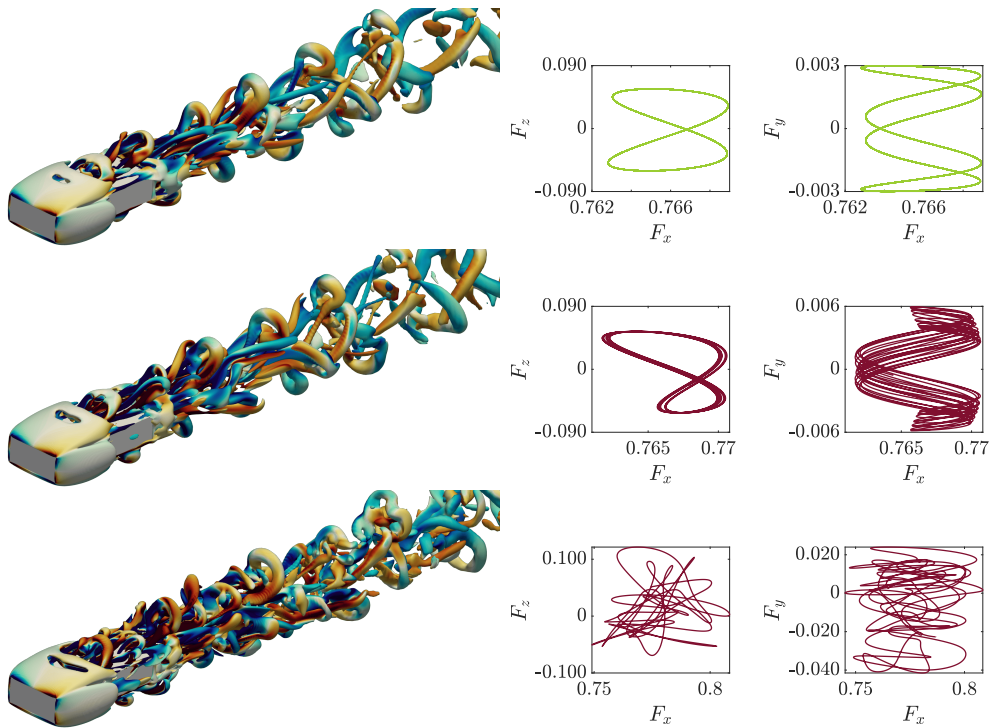


Figure 25: Structure of the flow for $W = 2.25$ and $470 \leq Re \leq 700$. Left: instantaneous visualisation of the flow structure by means of isocontours of $\lambda_2 = -0.05$ coloured with $-1 \leq \omega_x \leq 1$. Right: $F_z - F_x$ and $F_y - F_x$ force diagrams. From top to bottom $Re = 470$, $Re = 485$, $Re = 625$.

corresponding peak in the spectrum of F_z becomes less evident and more broad-banded: for $Re = 700$ it is hardly detectable. Like for smaller W , indeed, when Re increases the LE vortex shedding weakens, and the flow unsteadiness is mainly driven by the wake flapping modes. Note that $St \approx 0.03$ is close to what was found for $W = 1.2$, indicating that the frequency of the wake flapping mode in the z direction is only marginally influenced by the width of the prism for $1.2 \leq W \leq 2.25$. In contrast, the width of the prism clearly influences the frequency of the wake flapping mode in the y direction, as the corresponding St decreases as W increases. Figure 25 shows that for $Re > 500$ the shedding of hairpin vortices arises also over the lateral sides of the prism.

4.3. Wide prism: $W = 5$

For $L = 5$ and $W = 5$ three main regimes have been identified for $Re < 700$ (figure 26). In agreement with the linear stability analysis, at $Re \approx 250$ the low- Re sS_yS_z steady flow experiences a Hopf bifurcation towards the periodic pS_yS_zt regime, which is characterised by the unsteady S_yA_z flapping mode of the wake. For $Re \approx 305$ the flow approaches the aperiodic aS_yS_z regime. Here the wake oscillates in both the y and z directions, and vortices are shed from the top/bottom LE shear layers. The interaction between these modes largely changes with the Reynolds number, and for some Re the flapping mode of the wake in the z direction synchronises with the shedding of vortices from the LE, and the flow recovers periodicity.

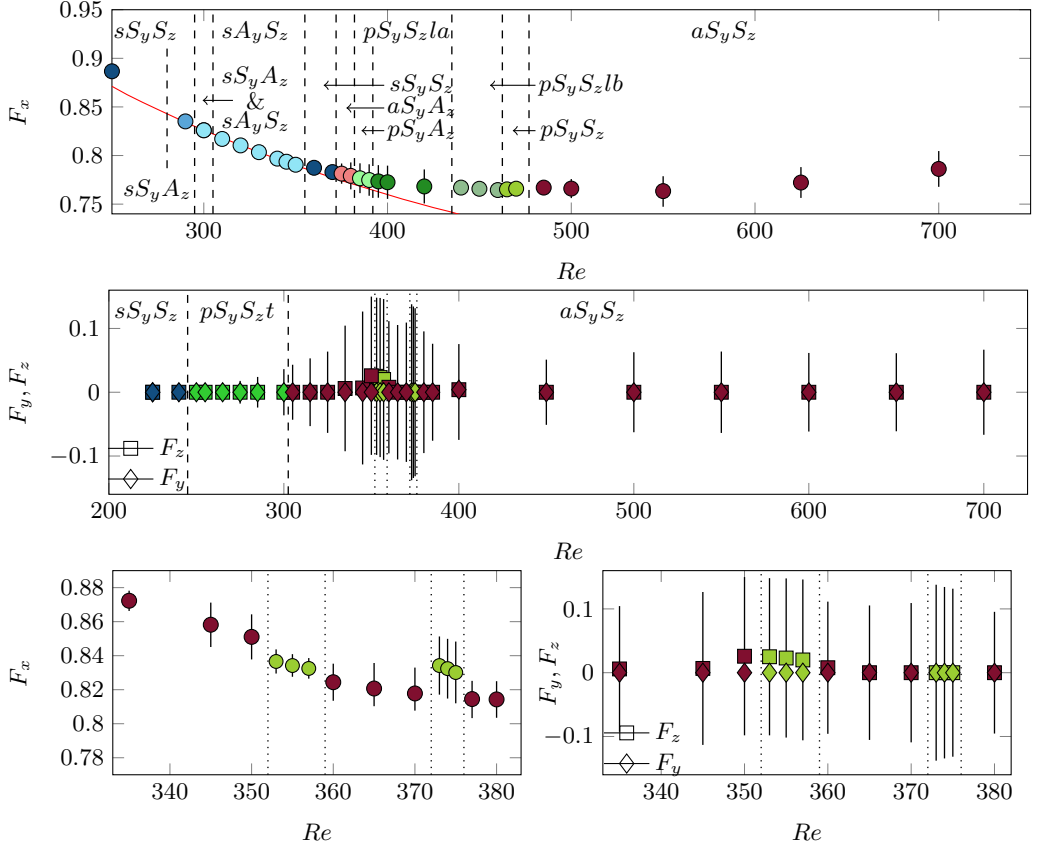


Figure 26: Top panels as figure 10, but for $L = 5$ and $W = 5$. The bottom panels are a zoom in the $330 \leq Re \leq 380$ range.

4.3.1. Low Re : Periodic regime pS_yS_zt

The nonlinear simulations show that the unsteady S_yA_z mode of the wake becomes unstable at $Re \approx 250$, and that for $250 \lesssim Re \lesssim 300$ the flow experiences a periodic flapping of the wake in the z direction around the steady S_yS_z state (see the top panel in figure 27). Unlike in the pS_yS_zl regimes found for smaller W , here hairpin vortices are not shed from the LE shear layers, and the flow unsteadiness is completely driven by the wake flapping. The flow is periodic and shows a single frequency, which is close to the value $St \approx 0.09$ found with the linear stability analysis (see section 3.2). More specifically, the frequency increases slightly with the Reynolds number due to nonlinear effects, being $St \approx 0.085$ at $Re = 250$ and $St \approx 0.09$ for $Re \geq 275$; see figure 27. As expected, the intensity of the wake flapping progressively increases with Re , as conveniently visualised in figure 26 by means of the root mean square: $rms(F_z) \approx 0.004$ at $Re = 250$ and $rms(F_z) \approx 0.036$ at $Re = 300$. In this regime, an increase of Re is accompanied by an increase of F_x , which is entirely ascribed to a monotonous increase of the pressure contribution $F_{x,p}$. In fact, similarly to what was shown for $W = 1.2$ in figure 12, an increase of Re leads to larger side (time-average) recirculating regions and, thus, to a decrease of the friction contribution to F_x (bottom left panel in figure 27).

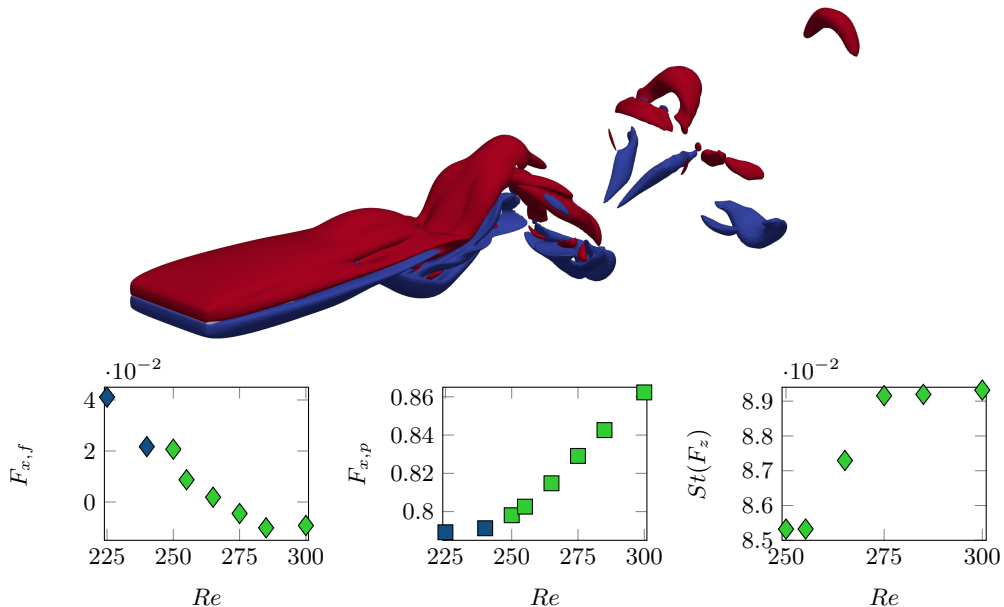


Figure 27: Characterisation of the pS_yS_z regime for $W = 5$. Top: Visualisation of the pS_yS_z regime at $Re = 275$. The red and blue isosurfaces are for $\omega_y = \pm 0.25$. Bottom left panels: friction (left) and pressure (right) contributions to the aerodynamic drag for $225 \leq Re \leq 300$. Bottom right: dependence of the flow frequency on the Reynolds number for $250 \leq Re \leq 300$.

4.3.2. Intermediate Re : aperiodic and frequency-locking regimes

As the Reynolds number increases, the limit cycle loses its stability via a Neimark-Sacker bifurcation, and new frequencies appear in the flow. At $Re \approx 305$ a torus replaces the limit cycle. The unsteady A_yS_z wake mode detected with the linear stability of the low- Re steady sS_yS_z base flow (see section 3.2) becomes unstable, and the flow experiences a flapping motion in both the y and z directions. The new frequency is $St \approx 0.03$, in agreement with the value predicted by the linear stability analysis; see the frequency spectrum of F_y and the $F_y - F_x$ force diagram in figure 28. Note that the Reynolds number corresponding to the onset of the A_yS_z mode is slightly larger than the value $Re_c \approx 280$ predicted by the linear stability of the steady sS_yS_z base flow. As Re increases, the two modes interact nonlinearly and different frequencies arise in the spectra (figure 28), resulting into a progressive loss of coherency. For $Re \gtrsim 325$ a new mode arises with a frequency in the $0.16 \leq St \leq 0.2$ range; see the spectrum of F_z . As shown in the bottom left panel of figure 28 and discussed in the following, this frequency is associated with the shedding of tubes of spanwise vorticity from the top/bottom LE shear layers, that roll up and generate hairpin vortices in the wake, similarly to what was found for smaller W . The shedding frequency for $W = 1.2$ and $W = 2.25$ is larger than that for $W = 5$, indicating that St decreases with W .

The presence of this LE vortex shedding progressively breaks the coherency of the flow (see the force diagrams and the emergence of several peaks in the frequency spectra in figures 28 and 29). However, for two narrow ranges of Reynolds numbers the flow oscillations influence each other in a way that produces synchronisation into a periodic regime. This phenomenon, known as frequency

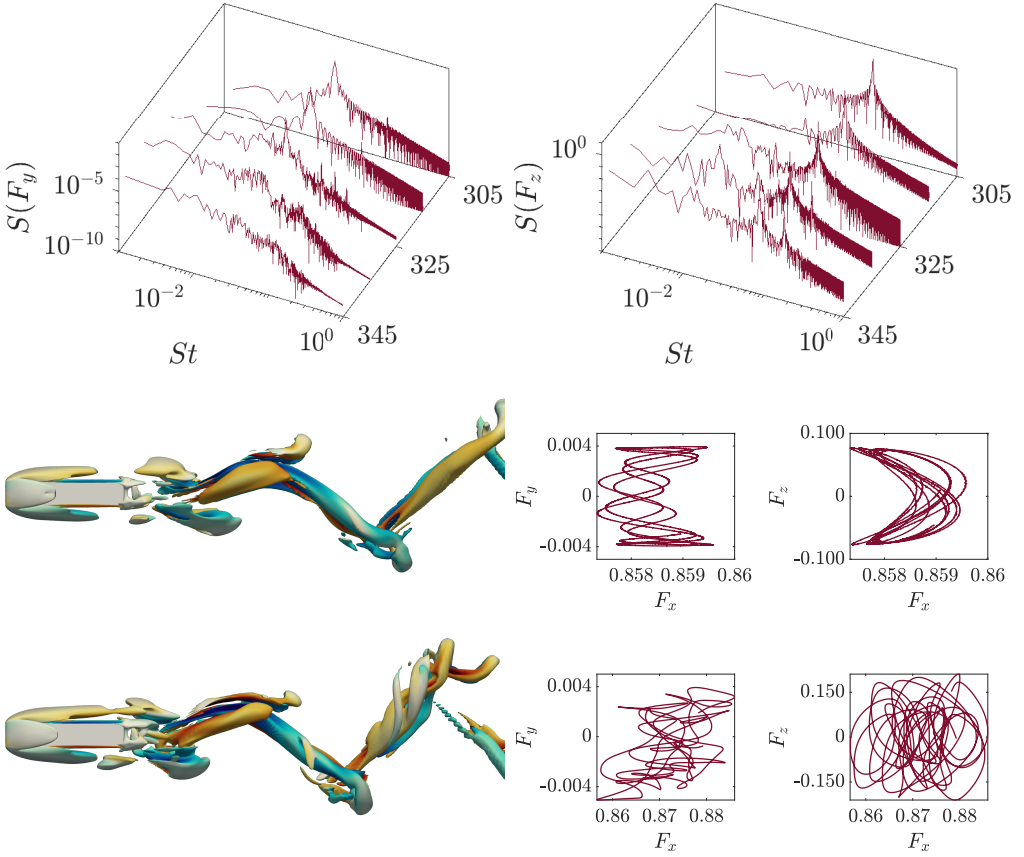


Figure 28: Top: Frequency spectra of the F_y (left) and F_z (right) aerodynamics forces for $W = 5$ and $305 \leq Re \leq 345$. Centre and bottom: Structure of the flow for $W = 5$ and $Re = 315$ (top) and $Re = 335$ (bottom); left: instantaneous visualisation of the flow structure by means of isocontours of $\lambda_2 = -0.25$ coloured with $-1 \leq \omega_x \leq 1$; right: $F_y - F_x$ and $F_z - F_x$ force diagrams.

locking (Iooss & Joseph 1990; Kuznetsov 2004), has already been observed in the flow past 2D rectangular cylinders by Chiarini et al. (2022c) who investigated the interaction of the LE and TE vortices at intermediate Re . They found that the two sheddings synchronise and different stable cycles (periodic orbits) arise in the torus, with a long-time period $T_{lp} = pT_{TE} = qT_{LE}$, where T_{LE} and T_{TE} are the characteristic times of the vortex shedding from the LE and the TE. In the present case, the frequency locking is visualised in figure 29, where the focus is on the range $345 \leq Re \leq 385$. The main frequency of the vertical wake flapping, $St \approx 0.09$, varies only marginally with Re (squares in the central panel of figure 29). We have found the same shedding frequency in the turbulent regime at $Re = 3000$ (not shown). By contrast, the main frequency of the LE vortex shedding increases with the Reynolds number: $St \approx 0.18$ at $Re = 345$ and $St \approx 0.20$ at $Re = 380$ (circles in the central panel of figure 29). The characteristic frequency of the LE vortex shedding is approximately twice that of the vertical wake flapping for all Re , meaning that two LE vortices are shed from the top and bottom LE shear layers during approximately one wake flapping period. The

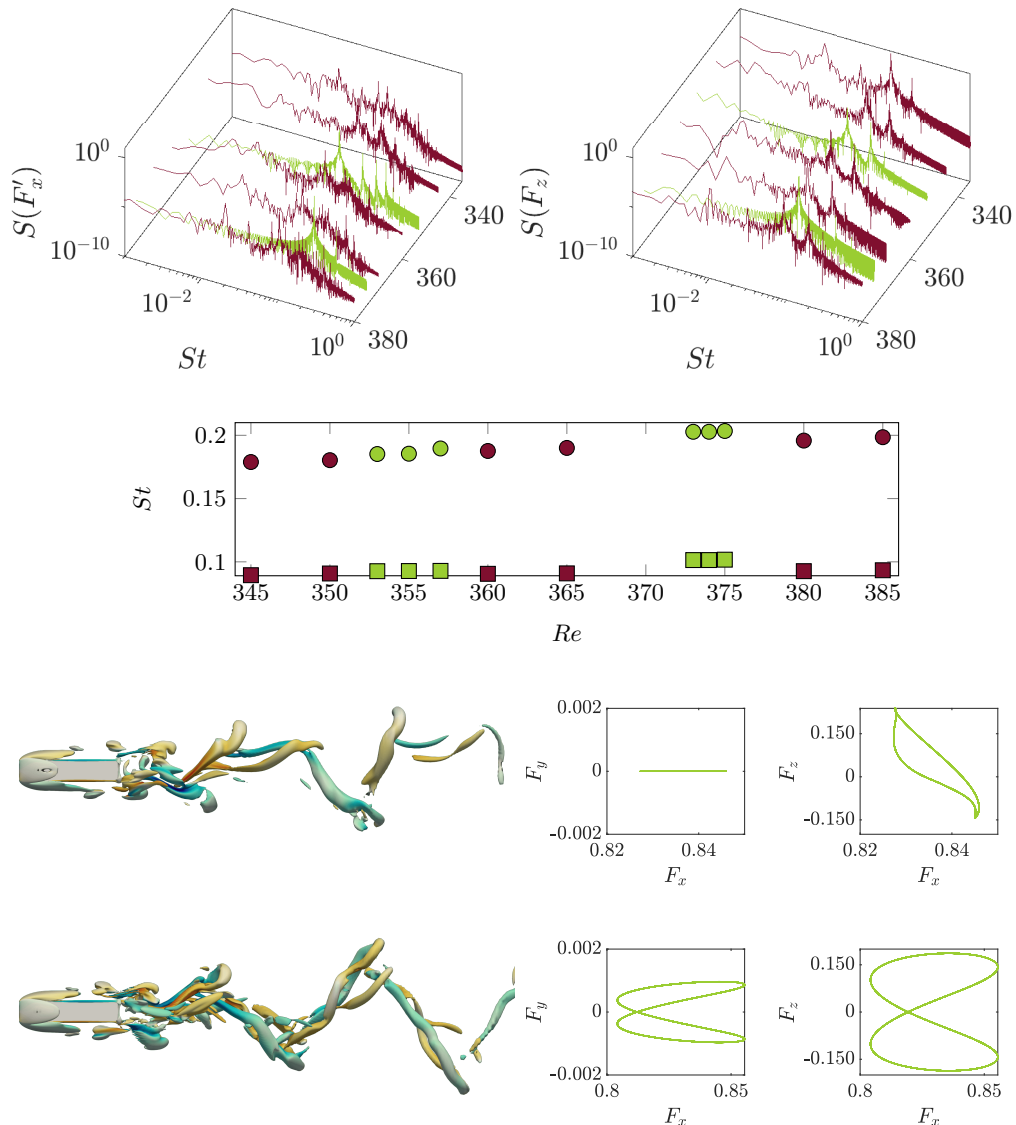


Figure 29: As figure 28, but for $345 \leq Re \leq 380$. The top left panel is for the frequency spectrum of the fluctuations of F_x . The central panel shows the dependence of the main flow frequencies on the Reynolds number for $345 \leq Re \leq 385$. The bottom panels are for $Re = 353$ (top) and $Re = 375$ (bottom).

flow recovers periodicity for $353 \leq Re \leq 357$ and $373 \leq Re \leq 375$: the LE vortex shedding synchronises with the vertical wake flapping, and a limit cycle arises with $T_p = T_{TE} = 2T_{LE}$ (i.e. $p = 1$ and $q = 2$).

Interestingly, the relative phase between the top and bottom vortex shedding is different in the two synchronised regimes: in phase opposition for $353 \leq Re \leq 357$, and in phase for $373 \leq Re \leq 375$ (figure 29). This explains why the $St = 1/T_{LE}$ frequency is not visible in the spectrum of F_z for $373 \leq Re \leq 375$: since

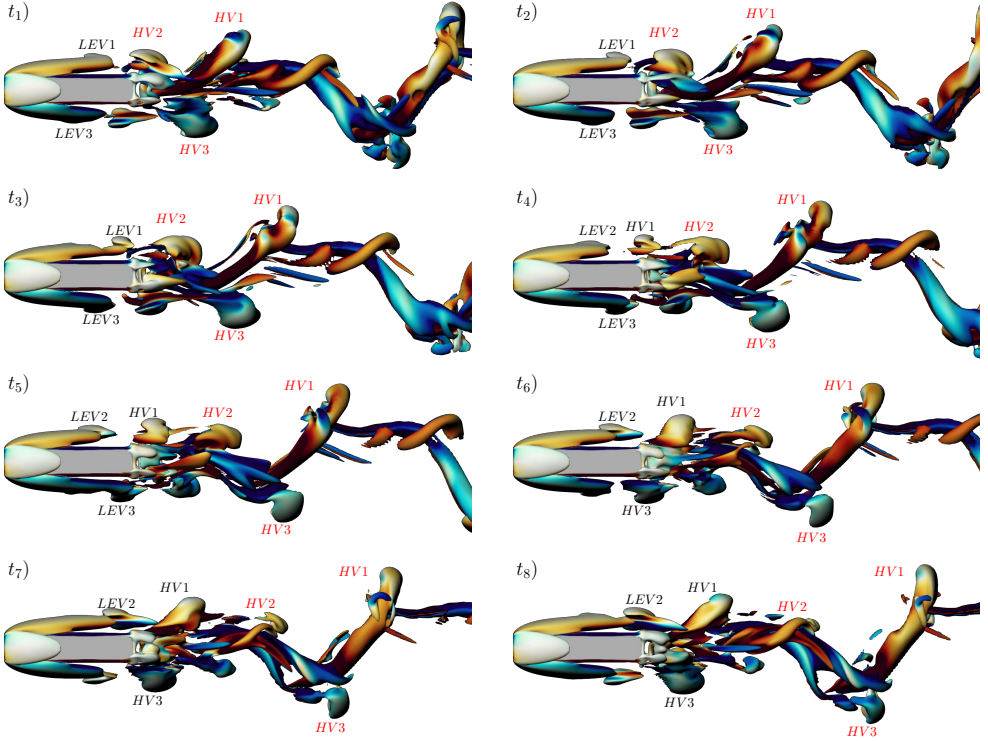


Figure 30: Lateral view of the flow structures within one period of the wake vortex shedding for $L = 5$ and $W = 5$ at $Re = 353$. Eight snapshots are shown separated in time by $T/8$, where T is the period of the wake flapping.

Isosurfaces of $\lambda_2 = -0.05$ coloured with the streamwise vorticity. The blue-to-red colourmap is for $-1 \leq \omega_x \leq 1$. Black labels refer to vortices shed in the considered period. Red labels refer to vortices shed in the previous period.

the top and bottom LE vortices are shed in phase, they do not create any instantaneous unbalance of vertical force. By contrast, for $353 \leq Re \leq 357$ the closed trajectory in the $F_z - F_x$ force diagram is not symmetric with respect to $F_z = 0$, meaning that the time-averaged F_z is non-zero. More generally, the time-averaged top/bottom symmetry is lost for $345 \leq Re \leq 360$ (figure 26). Regarding the lateral aerodynamic force, the different phase locking in the two synchronised regimes results in a different behaviour: $F_y \approx 0$ at all times for $353 \leq Re \leq 357$, while F_y oscillates with $St = 1/T_{TE} = 1/(2T_{LE})$ for $373 \leq Re \leq 375$.

We now illustrate the interaction between the LE and TE vortex shedding in the $353 \leq Re \leq 357$ range. Figure 30 shows eight snapshots of the flow at $Re = 353$, taken equispaced within a single period T_{TE} . Black labels refer to vortices that are shed within the considered period and red labels to vortices shed in the previous period. The vortices shed from the top and bottom LE shear layers are in phase opposition. At $t = t_1$ a spanwise-aligned vortex, named LEV1, is generated from the top LE shear layer, and convected downstream (see $t = t_2$). At $t = t_3$, LEV1 crosses the TE corner in phase with the upwards motion of the wake, and rolls up (t_4 , t_5 and t_6), generating a large hairpin vortex (HV1) that is then shed downstream (t_7 and t_8). The same dynamics is observed over the bottom side. A spanwise-aligned vortex LEV3 (of opposite vorticity compared to

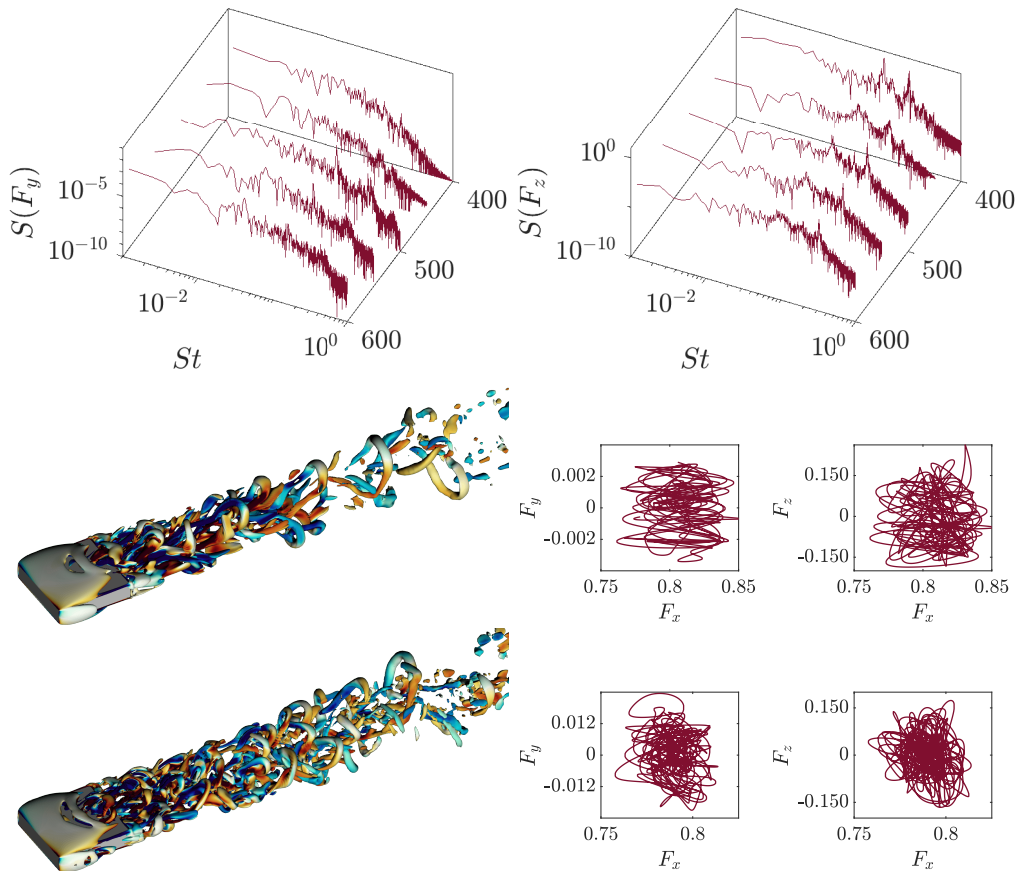


Figure 31: Top: frequency spectra of the F_y (left) and F_z (right) aerodynamics forces for $W = 5$ and $400 \leq Re \leq 600$. Centre and bottom: Structure of the flow for $Re = 400$ (centre) and $Re = 500$ (bottom). The left panel are isosurfaces of $\lambda_2 = -0.05$ coloured with the streamwise vorticity. The right panels are the $F_y - F_x$ and $F_z - F_x$ force diagrams.

LEV1) is shed from the LE shear layer at $t = t_3$. It crosses the bottom TE at $t = t_5$, and rolls up generating a hairpin vortex HV3 at $t = t_6$. Moving again to the top side, at $t = t_5$ the second spanwise-aligned vortex LEV2 is shed from the top LE shear layer. It crosses the TE corner at $t = t_5$ in phase with the downwards motion of the wake, and generates a streamwise-aligned rib-like structure that is then connected with the HV3 hairpin vortex.

In the $373 \leq Re \leq 375$ range, LE vortices interact with the vertical flapping of the wake in the same way, and a top (bottom) hairpin vortex arises when a LE vortex crosses the top (bottom) TE in phase with an upward (downward) motion of the wake.

4.3.3. Large Re : Aperiodic regime

For $Re \geq 400$ the synchronisation between the LE and TE vortex shedding is not observed any more, and the flow becomes progressively more chaotic. Like for lower Reynolds numbers, the frequency of the wake flapping is still approximately constant with Re , while the frequency of the LE vortex shedding

keeps increasing. To be quantitative, for $Re = 400, 500$ and 600 we measure $(St_{TE}, St_{LE}) \approx (0.095, 0.205), (0.094, 0.280)$ and $(0.100, 0.320)$, respectively. The increase in Re is accompanied by a slight increase in the amplitude of the oscillations in the y direction, as visualised in figure 26 by means of the rms of the aerodynamic forces. For $Re \geq 500$, a third peak appears in the spectrum of F_y at $St \approx 0.125$, and a shedding of hairpin vortices occurs also along the lateral sides of the prism (figure 31).

5. Conclusion

In this study we have investigated the sequence of bifurcations of the laminar flow past three-dimensional rectangular prisms. The length-to-height and width-to-height ratios are varied between $1 \leq L \leq 5$ and $1.2 \leq W \leq 5$, and the Reynolds number is increased up to $Re \approx 700$. The study is based on linear stability analysis for the characterisation of the primary bifurcation. For $L = 5$ we have used weakly nonlinear analysis for the study of the nonlinear interactions between competing modes close to the bifurcation points, and direct numerical simulations to fully account for the nonlinear effects and describe the bifurcation scenario at larger Re .

The linear stability analysis shows that the nature of the primary bifurcation changes depending on W and L . The flow past wide prisms with large W/L experiences first a Hopf bifurcation and becomes unstable to oscillatory perturbations that break the top/bottom planar symmetry, leading to a periodic vortex shedding across the smaller dimension of the body. For smaller W/L , the primary instability consists of a pitchfork bifurcation. For intermediate W/L , the flow becomes first unstable to stationary perturbations that break the top/bottom planar symmetry, while preserving the left/right one. This leads to a static vertical deflection of the wake. On the contrary, for small W/L the flow becomes first unstable to steady perturbations that break the left/right planar symmetry, and lead to a static horizontal deflection of the wake. In all cases, the critical Reynolds number corresponding to the first onset of the primary instability increases with L , and has a non-monotonous dependence on W .

A weakly nonlinear analysis has been performed for $(L, W) = (5, 1.2)$ and $(L, W) = (5, 2.25)$ in the vicinity of the critical Re of the static modes that break the top/bottom and left/right symmetries. Two coupled amplitude equations are obtained, revealing the sequence of bifurcations close to the bifurcation points. For $W = 1.2$ we have derived the third-order amplitude equations and the bifurcation scenario resembles what was found by Zampogna & Boujo (2023) for Ahmed bodies, with a change of stability between the vertically deflected state and the horizontally deflected one at $Re \approx 353$. For $W = 2.25$ we have derived the fifth-order amplitude equations and find a subcritical bifurcation for the horizontally deflected state, with a relatively narrow interval of bistability between the vertically (lower Re) and horizontally (larger Re) deflected states. The fully nonlinear simulations confirm the bifurcation sequence predicted by the linear and weakly nonlinear stability analyses, including the bistability-induced hysteresis for $W = 2.25$ and the final states after the first bifurcations.

At larger Re the non linear simulations reveal an extremely rich bifurcation scenario (see figure 32), that has been investigated by means of frequency spectra and force diagrams, and with the aid of the proper orthogonal decomposition (POD) to separate the modes. For Reynolds numbers up to $Re \approx 700$ the flow

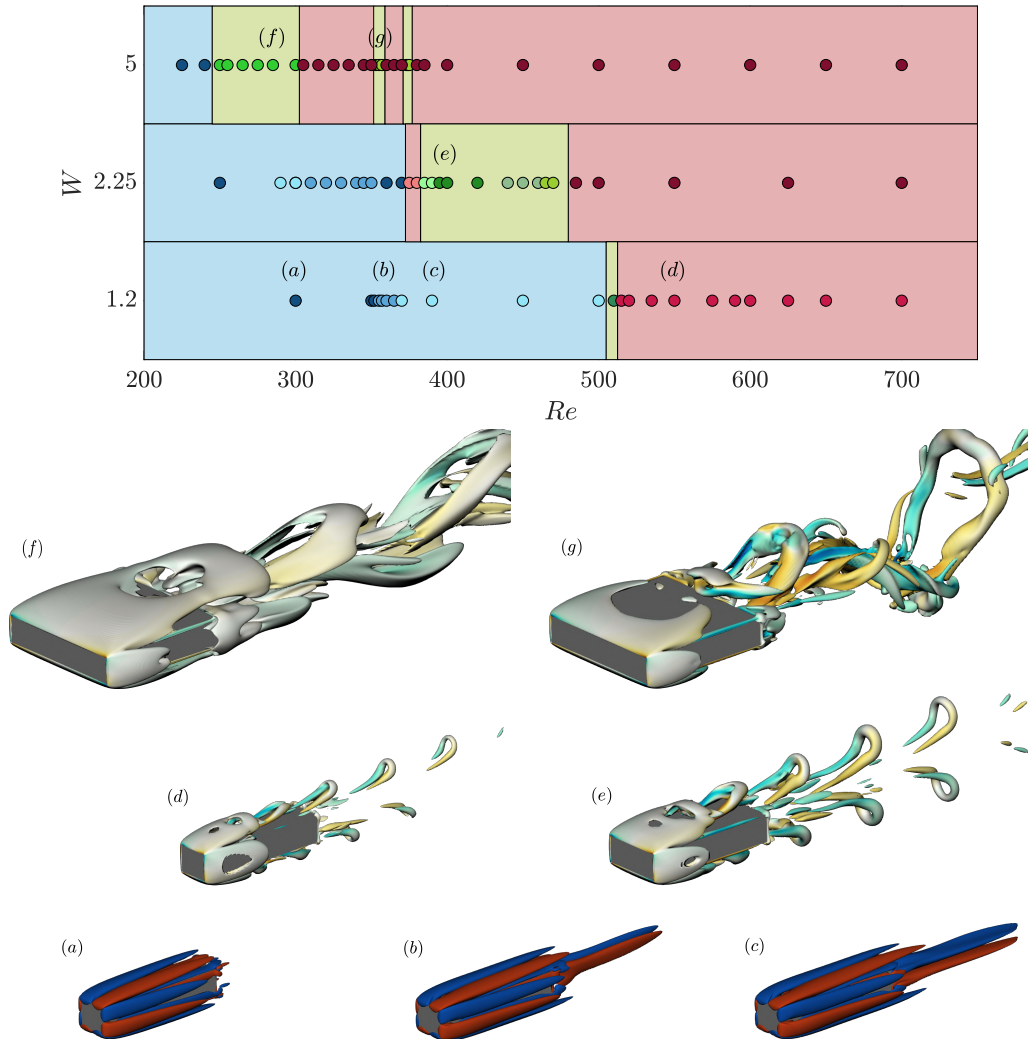


Figure 32: Regimes observed in the flow past rectangular prisms with $L = 5$ for Reynolds numbers up to $Re = 700$. Blue, green and red shaded areas refer to steady, periodic and aperiodic states, respectively. Different tonalities refer to different regimes, accordingly to figures 10, 17 and 26. The solid lines separating the regimes are a guide to the eye. Vertical axis not to scale. (a)-(c) Steady flows are represented with $\omega_x = \pm 0.1$ isosurfaces, and (d)-(g) unsteady flows with snapshots of λ_2 isosurfaces coloured with the streamwise vorticity.

dynamics is driven by the non linear interaction of five different modes, i.e. the static deflections of the wake in the (i) vertical and (ii) horizontal directions, (iii) a vortex shedding of hairpin vortices from the LE shear layers, and the unsteady flapping modes of the wake in the (iv) vertical and (v) horizontal directions. Their nonlinear interaction changes with W and Re giving rise to several regimes, ranging from steady and periodic regimes at small Re to aperiodic and chaotic regimes at larger Re . For intermediate W we have observed, for the first time, a periodic LE shedding of hairpin vortices that instantaneously preserves all

spatial symmetries and generates neither lift nor side forces. Interestingly, in some portions of the parameter space the different modes synchronise, and give origin to periodic regimes also at relatively large Re .

The mechanism sustaining the shedding of the hairpin vortices from the LE shear layers has been investigated. Unlike in the flow past two-dimensional rectangular cylinders, this LE vortex shedding does not require the presence of a sharp trailing edge, and does not necessarily lock with the TE vortex shedding. Indeed, for $W = 2.25$ the same vortex shedding has been found for a three-dimensional rectangular flat plate without trailing edge ($L = \infty$). By rounding the LE corners, we have also shown that the LE vortex shedding is the result of a feedback mechanism embedded within the recirculating regions that form over the lateral sides of the prisms.

Having characterised the flow stability and dynamics in a systematic manner over a wide range of body widths and lengths, the present study will serve as a stepping stone to further investigation in more complex settings. For instance, the laminar wakes of spheres and 2D cylinders translating close to a solid wall have been studied extensively (Thompson *et al.* 2021). Ground proximity is by definition an essential feature of flows around ground vehicles such as cars and trains, and many numerical simulations have been carried out. The stability of these flows, however, still remains largely unexplored in both the laminar and turbulent regimes, except for a few studies (e.g. simplified train geometry with $L/H = 6.9$, $W/H = 0.83$ and ground clearance $0.15H$ in Li *et al.* 2024). Another topic of interest is that of body attitude (yaw and pitch), as in the laminar regime a small misalignment may significantly alter the onset and sequence of bifurcations, and in the turbulent regime ground vehicles may be subject to crosswind or varying front/rear load distribution. Finally, the effect of stochastic conditions (e.g. disturbances in the incoming flow) on the laminar bifurcations and wake dynamics could be studied, especially near codimension-two bifurcations where two stationary modes become unstable simultaneously (e.g. $(L, W) = (3, 1.2)$ at $Re \approx 330$, $(5, 1.2)$ at $Re \approx 350$, or $(5, 2.25)$ at $Re \approx 300$), which may result in multistability, with the wake switching randomly between two or more static deflected states. A treatment in the spirit of Ducimetière *et al.* (2024) would yield a rigorously derived reduced-order model in the form of coupled stochastic amplitude equations, one for each symmetry-breaking mode, which could then be used to predict flow statistics.

Acknowledgments

A.C. acknowledges the computer time provided by the Scientific Computing & Data Analysis section of the Core Facilities at OIST.

Funding

This research received no specific grant from any funding agency, commercial or not-for-profit sectors.

Declaration of Interests

The authors report no conflict of interest.

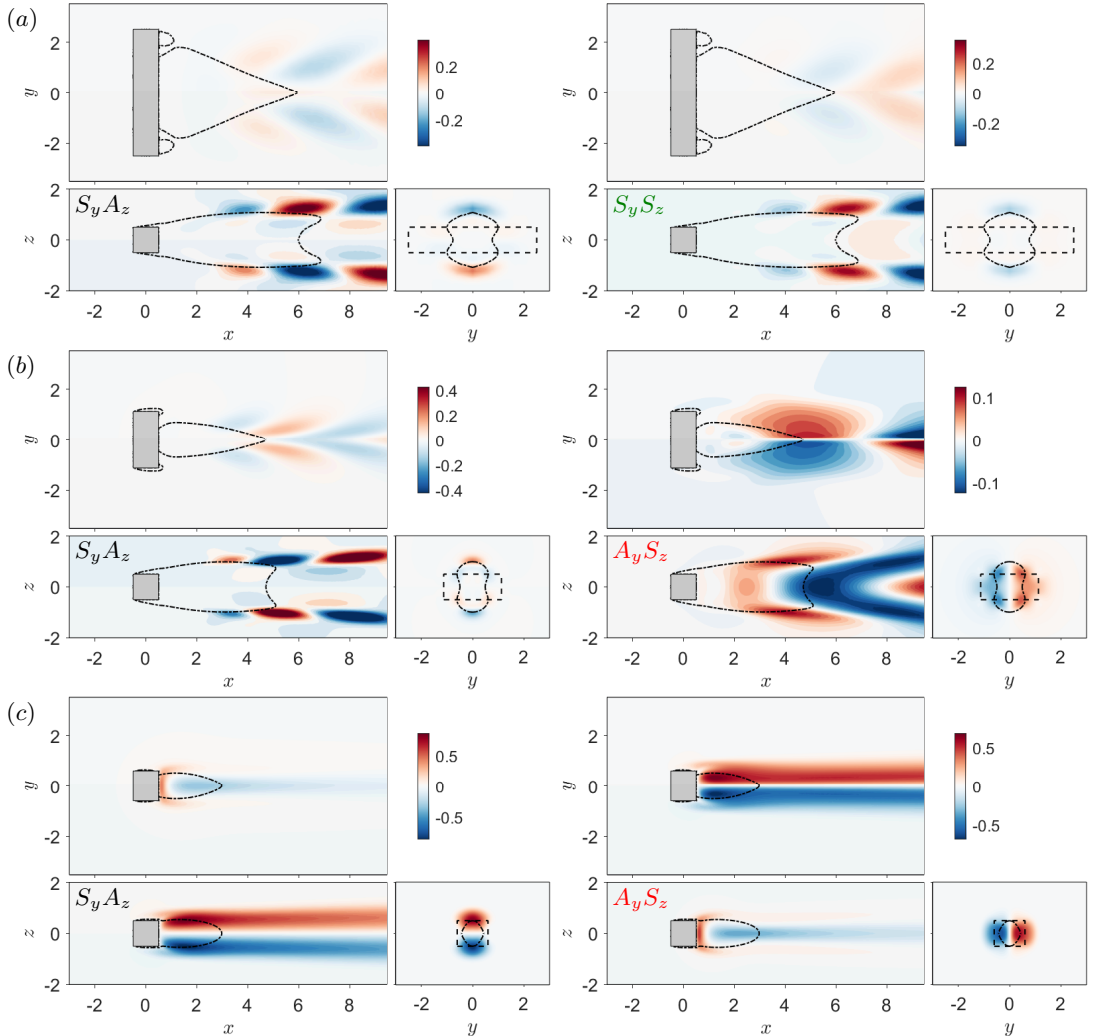


Figure 33: Eigenmodes $\hat{\mathbf{u}}_1$ (real part), $L = 1$. Top view ($z = 0$), side view ($y = 0$) and rear view ($x = x^*$). Dash-dotted line: contour of zero streamwise velocity, $u_0 = 0$. (a) $W = 5$, $Re = 120$, $x^* = 4$; (b) $W = 2.25$, $Re = 200$, $x^* = 3$; (c) $W = 1.2$, $Re = 180$, $x^* = 2$.

Appendix A. Eigenmodes and structural sensitivity

Three-dimensional views of the two leading eigenmodes and their structural sensitivity were shown in figures 6 and 8 for six different geometries ($W = 1, 2.25$ and 5 , and $L = 1$ and 5). In this appendix, we provide two-dimensional cross-sections of these eigenmodes and their structural sensitivity in the near-wake region, in figures 33-36.

Appendix B. Convergence study

Tables 1 and 2 show how the critical Reynolds numbers of the first two bifurcations vary with the mesh size and domain size. The numerical domain is

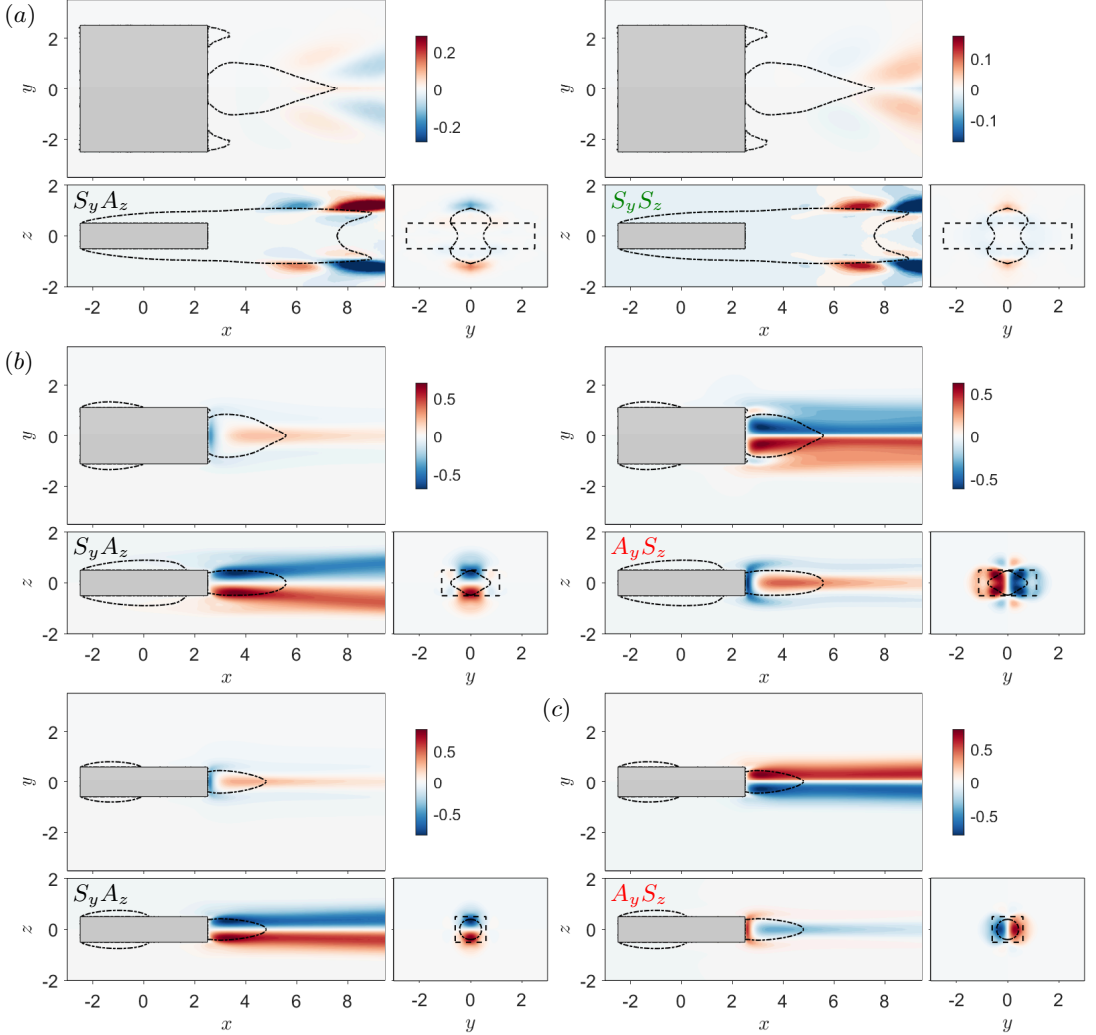


Figure 34: Same as figure 33, $L = 5$. (a) $W = 5$, $Re = 260$, $x^* = 6$; (b) $W = 2.25$, $Re = 300$, $x^* = 4$; (c) $W = 1.2$, $Re = 360$, $x^* = 3.5$.

$\{x, y, z \mid x_{min} \leq x \leq x_{max}; 0 \leq y, z \leq y_{max} = z_{max}\}$. The mesh density is n_1 on the prism surface, n_2 on the boundaries of the sub-domain $\{x, y, z \mid -5 \leq x \leq 15; 0 \leq y, z \leq 2\}$, and $n_3 = 1$ on the outermost boundaries. Given the weak influence of the mesh size and domain size on $Re_{c,1}$ and $Re_{c,2}$, we choose mesh $M3$ and domain $D1$ throughout the linear and weakly nonlinear analyses, similar to Zampogna & Boujo (2023).

Appendix C. Weakly nonlinear analysis

We detail here the derivation of the systems of third- and fifth-order amplitude equations (3.1)-(3.2) and (3.3)-(3.4) in the vicinity of a codimension-two bifurcation for two stationary modes A and B . The procedure is similar to that in Zampogna & Boujo (2023).

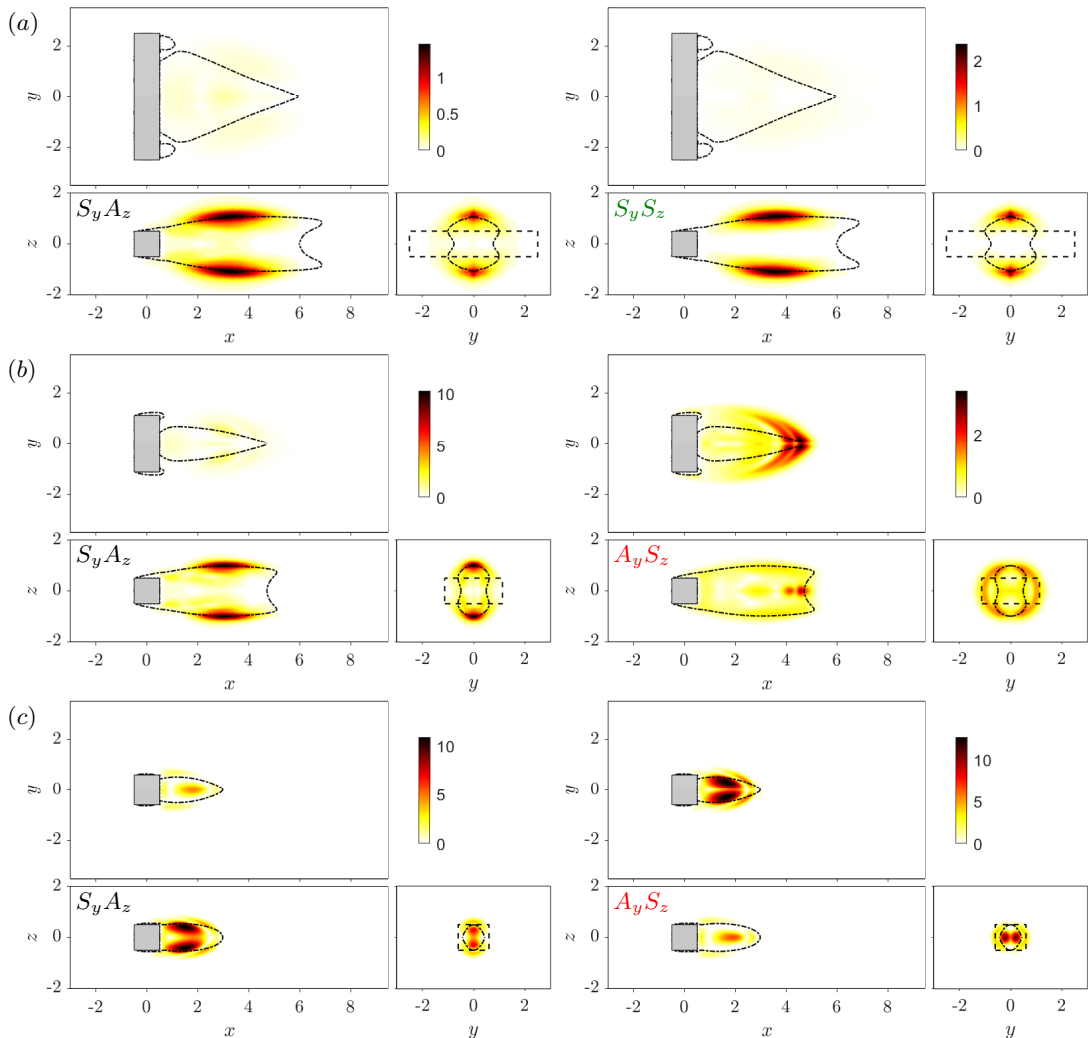


Figure 35: Structural sensitivity, $L = 1$. Top view ($z = 0$), side view ($y = 0$) and rear view ($x = x^*$). Dash-dotted line: contour of zero streamwise velocity, $u_0 = 0$. (a) $W = 5$, $Re = 120$, $x^* = 4$; (b) $W = 2.25$, $Re = 200$, $x^* = 3$; (c) $W = 1.2$, $Re = 180$, $x^* = 2$.

C.1. Derivation of the amplitude equations

When the two modes of interest do not bifurcate exactly at the same Reynolds number, we introduce a reference critical Reynolds number Re_c , typically chosen between the critical Reynolds numbers of the two modes. Departure from criticality is measured as

$$\frac{1}{Re_c} - \frac{1}{Re} = \epsilon^2 \tilde{\alpha}, \quad (\text{C1})$$

which defines the small parameter $0 < \epsilon \ll 1$ and the order-one parameter $\tilde{\alpha} = O(1)$. We also define a shift operator \mathcal{S} such that, unlike the original linearised NS operator \mathcal{A} , the shifted linearised NS operator $\tilde{\mathcal{A}} = \mathcal{A} + \epsilon^2 \mathcal{S}$ is singular

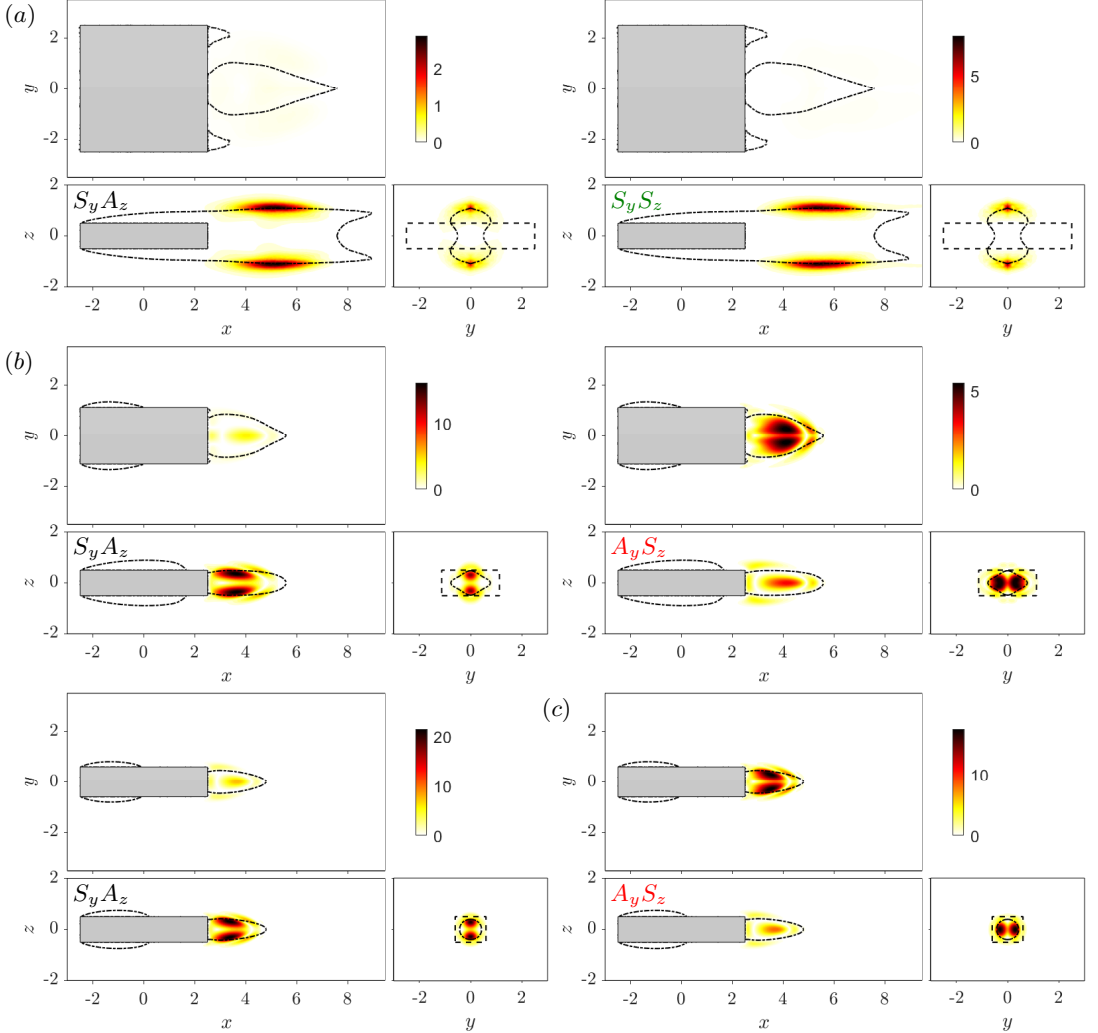


Figure 36: Same as figure 35, $L = 5$. (a) $W = 5$, $Re = 260$, $x^* = 6$; (b) $W = 2.25$, $Re = 300$, $x^* = 4$; (c) $W = 1.2$, $Re = 360$, $x^* = 3.5$.

exactly at $Re = Re_c$ for both modes. In other words, denoting $\mathcal{B}\partial_t \mathbf{q} + \mathcal{A}\mathbf{q} = \mathbf{0}$ the linearised NS equations and $\hat{\mathbf{q}} = \{\hat{\mathbf{u}}, \hat{p}\}$, one has $\tilde{\mathcal{A}}\hat{\mathbf{q}}_1^A = \tilde{\mathcal{A}}\hat{\mathbf{q}}_1^B = \mathbf{0}$, while $\mathcal{A}\hat{\mathbf{q}}_1^A = -\sigma_A \mathcal{B}\hat{\mathbf{q}}_1^A$ and $\mathcal{A}\hat{\mathbf{q}}_1^B = -\sigma_B \mathcal{B}\hat{\mathbf{q}}_1^B$.

We use the method of multiple scales. We introduce slow time scales $T_1 = \epsilon^2 t$, $T_2 = \epsilon^4 t, \dots$ and inject the expansion

$$\mathbf{q}(\mathbf{x}, t, T_1, T_2 \dots) = \mathbf{q}_0 + \epsilon \mathbf{q}_1 + \epsilon^2 \mathbf{q}_2 + \epsilon^3 \mathbf{q}_3 + \dots \quad (\text{C } 2)$$

in the NS equations at $Re = Re_c$, where the time derivative now reads $\partial_t + \epsilon^2 \partial_{T_1} + \epsilon^4 \partial_{T_2} + \dots$. Collecting like-order terms yields the following series of problems.

C.1.1. Zeroth and first orders

At order ϵ^0 we find the nonlinear NS equations, and the zeroth-order field $\mathbf{q}_0(\mathbf{x})$ is the steady $S_y S_z$ base flow at $Re = Re_c$. At order ϵ^1 we obtain the linearised

	Mesh	M1	M2	M3	M4	M5	M6	M7
	n_1	30	40	60	60	60	80	80
	n_2	10	10	10	12	15	10	12
$W = 1.2, L = 1/6$	$N_{elmts} (\times 10^6)$	0.76	0.83	0.97	1.46	2.49	-	-
	$Re_{c,1}(S_y A_z)$	109	109	108	108	108	-	-
	$Re_{c,2}(A_y S_z)$	113	113	113	113	113	-	-
$W = 1.2, L = 5$	$N_{elmts} (\times 10^6)$	0.92	1.14	1.63	2.23	-	2.27	3.04
	$Re_{c,1}(S_y A_z)$	357	354	352	352	-	352	352
	$Re_{c,2}(A_y S_z)$	354	354	353	353	-	353	353
$W = 5, L = 1/6$	$N_{elmts} (\times 10^6)$	0.76	0.82	0.95	1.43	2.46	-	-
	$Re_{c,1}(S_y A_z)$	61	60	60	60	60	-	-
	$Re_{c,2}(S_y S_z)$	80	79	79	79	79	-	-
$W = 5, L = 5$	$N_{elmts} (\times 10^6)$	0.78	0.86	1.04	1.55	2.61	1.26	1.83
	$Re_{c,1}(S_y A_z)$	233	234	235	235	235	235	236
	$Re_{c,2}(S_y S_z)$	259	259	263	264	264	263	265

Table 1: Influence of the mesh size on the first two critical Reynolds numbers for four different prism geometries. Domain D1: $x_{min} = -10$, $x_{max} = 20$, $y_{max} = z_{max} = 10$.

	Domain	D1	D2	D3
	x_{min}	-10	-15	-20
	x_{max}	20	30	40
	y_{max}, z_{max}	10	15	20
$W = 1.2, L = 1/6$	$N_{elmts} (\times 10^6)$	0.97	1.16	1.49
	$Re_{c,1}(S_y A_z)$	108	109	109
	$Re_{c,2}(A_y S_z)$	113	113	113
$W = 1.2, L = 5$	$N_{elmts} (\times 10^6)$	1.63	1.81	2.14
	$Re_{c,1}(S_y A_z)$	352	354	354
	$Re_{c,2}(A_y S_z)$	353	354	354
$W = 5, L = 1/6$	$N_{elmts} (\times 10^6)$	0.95	1.14	1.46
	$Re_{c,1}(S_y A_z)$	60	61	61
	$Re_{c,2}(S_y S_z)$	79	79	80
$W = 5, L = 5$	$N_{elmts} (\times 10^6)$	1.04	2.06	2.06
	$Re_{c,1}(S_y A_z)$	235	236	236
	$Re_{c,2}(S_y S_z)$	263	262	263

Table 2: Influence of the domain size on the first two critical Reynolds numbers for four different prism geometries. Mesh M3: $n_1 = 60$, $n_2 = 10$.

and shifted NS equations

$$\partial_t \mathbf{q}_1 + \tilde{\mathcal{A}} \mathbf{q}_1 = 0. \quad (\text{C3})$$

Since $\tilde{\mathcal{A}}$ is singular at $Re = Re_c$, the first-order field is a superposition of the $S_y A_z$ and $A_y S_z$ eigenmodes:

$$\mathbf{q}_1(\mathbf{x}, T_1, T_2, \dots) = A\hat{\mathbf{q}}_1^A + B\hat{\mathbf{q}}_1^B, \quad (\text{C } 4)$$

where $A(T_1, T_2, \dots)$ and $B(T_1, T_2, \dots)$ are real-valued slowly-varying amplitudes to be determined.

C.1.2. Second order

At order ϵ^2 the field \mathbf{q}_2 is a solution of the linearised and shifted NS equations

$$\mathcal{B}\partial_t \mathbf{q}_2 + \tilde{\mathcal{A}}\mathbf{q}_2 = \{\mathbf{F}_2, 0\}, \quad (\text{C } 5)$$

where

$$\begin{aligned} \mathbf{F}_2 &= -\tilde{\alpha}\nabla^2 \mathbf{u}_0 - (\mathbf{u}_1 \cdot \nabla) \mathbf{u}_1 \\ &= -\tilde{\alpha}\nabla^2 \mathbf{u}_0 - A^2 \hat{\mathbf{u}}_1^A \cdot \nabla \hat{\mathbf{u}}_1^A - ABC(\hat{\mathbf{u}}_1^A, \hat{\mathbf{u}}_1^B) - B^2 \hat{\mathbf{u}}_1^B \cdot \nabla \hat{\mathbf{u}}_1^B, \end{aligned} \quad (\text{C } 6)$$

and where we have introduced the notation $\mathcal{C}(\mathbf{a}, \mathbf{b}) = (\mathbf{a} \cdot \nabla) \mathbf{b} + (\mathbf{b} \cdot \nabla) \mathbf{a}$. Symmetry considerations show that (C 5) can be inverted: all the terms in \mathbf{F}_2 are either $S_y S_z$ or $A_y A_z$ and cannot resonate since $\tilde{\mathcal{A}}$ is singular to $S_y A_z$ and $A_y S_z$ modes. Therefore,

$$\mathbf{q}_2(\mathbf{x}, T_1, T_2, \dots) = \tilde{\alpha}\mathbf{q}_2^\alpha + A^2 \mathbf{q}_2^{A^2} + B^2 \mathbf{q}_2^{B^2} + AB\mathbf{q}_2^{AB}, \quad (\text{C } 7)$$

where the \mathbf{q}_2^* fields are solution of:

$$\begin{aligned} \tilde{\mathcal{A}}\mathbf{q}_2^\alpha &= -\{\nabla^2 \mathbf{u}_0, 0\}, & \tilde{\mathcal{A}}\mathbf{q}_2^{A^2} &= -\{(\hat{\mathbf{u}}_1^A \cdot \nabla) \hat{\mathbf{u}}_1^A, 0\}, \\ \tilde{\mathcal{A}}\mathbf{q}_2^{B^2} &= -\{(\hat{\mathbf{u}}_1^B \cdot \nabla) \hat{\mathbf{u}}_1^B, 0\}, & \tilde{\mathcal{A}}\mathbf{q}_2^{AB} &= -\{\mathcal{C}(\hat{\mathbf{u}}_1^A, \hat{\mathbf{u}}_1^B), 0\}. \end{aligned} \quad (\text{C } 8)$$

C.1.3. Third order

At order ϵ^3 the field \mathbf{q}_3 is a solution of the linearised and shifted NS equations

$$\mathcal{B}\partial_t \mathbf{q}_3 + \tilde{\mathcal{A}}\mathbf{q}_3 = \{\mathbf{F}_3, 0\}, \quad (\text{C } 9)$$

where

$$\begin{aligned} \mathbf{F}_3 &= -(\partial_{T_1} A) \hat{\mathbf{u}}_1^A - (\partial_{T_1} B) \hat{\mathbf{u}}_1^B + A(\tilde{\sigma}_A \hat{\mathbf{u}}_1^A - \tilde{\alpha}\mathcal{C}(\hat{\mathbf{u}}_1^A, \mathbf{u}_2^\alpha) - \tilde{\alpha}\nabla^2 \hat{\mathbf{u}}_1^A) \\ &\quad + B(\tilde{\sigma}_B \hat{\mathbf{u}}_1^B - \tilde{\alpha}\mathcal{C}(\hat{\mathbf{u}}_1^B, \mathbf{u}_2^\alpha) - \tilde{\alpha}\nabla^2 \hat{\mathbf{u}}_1^B) - A^3 \mathcal{C}(\hat{\mathbf{u}}_1^A, \mathbf{u}_2^{A^2}) - B^3 \mathcal{C}(\hat{\mathbf{u}}_1^B, \mathbf{u}_2^{B^2}) \\ &\quad - AB^2 \left(\mathcal{C}(\hat{\mathbf{u}}_1^A, \mathbf{u}_2^{B^2}) + \mathcal{C}(\hat{\mathbf{u}}_1^B, \mathbf{u}_2^{AB}) \right) - A^2 B \left(\mathcal{C}(\hat{\mathbf{u}}_1^B, \mathbf{u}_2^{A^2}) + \mathcal{C}(\hat{\mathbf{u}}_1^A, \mathbf{u}_2^{AB}) \right), \end{aligned} \quad (\text{C } 10)$$

and where $\tilde{\sigma}_A = \sigma_A/\epsilon^2$ and $\tilde{\sigma}_B = \sigma_B/\epsilon^2$. All the terms in \mathbf{F}_3 are resonant with either $\hat{\mathbf{u}}_1^A$ or $\hat{\mathbf{u}}_1^B$. To avoid secular terms we impose a compatibility condition, i.e. we require the respective inner products with either $\hat{\mathbf{u}}_1^{A\dagger}$ or $\hat{\mathbf{u}}_1^{B\dagger}$ be zero. With the normalisation $\langle \hat{\mathbf{u}}_1^{A\dagger}, \hat{\mathbf{u}}_1^A \rangle = \langle \hat{\mathbf{u}}_1^{B\dagger}, \hat{\mathbf{u}}_1^B \rangle = 1$, we obtain

$$\partial_{T_1} A = \tilde{\lambda}_A A - \tilde{\chi}_A A^3 - \tilde{\eta}_A AB^2, \quad (\text{C } 11)$$

$$\partial_{T_1} B = \tilde{\lambda}_B B - \tilde{\chi}_B B^3 - \tilde{\eta}_B A^2 B, \quad (\text{C } 12)$$

with the coefficients

$$\begin{aligned}\tilde{\lambda}_A &= \tilde{\sigma}_A + \tilde{\alpha} \langle \hat{\mathbf{u}}_1^{A\dagger}, -\mathcal{C}(\hat{\mathbf{u}}_1^A, \mathbf{u}_2^\alpha) - \nabla^2 \hat{\mathbf{u}}_1^A \rangle, \\ \tilde{\chi}_A &= \langle \hat{\mathbf{u}}_1^{A\dagger}, -\mathcal{C}(\hat{\mathbf{u}}_1^A, \mathbf{u}_2^{A^2}) \rangle, \\ \tilde{\eta}_A &= \langle \hat{\mathbf{u}}_1^{A\dagger}, -\mathcal{C}(\hat{\mathbf{u}}_1^A, \mathbf{u}_2^{B^2}) - \mathcal{C}(\hat{\mathbf{u}}_1^B, \mathbf{u}_2^{AB}) \rangle,\end{aligned}\tag{C 13}$$

and similar expressions for $\tilde{\lambda}_B$, $\tilde{\chi}_B$ and $\tilde{\eta}_B$ upon exchange of indices A and B .

Equations (C 11)-(C 12) constitute the leading-order system of amplitude equations. If the derivation is stopped at this order, one can reintroduce the fast time $t = \epsilon^2 T_1$ and obtain the system (3.1)-(3.2), with the coefficients $\lambda_A = \epsilon^2 \tilde{\lambda}_A$, $\chi_A = \epsilon^2 \tilde{\chi}_A$, etc.:

$$d_t A = \lambda_A A - \chi_A A^3 - \eta_A A B^2,\tag{C 14}$$

$$d_t B = \lambda_B B - \chi_B B^3 - \eta_B A^2 B.\tag{C 15}$$

To derive higher-order amplitude equations, the third-order field

$$\mathbf{q}_3(\mathbf{x}, T_1, T_2, \dots) = \tilde{\alpha} A \mathbf{q}_3^A + \tilde{\alpha} B \mathbf{q}_3^B + A^3 \mathbf{q}_3^{A^3} + B^3 \mathbf{q}_3^{B^3} + AB^2 \mathbf{q}_3^{AB^2} + A^2 B \mathbf{q}_3^{A^2 B},\tag{C 16}$$

is needed, where the \mathbf{q}_3^* fields are solution of:

$$\begin{aligned}\tilde{\mathcal{A}} \mathbf{q}_3^A &= \{-\mathcal{C}(\hat{\mathbf{u}}_1^A, \mathbf{u}_2^\alpha) - \nabla^2 \hat{\mathbf{u}}_1^A + \langle \hat{\mathbf{u}}_1^{A\dagger}, \mathcal{C}(\hat{\mathbf{u}}_1^A, \mathbf{u}_2^\alpha) + \nabla^2 \hat{\mathbf{u}}_1^A \rangle \hat{\mathbf{u}}_1^A, 0\}, \\ \tilde{\mathcal{A}} \mathbf{q}_3^{A^3} &= \{-\mathcal{C}(\hat{\mathbf{u}}_1^A, \mathbf{u}_2^{A^2}) + \tilde{\chi}_A \hat{\mathbf{u}}_1^A, 0\}, \\ \tilde{\mathcal{A}} \mathbf{q}_3^{A^2 B} &= \{-\mathcal{C}(\hat{\mathbf{u}}_1^B, \mathbf{u}_2^{A^2}) - \mathcal{C}(\hat{\mathbf{u}}_1^A, \mathbf{u}_2^{AB}) + \tilde{\eta}_B \hat{\mathbf{u}}_1^B, 0\},\end{aligned}\tag{C 17}$$

with similar expressions for \mathbf{q}_3^B , $\mathbf{q}_3^{B^3}$ and $\mathbf{q}_3^{AB^2}$ upon exchange of A and B .

Because the kernel of $\tilde{\mathcal{A}}$ is not empty, the \mathbf{q}_3^* fields are defined up to an arbitrary constant along $\hat{\mathbf{u}}_1^A$ or $\hat{\mathbf{u}}_1^B$. We remove this component such that $\langle \hat{\mathbf{u}}_1^{A\dagger}, \mathbf{u}_3^A \rangle = \langle \hat{\mathbf{u}}_1^{A\dagger}, \mathbf{u}_3^{A^3} \rangle = \langle \hat{\mathbf{u}}_1^{A\dagger}, \mathbf{u}_3^{AB^2} \rangle = \langle \hat{\mathbf{u}}_1^{B\dagger}, \mathbf{u}_3^B \rangle = \langle \hat{\mathbf{u}}_1^{B\dagger}, \mathbf{u}_3^{B^3} \rangle = \langle \hat{\mathbf{u}}_1^{B\dagger}, \mathbf{u}_3^{A^2 B} \rangle = 0$.

C.1.4. Fourth order

At order ϵ^4 the field \mathbf{q}_4 is a solution of the linearised and shifted NS equations

$$B \partial_t \mathbf{q}_4 + \tilde{\mathcal{A}} \mathbf{q}_4 = \{\mathbf{F}_4, 0\},\tag{C 18}$$

where symmetry considerations show that \mathbf{F}_4 is not resonant. Therefore, one can invert (C 18) and compute

$$\begin{aligned}\mathbf{q}_4(\mathbf{x}, T_1, T_2, \dots) &= \tilde{\alpha}^2 \mathbf{q}_4^\alpha + \partial_{T_1} (A^2) \mathbf{q}_4^{(A^2)'} + \partial_{T_1} (AB) \mathbf{q}_4^{(AB)'} + \partial_{T_1} (B^2) \mathbf{q}_4^{(B^2)'} \\ &\quad + \tilde{\alpha} A^2 \mathbf{q}_4^{A^2} + \tilde{\alpha} AB \mathbf{q}_4^{AB} + \tilde{\alpha} B^2 \mathbf{q}_4^{B^2} + A^4 \mathbf{q}_4^{A^4} + B^4 \mathbf{q}_4^{B^4} \\ &\quad + A^3 B \mathbf{q}_4^{A^3 B} + A^2 B^2 \mathbf{q}_4^{A^2 B^2} + AB^3 \mathbf{q}_4^{AB^3},\end{aligned}\tag{C 19}$$

where the \mathbf{q}_4^* fields are solution of:

$$\begin{aligned}
\tilde{\mathcal{A}}\mathbf{q}_4^\alpha &= \{-(\mathbf{u}_2^\alpha \cdot \nabla)\mathbf{u}_2^\alpha - \nabla^2\mathbf{u}_2^\alpha, 0\}, & \tilde{\mathcal{A}}\mathbf{q}_4^{(A^2)'} &= \{-\mathbf{u}_2^{A^2}, 0\}, \\
\tilde{\mathcal{A}}\mathbf{q}_4^{A^2} &= \{-\mathcal{C}(\mathbf{u}_2^{A^2}, \mathbf{u}_2^\alpha) - \mathcal{C}(\hat{\mathbf{u}}_1^A, \mathbf{u}_3^A) - \nabla^2\mathbf{u}_2^{A^2}, 0\}, & \tilde{\mathcal{A}}\mathbf{q}_4^{(AB)'} &= \{-\mathbf{u}_2^{AB}, 0\}, \\
\tilde{\mathcal{A}}\mathbf{q}_4^{AB} &= \{-\mathcal{C}(\mathbf{u}_2^{AB}, \mathbf{u}_2^\alpha) - \mathcal{C}(\hat{\mathbf{u}}_1^B, \mathbf{u}_3^A) - \mathcal{C}(\hat{\mathbf{u}}_1^A, \mathbf{u}_3^B) - \nabla^2\mathbf{u}_2^{AB}, 0\}, \\
\tilde{\mathcal{A}}\mathbf{q}_4^{A^2B^2} &= \{-(\mathbf{u}_2^{AB} \cdot \nabla)\mathbf{u}_2^{AB} - \mathcal{C}(\mathbf{u}_2^{A^2}, \mathbf{u}_2^{B^2}) - \mathcal{C}(\hat{\mathbf{u}}_1^B, \mathbf{u}_3^{A^2B}) - \mathcal{C}(\hat{\mathbf{u}}_1^A, \mathbf{u}_3^{AB^2}), 0\}, \\
\tilde{\mathcal{A}}\mathbf{q}_4^{A^3B} &= \{-\mathcal{C}(\mathbf{u}_2^{A^2}, \mathbf{u}_2^{AB}) - \mathcal{C}(\hat{\mathbf{u}}_1^B, \mathbf{u}_3^{A^3}) - \mathcal{C}(\hat{\mathbf{u}}_1^A, \mathbf{u}_3^{A^2B}), 0\}, \\
\tilde{\mathcal{A}}\mathbf{q}_4^{A^4} &= \{-(\mathbf{u}_2^{A^2} \cdot \nabla)\mathbf{u}_2^{A^2} - \mathcal{C}(\hat{\mathbf{u}}_1^A, \mathbf{u}_3^{A^3}), 0\}.
\end{aligned} \tag{C 20}$$

with similar expressions for $\mathbf{q}_4^{(B^2)'}$, $\mathbf{q}_4^{B^2}$, $\mathbf{q}_4^{AB^3}$, $\mathbf{q}_4^{B^4}$ upon exchange of A and B .

C.1.5. Fifth order

At order ϵ^5 the field \mathbf{q}_5 is a solution of the linearised and shifted NS equations

$$\mathcal{B}\partial_t\mathbf{q}_5 + \tilde{\mathcal{A}}\mathbf{q}_5 = \{\mathbf{F}_5, 0\}, \tag{C 21}$$

where all the terms in \mathbf{F}_5 resonate with either $\hat{\mathbf{u}}_1^A$ or $\hat{\mathbf{u}}_1^B$. Imposing a compatibility condition yields

$$\partial_{T_2}A = \langle \hat{\mathbf{u}}_1^{A\dagger}, A\mathbf{a} + A^3\mathbf{b} + AB^2\mathbf{c} + AB^4\mathbf{d} + A^3B^2\mathbf{e} + A^5\mathbf{f} \rangle, \tag{C 22}$$

where

$$\begin{aligned}
\mathbf{a} &= \tilde{\alpha}^2 [-\mathcal{C}(\mathbf{u}_2^\alpha, \mathbf{u}_3^A) - \mathcal{C}(\hat{\mathbf{u}}_1^A, \mathbf{u}_4^\alpha) - \nabla^2\mathbf{u}_3^A], \\
\mathbf{b} &= \tilde{\alpha} [-\mathcal{C}(\mathbf{u}_2^{A^2}, \mathbf{u}_3^A) - \mathcal{C}(\mathbf{u}_2^\alpha, \mathbf{u}_3^{A^3}) - \mathcal{C}(\hat{\mathbf{u}}_1^A, \mathbf{u}_4^{A^2}) - \nabla^2\mathbf{u}_3^{A^3}] - 2\tilde{\lambda}_A\mathcal{C}(\hat{\mathbf{u}}_1^A, \mathbf{u}_4^{(A^2)'})', \\
\mathbf{c} &= \tilde{\alpha} [-\mathcal{C}(\mathbf{u}_2^{B^2}, \mathbf{u}_3^A) - \mathcal{C}(\mathbf{u}_2^\alpha, \mathbf{u}_3^{AB^2}) - \mathcal{C}(\mathbf{u}_2^{AB}, \mathbf{u}_3^B) - \mathcal{C}(\hat{\mathbf{u}}_1^B, \mathbf{u}_4^{AB}) - \mathcal{C}(\hat{\mathbf{u}}_1^A, \mathbf{u}_4^{B^2}) \\
&\quad - \nabla^2\mathbf{u}_3^{AB^2}] - 2\tilde{\lambda}_B\mathcal{C}(\hat{\mathbf{u}}_1^A, \mathbf{u}_4^{(B^2)'})' - (\tilde{\lambda}_A + \tilde{\lambda}_B)\mathcal{C}(\hat{\mathbf{u}}_1^B, \mathbf{u}_4^{(AB)'})', \\
\mathbf{d} &= -\mathcal{C}(\mathbf{u}_2^{B^2}, \mathbf{u}_3^{AB^2}) - \mathcal{C}(\mathbf{u}_2^{AB}, \mathbf{u}_3^{B^3}) - \mathcal{C}(\hat{\mathbf{u}}_1^B, \mathbf{u}_4^{AB^3}) - \mathcal{C}(\hat{\mathbf{u}}_1^A, \mathbf{u}_4^{B^4}) \\
&\quad + 2\tilde{\chi}_B\mathcal{C}(\hat{\mathbf{u}}_1^A, \mathbf{u}_4^{(B^2)'})' + (\tilde{\eta}_A + \tilde{\chi}_B)\mathcal{C}(\hat{\mathbf{u}}_1^B, \mathbf{u}_4^{(AB)'})', \\
\mathbf{e} &= -\mathcal{C}(\mathbf{u}_2^{B^2}, \mathbf{u}_3^{A^3}) - \mathcal{C}(\mathbf{u}_2^{AB}, \mathbf{u}_3^{A^2B}) - \mathcal{C}(\mathbf{u}_2^{A^2}, \mathbf{u}_3^{AB^2}) - \mathcal{C}(\hat{\mathbf{u}}_1^B, \mathbf{u}_4^{A^3B}) - \mathcal{C}(\hat{\mathbf{u}}_1^A, \mathbf{u}_4^{A^2B^2}) \\
&\quad + 2\tilde{\eta}_A\mathcal{C}(\hat{\mathbf{u}}_1^A, \mathbf{u}_4^{(A^2)'})' + 2\tilde{\eta}_B\mathcal{C}(\hat{\mathbf{u}}_1^A, \mathbf{u}_4^{(B^2)'})' + (\tilde{\chi}_A + \tilde{\eta}_B)\mathcal{C}(\hat{\mathbf{u}}_1^B, \mathbf{u}_4^{(AB)'})', \\
\mathbf{f} &= -\mathcal{C}(\mathbf{u}_2^{A^2}, \mathbf{u}_3^{A^3}) - \mathcal{C}(\hat{\mathbf{u}}_1^A, \mathbf{u}_4^{A^4}) + 2\tilde{\chi}_A\mathcal{C}(\hat{\mathbf{u}}_1^A, \mathbf{u}_4^{(A^2)'})'.
\end{aligned} \tag{C 23}$$

A similar equation is obtained for $\partial_{T_2}B$ upon exchange of A and B .

Terms proportional to $\tilde{\lambda}_A$, $\tilde{\chi}_A$, etc., come from the interaction of the eigenmodes with the fourth-order fields $\mathbf{q}_4^{(A^2)'}$, $\mathbf{q}_4^{(AB)'}$ and $\mathbf{q}_4^{(B^2)'}$, and are obtained after developing $\partial_{T_1}(A^2)$, $\partial_{T_1}(AB)$ and $\partial_{T_1}(B^2)$ and using (C 11)-(C 12). By contrast, all the forcing terms of the form $\partial_{T_1}(A^m B^n)\mathbf{u}_3^*$ with $m+n=1$ or 3 vanish when imposing the compatibility condition because of our choice to impose $\langle \hat{\mathbf{u}}_1^\dagger, \mathbf{u}_3^* \rangle = 0$.

Defining coefficients $\tilde{*}'$, we obtain:

$$\partial_{T_2}A = \tilde{\lambda}'_A A - \tilde{\chi}'_A A^3 - \tilde{\eta}'_A AB^2 + \tilde{\kappa}'_A AB^4 + \tilde{\beta}'_A A^3 B^2 + \tilde{\gamma}'_A A^5 \tag{C 24}$$

$$\partial_{T_2}B = \tilde{\lambda}'_B B - \tilde{\chi}'_B B^3 - \tilde{\eta}'_B A^2 B + \tilde{\kappa}'_B A^4 B + \tilde{\beta}'_B A^2 B^3 + \tilde{\gamma}'_B B^5 \tag{C 25}$$

Finally, the total fifth-order amplitude equations are obtained by reconstructing the total derivatives $d_t(A, B) = (\epsilon^2 \partial_{T_1} + \epsilon^4 \partial_{T_2})(A, B)$, i.e. combining (C 11)-(C 12) and (C 24)-(C 25):

$$d_t A = \lambda_A A - \chi_A A^3 - \eta_A A B^2 + \kappa_A A B^4 + \beta_A A^3 B^2 + \gamma_A A^5, \quad (\text{C } 26)$$

$$d_t B = \lambda_B B - \chi_B B^3 - \eta_B A^2 B + \kappa_B A^4 B + \beta_B A^2 B^3 + \gamma_B B^5, \quad (\text{C } 27)$$

where now $\lambda_A = \epsilon^2 \tilde{\lambda}_A + \epsilon^4 \tilde{\lambda}'_A$, $\chi_A = \epsilon^2 \tilde{\chi}_A + \epsilon^4 \tilde{\chi}'_A$, etc. Therefore, compared to the third-order system, the fifth-order system has not only higher-order terms but also corrected coefficients.

C.2. Equilibrium solutions

C.2.1. Third-order system

The third-order system (3.1)-(3.2) has four possible equilibrium solutions:

- Symmetric state: $A = B = 0$;
- Pure vertical symmetry breaking: $A^2 = \lambda_A / \chi_A$, $B = 0$;
- Pure horizontal symmetry breaking: $A = 0$, $B^2 = \lambda_B / \chi_B$;
- Mixed state (double symmetry breaking): $A^2 = (\chi_B \lambda_A - \eta_A \lambda_B) / (\chi_A \chi_B - \eta_A \eta_B)$, $B^2 = (\chi_A \lambda_B - \eta_B \lambda_A) / (\chi_A \chi_B - \eta_A \eta_B)$.

C.2.2. Fifth-order system

The fifth-order system (3.3)-(3.4) has four types of equilibrium states, with multiple possible amplitudes:

- Symmetric state: $A = B = 0$;
- Pure vertical symmetry breaking: $A^2 = \pm \sqrt{(\chi_A \pm \sqrt{\Delta}) / (2\gamma_A)}$, $B = 0$, where $\Delta = \chi_A^2 - 4\lambda_A \gamma_A$. Real-valued solutions exist when $\Delta > 0$ and $(\chi_A \pm \sqrt{\Delta}) / \gamma_A > 0$. Focusing on positive values, this yields up to two different amplitudes A_1, A_2 ;
- Pure horizontal symmetry breaking: $A = 0$, $B^2 = \pm \sqrt{(\chi_B \pm \sqrt{\Delta}) / (2\gamma_B)}$, where $\Delta = \chi_B^2 - 4\lambda_B \gamma_B$. Real-valued solutions exist when $\Delta > 0$ and $(\chi_B \pm \sqrt{\Delta}) / \gamma_B > 0$. Again, there are up to two different positive amplitudes B_1, B_2 ;
- Mixed states (double symmetry breaking) $A \neq 0, B \neq 0$. These states correspond to the intersections of conic sections, since $u = A^2$ and $v = B^2$ satisfy the bivariate quadratic equations

$$0 = \lambda_A - \chi_A u - \eta_A v + \kappa_A v^2 + \beta_A uv + \gamma_A u^2, \quad (\text{C } 28)$$

$$0 = \lambda_B - \chi_B v - \eta_B u + \kappa_B u^2 + \beta_B uv + \gamma_B v^2. \quad (\text{C } 29)$$

An analytic treatment of these equations can be found for example in chapter 11 of Richter-Gebert (2011). There are in general zero, two or four real-valued intersections. Here, we compute these intersections numerically with the algorithm of Nakatsukasa et al. (2015).

Appendix D. Proper orthogonal decomposition

In section 4 we have used proper orthogonal decomposition (POD) to separate the dominant modes of the flow. In this appendix, we briefly recall the computational procedure and provide computational details.

In general POD is based on performing the singular value decomposition (SVD) of the snapshot matrix S . The snapshot matrix has N_{dof} rows and m columns,

where N_{dof} denotes the number of degrees of freedom of the problem and m the number of snapshots used. The SVD is expressed as

$$S = U \Sigma V^T \quad (\text{D } 1)$$

where U and V are unitary and Σ is diagonal. The j_{th} basis function is the j_{th} column of U , while the coefficients of the POD bases are given by $\Sigma V^T = U^T S$.

To reduce the computational cost we have used the method of snapshots (Sirovich 1987), that is useful when the snapshot matrix is tall and skinny, i.e. when the number of degrees of freedom N_{dof} is much larger than the number of snapshots m , i.e. $N_{dof} \gg m$. Instead of performing a singular value decomposition, this method manipulates the problem and leads to a smaller eigenvalue problem, i.e

$$S^T S Z = Z \Lambda \quad (\text{D } 2)$$

where $S^T S$ is known as the snapshot covariance matrix with size $m \times m$, Λ is the diagonal matrix of eigenvalues and Z are the corresponding eigenvectors. Note that

$$S^T S = V \Sigma^2 V^T \quad (\text{D } 3)$$

implying that

$$S^T S V = V \Sigma^2. \quad (\text{D } 4)$$

Therefore, the right singular vectors of S , i.e. V , are the same as the eigenvectors of $S^T S$, i.e. Z . Also, the singular values of S are the positive square roots of the eigenvalues of $S^T S$. Based on this, one can solve the eigenvalue problem D 2, and obtain the j_{th} POD basis function ϕ_j as:

$$\phi_j = \frac{1}{\sqrt{\lambda_j}} \sum_{\ell=1}^m (z_j)_\ell S_{(\cdot,\ell)}, \quad 1 \leq j \leq r, \quad (\text{D } 5)$$

where $(z_j)_\ell$ is the ℓ_{th} component of the j_{th} eigenvector z_j of $S^T S$, $S_{(\cdot,\ell)}$ is the ℓ_{th} column of S , and r is the number of POD modes considered.

When computing the POD modes we have used a portion of the domain only, to reduce the computational cost, and interpolated on a uniform grid to avoid the need of weight matrices when performing the scalar products. For both $W = 1.2$ and $W = 2.25$ we have restricted the analysis to $-3.7 \leq x \leq 17.7$, $-3.2 \leq y, z \leq 3.2$ and interpolated on a cubic grids with $N_x = N_y = 120$ and $N_z = 410$ for a total of approximately 5.9×10^6 grids points. The number of snapshots and their time separation has been chosen to properly capture all the frequencies of the flow. The sampling time δt_s has been chosen to be approximately $1/(20f_i)$, where f_i is the largest and fastest frequency of the flow detected in the spectra. The total integration time T , instead, has been chosen to be approximately $8/f_s$, where f_s is the smallest and slowest frequency. Therefore, for $W = 1.2$ and $Re = 515$, $\delta t_s = 0.174$ and $T = \delta t_s \times 600$. For $W = 2.25$ and $Re = 380$, instead, $\delta t_s = 0.195$ and $T = \delta t_s \times 600$. This means that $N_{dof} \approx 17.7 \times 10^6$ (three velocity components for each grid point) and $m = 600$.

Appendix E. Structure of the LE vortex shedding for $W = 2.25$

In this appendix we address the apparent discrepancy between the left panels of figure 21 and figure 22, in terms of wavelength and periodicity. In the POD analysis (figure 21), trains of hairpin vortices with streamwise vorticity of alternating

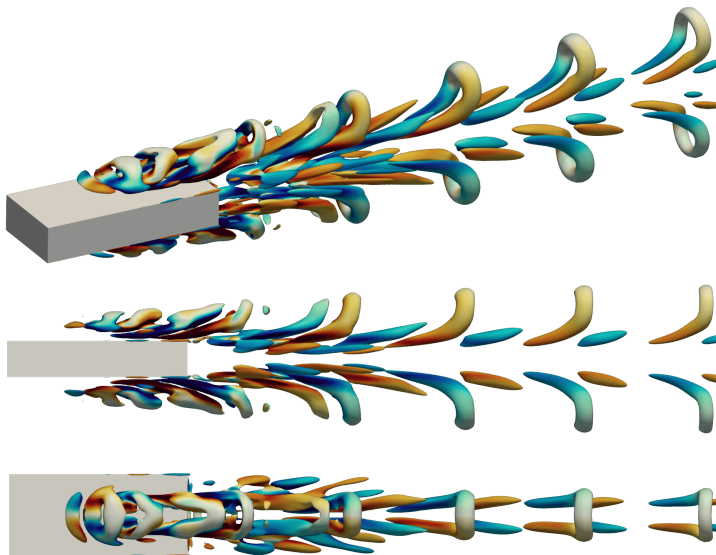


Figure 37: Structure of the perturbation field $\{\mathbf{u}, p\} - \{\langle \mathbf{u} \rangle_t, \langle p \rangle_t\}$ (where $\langle \cdot \rangle_t$ denotes the time average) for $W = 2.25$ and $Re = 420$ (regime $pS_y S_z la$). Top: three-dimensional view. Centre: lateral view. Bottom: top view. The isosurfaces are for $\lambda_2 = -0.04$, and are coloured with the streamwise vorticity of the fluctuating field in the $-1 \leq \omega'_x \leq 1$ range.

sign are shed from the LE shear layer; also, a total of four hairpin vortices are simultaneously accommodated over the top and bottom sides of the prism when $L = 5$. By contrast, the DNS visualisations (figure 22) show only two hairpin vortices over the sides of the prisms at each time, both with streamwise vorticity of the same sign. In this case, indeed, vortices with vorticity that oppose to the mean velocity gradients are not visible. However, we show the consistency of our results in figure 37. Here we consider $W = 2.25$ and $Re = 420$ (regime $pS_y S_z la$), and we plot isocontours of negative λ_2 , computed using the perturbation field, i.e. $\{\mathbf{u}, p\} - \{\langle \mathbf{u} \rangle_t, \langle p \rangle_t\}$, where the operator $\langle \cdot \rangle_t$ denotes time averaging. We note that getting rid of the time-averaged contribution yields the same structures as the POD mode, with four hairpin vortices with streamwise vorticity of opposite sign simultaneously placed over the top/bottom sides of the prism.

REFERENCES

- BARKLEY, D. & HENDERSON, R. D. 1996 Three-dimensional Floquet stability analysis of the wake of a circular cylinder. *J. Fluid Mech.* **322**, 215–241.
- BLACKBURN, H. M. & LOPEZ, J. M. 2003 On three-dimensional quasiperiodic Floquet instabilities of two-dimensional bluff body wakes. *Phys. Fluids* **15** (8), L57–L60.
- BLACKBURN, H. M., MARQUES, F. & LOPEZ, J. M. 2005 Symmetry breaking of two-dimensional time-periodic wakes. *J. Fluid Mech.* **522**, 395–411.
- BLACKBURN, H. M. & SHEARD, G. J. 2010 On quasiperiodic and subharmonic Floquet wake instabilities. *Phys. Fluids* **22** (3), 031701.
- BOHORQUEZ, P., SANMIGUEL-ROJAS, E., SEVILLA, A., JIMÉNEZ-GONZÁLEZ, J. I. & MARTÍNEZ-BAZÁN, C. 2011 Stability and dynamics of the laminar wake past a slender blunt-based axisymmetric body. *J. Fluid Mech.* **676**, 110–144.

- BRUNO, L., SALVETTI, M. V. & RICCIARDELLI, F. 2014 Benchmark on the aerodynamics of a rectangular 5:1 cylinder: An overview after the first four years of activity. *J. Wind Eng. Ind. Aerodyn.* **126**, 87–106.
- CHAURASIA, H.K. & THOMPSON, M.C. 2011 Three-dimensional instabilities in the boundary-layer flow over a long rectangular plate. *J. Fluid Mech.* **681**, 411–433.
- CHIARINI, A., GATTI, D., CIMARELLI, A. & QUADRIO, M. 2022a Structure of turbulence in the flow around a rectangular cylinder. *J. Fluid Mech.* **946**, A35.
- CHIARINI, A. & QUADRIO, M. 2021 The Turbulent Flow over the BARC Rectangular Cylinder: A DNS Study. *Flow Turbul. Combust.* **107**, 875–899.
- CHIARINI, A. & QUADRIO, M. 2022 The importance of corner sharpness in the BARC test case: a numerical study. *Wind Struct.* **34** (1), 43–58.
- CHIARINI, A., QUADRIO, M. & AUTERI, F. 2021 Linear stability of the steady flow past rectangular cylinders. *J. Fluid Mech.* **929**, A36.
- CHIARINI, A., QUADRIO, M. & AUTERI, F. 2022b An almost subharmonic instability in the flow past rectangular cylinders. *J. Fluid Mech.* **950**, A20.
- CHIARINI, A., QUADRIO, M. & AUTERI, F. 2022c On the frequency selection mechanism of the low-Re flow around rectangular cylinders. *J. Fluid Mech.* **933**, A44.
- CHOI, H., JEON, W.-P. & KIM, J. 2008 Control of Flow Over a Bluff Body. *Ann. Rev. Fluid Mech.* **40** (1), 113–139.
- CHOMAZ, J.-M. 2005 Global instabilities in spatially developing flows: Non-normality and nonlinearity. *Annu. Rev. Fluid Mech.* **37** (1), 357–392.
- CITRO, V., SICONOLFI, L., FABRE, D., GIANNETTI, F. & LUCHINI, P. 2017 Stability and Sensitivity Analysis of the Secondary Instability in the Sphere Wake. *AIAA Journal* **55** (11), 3661–3668.
- DUCIMETIÈRE, Y.-M., BOUJO, E. & GALLAIRE, F. 2024 Noise-induced transitions past the onset of a steady symmetry-breaking bifurcation: The case of the sudden expansion. *Phys. Rev. Fluids* **9**, 053905.
- FABRE, D., AUGUSTE, F. & MAGNAUDET, J. 2008 Bifurcations and symmetry breaking in the wake of axisymmetric bodies. *Phys. Fluids* **20** (5), 051702.
- GIANNETTI, F., CAMARRI, S. & LUCHINI, P. 2010 Structural sensitivity of the secondary instability in the wake of a circular cylinder. *J. Fluid Mech.* **651**, 319–337.
- GIANNETTI, F. & LUCHINI, P. 2007 Structural sensitivity of the first instability of the cylinder wake. *J. Fluid Mech.* **581**, 167–197.
- HECHT, F. 2012 New development in FreeFem++. *J. Num. Math.* **20** (3–4), 251–266.
- HOURIGAN, K., THOMPSON, M. C. & TAN, B. T. 2001 Self-sustained oscillations in flows around long blunt plates. *J. Fluids Struct.* **15** (3), 387–398.
- INOUE, O. & SAKURAGI, A. 2008 Vortex shedding from a circular cylinder of finite length at low Reynolds numbers. *Phys. Fluids* **20** (3), 033601.
- IOOSS, G. & JOSEPH, D. D. 1990 Elementary Stability and Bifurcation Theory. New York, NY: Springer.
- JACKSON, C. P. 1987 A finite-element study of the onset of vortex shedding in flow past variously shaped bodies. *J. Fluid Mech.* **182**, 23–45.
- JOHNSON, T. A. & PATEL, V. C. 1999 Flow past a sphere up to a Reynolds number of 300. *J. Fluid Mech.* **378**, 19–70.
- KLOTZ, L., GOUJON-DURAND, S., ROKICKI, J. & WESFREID, J. E. 2014 Experimental investigation of flow behind a cube for moderate Reynolds numbers. *J. Fluid Mech.* **750**, 73–98.
- KUZNETSOV, Y. 2004 Elements of Applied Bifurcation Theory, 3rd edn. New York: Springer-Verlag.
- LI, X.-B., DEMANGE, S., CHEN, G., WANG, J.-B., LIANG, X.-F., SCHMIDT, O.T. & OBERLEITHNER, K. 2024 Linear stability and spectral modal decomposition of three-dimensional turbulent wake flow of a generic high-speed train, arXiv: 2401.12575.
- LUCHINI, P. 2013 Linearized no-slip boundary conditions at a rough surface. *J. Fluid Mech.* **737**, 349–367.
- LUCHINI, P. 2016 Immersed-boundary simulation of turbulent flow past a sinusoidally undulated river bottom. *Eur. J. Mech. B Fluids* **55**, 340–347.
- LUCHINI, P. 2021 Introducing CPL. *2012.12143* .

- MAGARVEY, R. H. & BISHOP, ROY L. 1961a Transition ranges for three-dimensional wakes. *J. Phys.* **39** (10), 1418–1422.
- MAGARVEY, R. H. & BISHOP, ROY L. 1961b Wakes in Liquid-Liquid Systems. *Phys. Fluids* **4** (7), 800–805.
- MAGARVEY, R. H. & MACLATCHY, C. S. 1965 Vortices in sphere wakes. *Can. J. Phys.* **43** (9), 1649–1656, publisher: NRC Research Press.
- MAGNAUDET, J. & MOUGIN, G. 2007 Wake instability of a fixed spheroidal bubble. *J. Fluid Mech.* **572**, 311–337, publisher: Cambridge University Press.
- MARQUET, O. & LARSSON, M. 2015 Global wake instabilities of low aspect-ratio flat-plates. *Eur. J. Mech. B Fluids* **49**, 400–412.
- MELIGA, P., CHOMAZ, J.-M. & SIPP, D. 2009 Global mode interaction and pattern selection in the wake of a disk: a weakly nonlinear expansion. *J. Fluid Mech.* **633**, 159–189.
- MENG, Q., AN, H., CHENG, L. & KIMIAEI, M. 2021 Wake transitions behind a cube at low and moderate reynolds numbers. *J. Fluid Mech.* **919**, A44.
- MILLS, R., SHERIDAN, J., HOURIGAN, K. & WELSH, M. C. 1995 The mechanism controlling vortex shedding from rectangular bluff bodies. *Proceeding Twelfth Australas. Fluid Mech. Conf.* pp. 227–230.
- MONKEWITZ, P. A., HUERRE, P. & CHOMAZ, J.-M. 1993 Global linear stability analysis of weakly non-parallel shear flows. *J. Fluid Mech.* **251**, 1–20.
- NAKAMURA, Y., OHYA, Y. & TSURUTA, H. 1991 Experiments on vortex shedding from flat plates with square leading and trailing edges. *J. Fluid Mech.* **222**, 437–447.
- NAKATSUKASA, Y., NOFERINI, V. & TOWNSEND, A. 2015 Computing the common zeros of two bivariate functions via Bézout resultants. *Numerische Mathematik* **129**, 181–209.
- NATARAJAN, R. & ACRIVOS, A. 1993 The instability of the steady flow past spheres and disks. *J. Fluid Mech.* **254**, 323–344.
- NAUDASCHER, E. & ROCKWELL, D. 1994 *Flow-Induced Vibrations : An Engineering Guide. Hydraulic Structures Design Manual* 7. Rotterdam ; Brookfield, VT : A.A. Balkema, 1994.
- NOACK, B. R. & ECKELMANN, H. 1994 A global stability analysis of the steady and periodic cylinder wake. *J. Fluid Mech.* **270**, 297–330.
- OERTEL, H 1990 Wakes Behind Blunt Bodies. *Annu. Rev. Fluid Mech.* **22** (1), 539–562.
- OKAJIMA, A. 1982 Strouhal numbers of rectangular cylinders. *J. Fluid Mech.* **123**, 379–398.
- PIERSON, J.-L., AUGUSTE, F., HAMMOUTI, A. & WACHS, A. 2019 Inertial flow past a finite-length axisymmetric cylinder of aspect ratio 3: Effect of the yaw angle. *Phys. Rev. Fluids* **4** (4), 044802.
- RICHTER-GEBERT, J. 2011 *Perspectives on Projective Geometry*. Springer Berlin, Heidelberg.
- ROBICHAUX, J., BALACHANDAR, S. & VANKA, S. P. 1999 Three-dimensional Floquet instability of the wake of square cylinder. *Phys. Fluids* **11** (3), 560–578.
- SAHA, A. K. 2004 Three-dimensional numerical simulations of the transition of flow past a cube. *Phys. Fluids* **16** (5), 1630–1646.
- SHEARD, G. J., THOMPSON, M. C. & HOURIGAN, K. 2008 Flow normal to a short cylinder with hemispherical ends. *Phys. Fluids* **20** (4), 041701.
- SIROVICH, L. 1987 Turbulence and the dynamics of coherent structures. I. Coherent structures. *Quarterly of Applied Mathematics* **45** (3), 561–571.
- THEOFILIS, V. 2003 Advances in global linear instability analysis of nonparallel and three-dimensional flows. *Prog. Aerosp. Sci.* **39** (4), 249–315.
- THEOFILIS, V. 2011 Global Linear Instability. *Annu. Rev. Fluid Mech.* **43** (1), 319–352.
- THOMPSON, M. C. 2012 Effective transition of steady flow over a square leading-edge plate. *J. Fluid Mech.* **698**, 335–357.
- THOMPSON, M. C., LEWEKE, T. & HOURIGAN, K. 2021 Bluff Bodies and Wake–Wall Interactions. *Annu. Rev. Fluid Mech.* **53** (1), 347–376.
- TOMBOULIDES, A. G. & ORSZAG, S. A. 2000 Numerical investigation of transitional and weak turbulent flow past a sphere. *J. Fluid Mech.* **416**, 45–73.
- TOMBOULIDES, A. G., ORSZAG, S. A. & KARNIADAKIS, G. E. 1993 Direct and Large-Eddy Simulation of the Flow Past a Sphere. In *Engineering Turbulence Modelling and Experiments*, pp. 273–282. Elsevier.
- WILLIAMSON, C. H. K. 1996a Three-dimensional wake transition. *J. Fluid Mech.* **328**, 345–407.

- WILLIAMSON, C H K 1996b Vortex Dynamics in the Cylinder Wake. *Annu. Rev. Fluid Mech.* **28** (1), 477–539.
- WILLIAMSON, C. H. K. & GOVARDHAN, R. 2008 A brief review of recent results in vortex-induced vibrations. *J. Wind Eng. Ind. Aerodyn.* **96** (6), 713–735.
- YANG, Y., FENG, Z. & ZHANG, M. 2022 Onset of vortex shedding around a short cylinder. *J. Fluid Mech.* **933**.
- ZAMPOGNA, G. A. & BOUJO, E. 2023 From thin plates to Ahmed bodies: linear and weakly nonlinear stability of rectangular prisms. *J. Fluid Mech.* **966**, A19.
- ZDRAVKOVICH, M. M., BRAND, V. P., MATHEW, G. & WESTON, A. 1989 Flow past short circular cylinders with two free ends. *J. Fluid Mech.* **203**, 557–575.
- ZDRAVKOVICH, M. M., FLAHERTY, A. J., PAHLE, M. G. & SKELHORNE, I. A. 1998 Some aerodynamic aspects of coin-like cylinders. *J. Fluid Mech.* **360**, 73–84.
- ZHANG, Z., KAREEM, A., XU, F. & JIANG, H. 2023 Global instability and mode selection in flow fields around rectangular prisms. *J. Fluid Mech.* **955**, A19.